AFRL-IF-RS-TR-2005-6
Final Technical Report
January 2005

LARGE-SCALE INTEGRATION OF SOLID-STATE MICROFLUIDIC VALVES WITH NO MOVING PARTS

University of Michigan

Sponsored by
Defense Advanced Research Projects Agency
DARPA Order No. J302

APPROVED FOR PUBLIC RELEASE; DISTRIBUTION UNLIMITED.

The views and conclusions contained in this document are those of the authors and should not be interpreted as necessarily representing the official policies, either expressed or implied, of the Defense Advanced Research Projects Agency or the U.S. Government.

AIR FORCE RESEARCH LABORATORY
INFORMATION DIRECTORATE
ROME RESEARCH SITE
ROME, NEW YORK

STINFO FINAL REPORT

This report has been reviewed by the Air Force Research Laboratory, Information Directorate, Public Affairs Office (IFOIPA) and is releasable to the National Technical Information Service (NTIS). At NTIS it will be releasable to the general public, including foreign nations.

AFRL-IF-RS-TR-2005-6 has been reviewed and is approved for publication

APPROVED: /s/

PETER J. ROCCI, JR.
Project Engineer

FOR THE DIRECTOR: /s/

JAMES A. COLLINS, Acting Chief
Advanced Computing Division
Information Directorate

REPORT DOCUMENTATION PAGE

Form Approved
OMB No. 074-0188

Public reporting burden for this collection of information is estimated to average 1 hour per response, including the time for reviewing instructions, searching existing data sources, gathering and maintaining the data needed, and completing and reviewing this collection of information. Send comments regarding this burden estimate or any other aspect of this collection of information, including suggestions for reducing this burden to Washington Headquarters Services, Directorate for Information Operations and Reports, 1215 Jefferson Davis Highway, Suite 1204, Arlington, VA 22202-4302, and to the Office of Management and Budget, Paperwork Reduction Project (0704-0188), Washington, DC 20503

1. AGENCY USE ONLY (Leave blank)	2. REPORT DATE	3. REPORT TYPE AND DATES COVERED
	JANUARY 2005	Final Jun 00 – Sep 03

4. TITLE AND SUBTITLE
LARGE-SCALE INTEGRATION OF SOLID-STATE MICROFLUIDIC VALVES WITH NO MOVING PARTS

5. FUNDING NUMBERS
C - F30602-00-1-0571
PE - 63739E
PR - E117
TA - 00
WU - 58

6. AUTHOR(S)
Carlos H. Mastangelo,
Yogesh B. Gianchandani, and
J.M.J. Frechet

7. PERFORMING ORGANIZATION NAME(S) AND ADDRESS(ES)
University of Michigan
3003 South State Street
Ann Arbor Michigan 48109-1287

8. PERFORMING ORGANIZATION REPORT NUMBER
N/A

9. SPONSORING / MONITORING AGENCY NAME(S) AND ADDRESS(ES)
Defense Advanced Research Projects Agency
3701 North Fairfax Drive
Arlington Virginia 22203-1714

AFRL/IFTB
525 Brooks Road
Rome New York 13441-4505

10. SPONSORING / MONITORING AGENCY REPORT NUMBER
AFRL-IF-RS-TR-2005-6

11. SUPPLEMENTARY NOTES

AFRL Project Engineer: Peter J. Rocci, Jr./IFTB/(315) 330-4654/ Peter.Rocci@rl.af.mil

12a. DISTRIBUTION / AVAILABILITY STATEMENT
APPROVED FOR PUBLIC RELEASE; DISTRIBUTION UNLIMITED.

12b. DISTRIBUTION CODE

13. ABSTRACT ***(Maximum 200 Words)***

This research concerns the development of a new kind of revolutionary design, solid-state microvalves that will permit the realization of complex microfluidic systems with arrays of hundreds of flow-control devices. Microfluidic systems have widespread applications in the implementation of immunological and genetic assays of both commercial and DoD interest. While fluidic capillary microchips made of glass, silicon, and plastic have been realized, their practical use has been so far confined to simple systems with very few assay steps such as PCR followed by electrophoresis or hybridization analyses. The scope of the project is focused on the elements necessary to demonstrate the feasibility of a simple, integratable, single element microvalves with no moving parts for microfluidic systems. A major goal of this program is the development of thin film active (and passive) polymer plugs that can be micromachined and integrated with microfluidic substrates to implement these plug valve devices.

14. SUBJECT TERMS
Solid-State Microvalves, Microfluidic Systems, Micromachining

15. NUMBER OF PAGES
183

16. PRICE CODE

17. SECURITY CLASSIFICATION OF REPORT	18. SECURITY CLASSIFICATION OF THIS PAGE	19. SECURITY CLASSIFICATION OF ABSTRACT	20. LIMITATION OF ABSTRACT
UNCLASSIFIED	UNCLASSIFIED	UNCLASSIFIED	UL

TABLE OF CONTENTS

SECTIONS

MICROPUMPS, VALVES AND MICRO TOTAL ANALYSIS SYSTEMS 1

1.1 Introduction 1
1.2 Micropumps 2
1.2.1 Mechanical Pumps 2
1.2.2 Non-Mechanical Pumps 6
1.3 Microvalves 11
1.3.1 Passive Valves 12
1.3.2 Active Valves 12
1.3.3 Hydrogel Valves 15
1.4 Analysis Methods 16
1.4.1 DNA Analysis 16
1.4.2 Protein Analysis 22
1.4.3 Chemical Analysis 23
1.4.4 Cell Analysis 23
1.5 Advantages of Integrated Systems 23
1.6 Realization Of An Integrated System 24
1.7 Report Organization 27

DOUBLE LAYER CONCEPT AND ELECTRO-OSMOTIC FLOW 30

2.1 Introduction 30
2.2 Double Layer Concept And Interface Charge and Potential Distribution 30
2.3 Double Layer Capacitance 34
2.3.1 The Helmholtz model 34
2.3.2 The Gouy-Chapman Model 36
2.3.3 The Gouy-Chapman-Stern Model 37
2.4 Electro-osmotic Flow 38

2.5 Modeling Flow Through Porous Medium 43
2.6 Circuit Model For The Fluid Flow In Microchannels 45
2.7 Pressures Generated Due To Droplets in Reservoirs 49
2.8 Conclusion 50
ELECTRODE KINETICS AND FARADAIC REACTIONS 51
3.1 Introduction 51
3.2 Faradaic And Non-Faradaic Processes 52
3.2.1 Non-Faradaic Processes 53
3.2.2 Faradaic Processes 54
3.3 Nernst Equation 55
3.4 Mass transfer 56
3.5 Butler-Volmer Model For Electrode Kinetics 57
3.6 Equivalent Models For Small And Large Overpotential Changes 58
3.6.1 Linear Approximation Of The Faradaic Response 59
3.6.2 Limit Current Of Linearity 60
3.6.3 Model For Nonlinearity At Low Frequencies 61
3.6.4 Faradaic Rectification 64
3.6.5 Stronger Non-Linearities At Low Frequencies 64
3.7 Voltage Time Response During Electrolysis With Alternating Currents 65
3.8 Current Voltage Relationship During Electrolysis 69
3.9 Theoretical Non-Gassing Limits For AC Current Drive 71
3.10 Voltage Time Response Causing Net Flow 73
3.11 Conclusion 76
SURFACE MICROMACHINED POROUS-PLUG ELECTRO-OSMOTIC PUMP 78
4.1 Introduction 78
4.2 Electrodes 79
4.3 Device Fabrication 81
4.3.1 Porous plug (pp) fabrication 81
4.3.2 Pp-EOP fabrication 84
4.4 Porous Polymer Characterization 88
4.5 Results and Discussion 89
4.5.1 Electro-osmotic Velocities Versus Applied Potential 90
4.5.2 Low Frequency Zero Averaged Current Drive 92
4.6 Conclusion 93
ENHANCED ELECTRO-OSMOTIC PUMPING WITH LIQUID BRIDGE AND FIELD EFFECT FLOW RECTIFICATION 100
5.1 Introduction 100
5.2 DC Drive Through Liquid Bridges 101
5.2.1 Advantage of Porous Polymer 102
5.2.2 Electro-Osmotically Induced Hydraulic Pumping 103
5.2.3 Fabrication and Test Results 106
5.3 AC Drive With Field Effect Rectification 109
5.3.1 AC Electro-Osmosis 110

5.3.2 Time Scale of Electro-Osmotic Flow 113
5.3.3 Fabrication 113
5.3.4 Net Electro-Osmotic Velocity After Rectification 114
5.3.5 Test Resuts 118
5.4 Conclusion 120
THERMALLY RESPONSIVE POLYMER VALVE 121
6.1 Introduction 121
6.2 Chemistry of Thermally Responsive Polymer.....122
6.3 Thin film formation.....123
6.4 Volume change characterization.....124
6.5 Device fabrication.....126
6.6 Test Results.....128
6.7 Mesoscale Thermally Responsive Monolithic Valves.....131
6.8 Mesoscale Thermally Responsive Monolithic Valve With Adjustable LCST 140
6.9 Conclusion 150
CONCLUSION AND FUTURE WORK 151
7.1 Conclusion 151
7.2 Future Work 155
PARTIALLY SUPPORTED PUBLICATIONS BY THIS CONTRACT.....158
BIBLIOGRAPHY 160

LIST OF FIGURES

Fig. 1.1. Electrostatically actuated micropump with check valves. 3

Fig. 1.2.Valveless diffuser-nozzle configuration. 4

Fig. 1.3. Peristaltic pump with three chamber (left) and three-phase chamber activation sequence (right). 4

Fig. 1.4. Dual diaphragm pump. 5

Fig. 1.5. Flow rectification by liquid viscosity modification with temperature. 6

Fig. 1.6. An electrochemical pump using electrolysis to pump liquid. 7

Fig. 1.7. Pump using solid propellant to generate gas to pump liquid. 7

Fig. 1.8. Schematic respresentation of a magnetohydrodynamic (MHD) pump. 8

Fig. 1.9. Schematic of capacitive micromachined ultrasonic transducer (cMUT). 8

Fig. 1.10. Electrohydrodynamic pump principle using thermally induced charge gradient. 9

Fig. 1.11. Basic electro-osmotic flow principle. 10

Fig. 1.12. Check valve acting as a flow rectifier. (a) Depiction of the valving mechanism, (b) valve is open, piston does not block flow (c) valve closed, piston blocks the flow. 12

Fig. 1.13. Diaphragm valves using (a) two and (b) one level capillaries. 13

Fig. 1.14. Electrostatically actuated valve (a) opened and (b) closed. 13

Fig. 1.15. Pneumatically actuated valves 14

Fig. 1.16. Thermopneumatically actuated valve. 14

Fig. 1.17. Thermal expansion valve. 15

Fig. 1.18. DNA nucleotide (a), single-stranded DNA (ssDNA) (b) and double-stranded DNA (dsDNA) (c).....17
Fig. 1.19 Polymerase chain reaction (PCR) of DNA.....18
Fig. 1.20 Restriction Endonucleases digestion of DNA. 18
Fig. 1.21. Gel Electrophoresis of DNA with gel electrophoresis device in cross shape with separation and injection channels. Device biased in injection mode (a), device biased in separation mode (b), fluorescent image of DNA during injection (c), injected plug in the separation column (d), separated bands of DNA (e) 19
Fig. 1.22. Sanger sequencing to read out the sequence of the DNA.....20
Fig. 1.23. Sanger sequencing to read out the sequence of the DNA.....22
Fig. 1.24. Traditional bench top analysis system.....24
Fig. 1.25. Proposed methodology to achieve integrated systems. 25
Fig. 1.26. An example of an integrated microfluidic system employing porous plug electro-osmotic pumps and thermally responsive polymer valves. 27
Fig. 2.1. Depiction of compact and diffuse layer concepts and potential profile between the walls of a channel and an aqueous liquid. Dimensions are not to scale. 31
Fig. 2.2. Potential profile inside a cylindrical channel with different radiuses assuming DI water of 7.5 μM ion concentration and ζ potential of 50 mv. 33
Fig. 2.3. Depiction of compact and diffuse layer concepts and potential profile at the electrode- solution interface.....37
Fig. 2.4. Qualitative behavior of C_d derived with Gouy-Chapman-Stern model over a wide potential range and electrolyte concentration. 38
Fig. 2.5. Depiction of electro-osmotic flow: double layer formation, dragging of liquid through surface charges with a tangential electric filed and resulting velocity profile. 38

Fig. 2.6. Volume flow rates for electro-osmotic flow at different electric field magnitudes and pressure driven flow at different pressure difference across 50-μm long cylindrical channel as the channel radius is scaled down. 41
Fig. 2.7. Maximum pressures that can be generated with electro-osmotic flow with the same assumptions used in Fig. 6 with different electric field magnitudes as channel radius decreases. 41
Fig. 2.8. EOF mobility decrease with decreasing channel dimension (with channel radius, double layer thickness ratio decreasing). 43
Fig. 2.9. Model of a porous structure as a pack of parallel cylindrical channels of radius *a*. 44
Fig. 2.10. Flow regimes and Reynolds numbers. 45
Fig. 2.11. Equivalent circuits of EOP. 47
Fig. 2.12. An example of microfluidic system and its equivalent electrical circuit. 48
Fig. 3.1. Equivalent electrical circuit of the electrochemical cell for small signals. 59
Fig. 3.2. More accurate equivalent electrical circuit of the electrochemical cell for small signals. 60
Fig. 3.3. Measured (o) and calculated (x) AC limit current of linearity of platinum electrodes in 0.01 M KCl solution vs. frequency. 61
Fig. 3.4. Illustration of the non-linear relationship between voltage and current of an electrochemical cell with large signal magnitudes. 62
Fig. 3.5. R_{ct} value calculated using equation (20) divided by the small signal R^0_{ct} value in equation (17) vs overpotential across the interface. 63
Fig. 3.6. Deviation from Butler-Volmer equation at even larger overpotential (a) and tafel plots of the same experimental results. 65
Fig. 3.7. Voltage response of an electrochemical cell to a constant current signal. 67
Fig. 3.8. Depiction of voltage response of an electrochemical with periodic current reversal. 67

Fig. 3.9. Applied current signal (top) and voltage response (bottom) for two electrode electrochemical cell (Electro-osmotic pump) with DI water. 68
Fig. 3.10. Setup to measure voltage response of porous plug electro-osmotic pump (pp-EOP).....69
Fig. 3.11. Measured and theoretical voltage response of the electro-chemical cell to current sweep. 70
Fig. 3.12. Potential of platinum electrode with respect to reversible hydrogen reference electrode (R.H.E) in response to biphasic current pulses of 50 mA/cm^2 magnitude [Bru77]. 72
Fig. 3.13. Measured voltage response of a vertical electrode device with a 65 μm long plug and a 30% duty cycle current input with +700 and -300 nA amplitudes at 5 Hz, not causing any net movement. 74
Fig. 3.14. Measured voltage response of a vertical electrode device with a 65 μm long plug and a 30% duty cycle current input with +700 and -300 nA amplitudes at 1 Hz, causing net movement.....75
Fig. 4.1. EOF pump schematic.....78
Fig. 4.2. Electrode configurations (a) planar (b) vertical (pillar) and corresponding equipotential and electric field lines for (c) planar (d) vertical. The units of plots (c) and (d) have been normalized with 1 corresponding to 25 μm. Flow is along x axis. 80
Fig. 4.3. Simulation results of two-dimensional planar (solid line) and vertical (dotted line) electrodes. First electrode is located at *x=0*. The gap between electrodes is *50 μm*. Applied voltage is *5 Volts*. The distance *y* is from substrate surface (0 μm) to 20 μm. 80
Fig. 4.4. Pore size distribution profiles of monolithic polymers with different percentages of 1-propanol. Percentage of 1-propanol in the porogenic mixture (1-propanol and 1,4-butanediol): peak 1) 80%; 2) 78%; 3) 76%; 4) 74%. 82

Fig. 4.5. Three step casting process of the porous polymer solution. After casting, solution is polymerized either by heat or *UV* exposure. After polymerization, since the liquid becomes solid with solvents inside the pores, wafers separate easily. 83
Fig. 4.6. Scanning electron micrograph (SEM) of patterned porous polymer plug. Patterning of the polymer was done by reactive ion etching unmasked areas. Ti was used as a mask, which was patterned by a lift-off process. 84
Fig. 4.7. Simplified process flow for a planar electrode pp-EOP device.....85
Fig. 4.8. Microscope photograph of a fabricated planar electrode pp-EOP device. 86
Fig. 4.9. Fabrication process flow for a vertical electrode pp-EOP device. 87
Fig. 4.10. Top view of a fabricated vertical electrode pp-EOP device. 87
Fig. 4.11. Resistance measurements of the device with and without the porous polymer. 89
Fig. 4.12. Electro-osmotic liquid (DI water) velocity versus applied voltage magnitude of two electrodes with a gap of 65 μm inside parylene channel and of planar and vertical electrodes with 65 μm long porous plugs in between.....91
Fig. 4.13. Characteristics of the applied current signal with duty cycle $D = t_p/(t_p+t_n)$, frequency $f = 1/(t_p+t_n)$ $(I_p \cdot t_p = I_n \cdot t_n)$. 93
Fig. 4.14. Water-air interface flow velocity measurement apparatus. 94
Fig 4.15. Water-air interface movement in a planar electrode device (left) forward (right) reverse. 94
Fig 4.16. Average velocity of water-air interface with straight channel as a function of drive frequency. 95
Fig. 4.17. Devices with "necked-down" channel from 200 μm to (left) 50 μm (right) 20 μm 95
Fig. 4.18. Average velocity as a function of frequency with *necked-down* channel from 200 μm to 50 (circles) and 20 μm (triangles). 96

Fig. 4.19. Water-air interface movement for vertical electrode device (a) forward (b) reverse. 97
Fig. 4.20. Average water-air interface velocities of a device with 130 μm long plug in response to different duty cycled step current signals at the same frequencies with same amplitude, duration products. 97
Fig. 4.21. Average water-air interface velocities of the device with 130 μm long plug as a function of frequency. 98
Fig. 5.1. Schematic of porous plug electro-osmotic pump (Pp-EOP) with liquid bridge connections. 101
Fig. 5.2. Hydraulic pressure generation due to electro-osmotic mobility difference. 105
Fig. 5.3. Top view of fabricated Pp-EOP with liquid bridge. 106
Fig. 5.4. Forward and reverse water-air interface movement with DC voltage applied and polarities reversed respectively. 106
Fig. 5.5. Water-air interface velocity versus applied DC voltage. 107
Fig. 5.6. Flow visualization with fluorescence detection of neutral markers, rhodamine b. 108
Fig. 5.7. Close up view of the porous plug region with neutral markers pumped in the downstream direction detected by their florescence. 108
Fig. 5.8. Schematic of new flow field effect transistor (flowFET). 109
Fig. 5.9. Case showing affected charges, electric field and liquid flow direction when a periodic, net zero average waveform is applied to V_d and its negative to V_g. Net flow can be achieved as long as the *change* in the zeta potential is synchronous with V_d. 110
Fig. 5.10. Induced charges and the affecting force on them due to normal and tangential components of the electric field on planar electrodes respectively (a). The resulting flow pattern on planar electrodes (b) 111

Fig. 5.11. Asymmetric electrodes to generate directional flow with AC electro-osmosis. 112
Fig. 5.12. Case showing affected charges, electric field and liquid flow on top of three electodes used for mixing liquids. 112
Fig. 5.13. Fabrication process for the flowFET. 114
Fig. 5.14. Top view of a fabricated new flowFET. 114
Fig. 5.15. Potential profile of the gate electrode/insulator/electrolyte interface. 116
Fig. 5.16. Equivalent circuit model of the metal electrode/insulator/electrolyte interface. 117
Fig. 5.17. Bead velocity vs. magnitude of V_d of a 1 KHz square wave, with V_g equals to V_d and $-V_d$. 119
Fig. 6.1. Preparation of resist like thermally responsive polymer. 123
Fig. 6.2. Fixture for the casting method. 124
Fig. 6.3. (Left) Top view of UV patterned polymer in 40 °C water. (Right) Same pattern in 15 °C water. 124
Fig. 6.4. Cross sectional view of patterned polymer inside DI water at different temperatures. 125
Fig. 6.5. Polymer's thickness change in DI water at different temperatures. 125
Fig. 6.6. Process flow for the photoresist like thermally responsive valve. 126
Fig. 6.7. Top view of a released valve 127
Fig. 6.8. Fixture used to test the polymer valve. 128
Fig. 6.9. Test setup to measure build-up pressure in front of the polymer. 129
Fig. 6.10. Top view of swollen polymer inside parylene channel shrinking with time as heater turned on (left column) and shrunk polymer swelling as the heater turned off (right column). 130
Fig 6.11. Pressure increase just after the valve is closed with a constant flow rate of 1 μm/min applied. 131

Fig. 6.12. Changes in the back pressure in the microfluidic channel containing 2 mm long macroporous NIPAAm-EDMA monolith. The microchip was submerged at time 0 in 42^0C bath..... 133
Fig. 6.13. Building of pressure in the channel containing monolithic valve. 133
Fig. 6.14. Response profiles for the monolithic valve using different gradients of temperature. The microchip was submerged at time 0 in bath with indicated temperature. 134
Fig 6.15. Microchip to test monolithic polyNIPAAm valve. 135
Fig. 6.16. Optical micrograph of the monolithic valve. 136
Fig. 6.17. Designed of a microchip with enhanced rate of heat transfer. TE is the thermal electrical cooler/heater (Peltier element). 137
Fig 6.18. Single valve action..... 138
Fig 6.19. A closer view of single valve action: opening (left) and closing (right) of the valve. 138
Fig 6.20. Sequential opening and closing of a single polyNIPAAm 139
Fig. 6.21. Differential scanning calorimetric trace enabling determination of LCST. ... 141
Fig. 6.22. LCST of gels as a function of the molar fraction of NEAAm in the copolymer. 142
Fig. 6.23. Environmental scanning electron micrographs of the crosslinked poly(NIPAAm-co-NEAAm) valve in wet (left) and dry state (right)..... 143
Fig. 6.24. Optical microscopic monitoring pore size of poly(NIPAAm-co-NEAAm) valve at position open using fluorescently labeled monodisperse beads. (a) and (b) are taken at the same point at different times illustrate flow of 2 μm polystyrene microspheres through the valve. (c) shows accumulation of monodisperse FITC-labeled 7.2 um poly(glycidyl methacrylate-co-ethylene dimethacrylate) beads in front of the valve. 144

Fig. 6.25. Pressure building within an open capillary containing valve in position close (□) and empty capillary sealed at the end (●). 145
Figure 6.26. Monitoring of the valving function of 2.5% crosslinked poly(NIPAAm-co-NEAAm) monolith in straight channel using photobleaching of 100 nmol/L aqueous Coumarin 519 solution at a flow rate of 1 μL/min. Inlet: expanded part of the profile. 146
Fig. 6.27. Monitoring of the valving function of 2.5% crosslinked poly(NIPAAm-co-NEAAm) monolith in M shaped microfluidic system that includes two valves using photobleaching of 100 nmol/L aqueous Coumarin 519 solution at a flow rate of 1 μL/min. (a) original trace; expanded parts of (b) opening and (c) closing profiles.148
Fig. 6.28. High frequency valving operation of the 2.5 % crosslinked poly(NIPAAm-co-NEAAm) monolithic gels in the M-shaped two valve microfluidic system actuated every 10 s. 149
Fig. 7.1. Test structures showing large-scale integration of porous plug electro-osmotic pumps. 157

LIST OF TABLES

Table 2.1. Molar conductivities of different anions and cations in water.....35

Table 2.2. Hydraulic resistance formulas for different channel types. 47

Table 5.1. Different cases of a periodic net zero average waveform applied to driving voltage (V_d) and gate voltage (V_g)..... 110

Table 6.1. Flow resistance of a monolithic valve located in a capillary at different flow rates. 132

SECTION 1

MICROPUMPS, VALVES AND MICRO TOTAL ANALYSIS SYSTEMS

1.1 Introduction

Fully integrated microfluidic systems are highly effective because they can completely automate analytical procedures, reduce consumption of organic or chemical reagents significantly [Har93] and speed up analysis time. Therefore, these kinds of systems have become an interest of many research groups, referring them as lab-on-a-chip or micro total analysis system [Rey02]. A complete complex system may require many pumps and valves operated simultaneously or sequentially to precisely control the liquid flow from one part of the system to another. It is hence imperative that these pumps and valves must be easy to fabricate and integrate with the other components of the system [Car00]. This work focuses on fabrication of these simple pumps and valves with no moving parts for large scale integration to realize a fully integrated microfluidic system.

The following two sections discuss some common micropumps and valves that have been explored in the literature so far and why electro-osmotic pumps and thermally responsive polymer valves have been chosen to build an integrated microfluidic system. This is followed by some analysis methods where the integrated microfluidic systems have found uses. Finally, the section is concluded by the proposed methodology for the system integration using these pumps and valves and then report organization.

1.2 Micropumps

Since transport of the liquid is the most basic and important operation in the microfluidic system, pumps play a key role in system's versatility and complexity. In many applications, since portable, stand-alone systems are much needed, an external pump is not favored. In addition, since this microfluidic system will often be accompanied by an electronic circuit to initiate and sequence its tasks, any integrated pump should have low power consumption and should require voltage and current levels within the limits that can be produced by the current electronic circuits and their standard power supplies. Up to now, many different micro pump devices have been proposed. In the current technology, we can separate pumps into two categories: mechanical and non-mechanical pumps.

1.2.1 Mechanical Pumps

Mechanical pumps usually employ a moving diaphragm or a mechanical structure actuated electrostatically [Zen95], thermo-pneumatically [Zde94], piezoelectrically [Lin88] or electromagnetically [Zha96] to move liquid. However these pumps usually have complicated fabrication processes and have moving parts causing reliability problems due to mechanical wearing. Except for the actuation scheme, structures of these pumps are very similar to each other. Furthermore these pumps need a flow rectification scheme in order to have a directed flow. These rectification schemes are summarized next.

1.2.1.1 Flow Rectification For Mechanical Pumps

The diaphragm of a mechanical pump moves back and forth. This would displace and replace same liquid volume resulting in no net motion unless the forward flow faces same conditions as the reverse flow. Therefore, the bi-directional motion generated by the diaphragm must be rectified in order to have a directional pumping. This can be done using one of the following flow rectification schemes: check valves, diffuser-nozzle configuration, peristaltic motion, dual diaphragm pumping and modification of the liquid viscosity with temperature.

Check Valves

Many stand alone mechanical pumps uses check valves to rectify the flow. These pumps have two directional check valves allowing flow only in one direction, very similar to a diode in electrical circuits. An example is shown in Fig. 1 with an electrostatic actuation [Zen95]. In this example, when the diaphragm moves up, it sucks liquid from the inlet and the outlet. However the outlet check valve closes with this motion not allowing any back flow from the outlet to the inlet. However the inlet valve is open, so it lets liquid into the chamber. When the diaphragm moves down it pushes the liquid into the outlet and the inlet. In this case, the inlet valve is closed and the outlet valve is open, again allowing flow only in one direction. Unfortunately there are not any good planar check valves. Therefore most of these pumps have out of plane liquid flow, complicating the integration of the fluidic system. Furthermore check valves add more moving parts, making the fabrication more complex and causing further reliability issues.

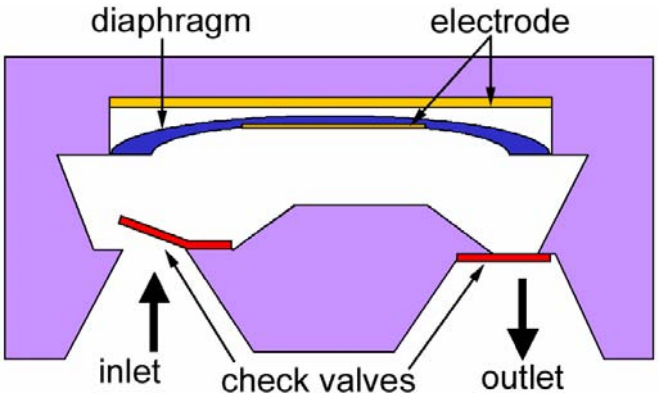

Fig. 1.1 Electrostatically actuated micropump with check valves.

Diffuser-Nozzle Configuration

Diffuser-nozzle configuration is a valveless flow rectification scheme. Therefore, it does not have any additional moving parts and it works well with planar design too. Directionality is achieved by the asymmetry in the geometry between the inlet and the outlet of the pump. In the supply mode, when the diaphragm moves up, it sucks liquid from the inlet and the outlet. However because of the geometry, inlet acts as a diffuser and the outlet as a nozzle. Therefore more liquid moves from the inlet into the chamber

than from the outlet as shown in Fig. 2 [Ols99]. In the pump mode, when the diaphragm moves down, it pumps liquid into the inlet and the outlet. However now the inlet is the nozzle and the outlet is the diffuser, therefore more liquid is pumped from the chamber to the outlet than to the inlet. As a result, even though this scheme does not rectify the flow fully, it gives a favorable flow in one direction.

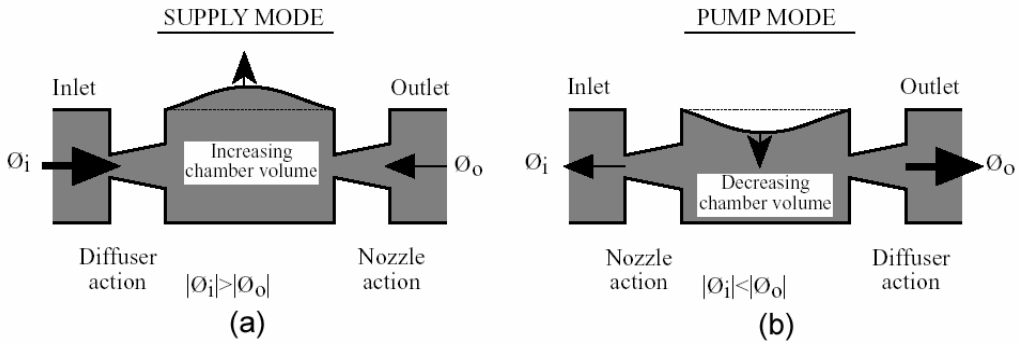

Fig. 1.2.Valveless diffuser-nozzle configuration [Ols99].

Peristaltic Motion

Another way to rectify a liquid flow is to use a peristaltic motion. This is achieved by having several pumps in series and operating them with a sequence. An example is shown in Fig. 3 with three pumping chambers and three-phase actuation sequence [Gro99]. The motion can be effectively established by actuating two of the diagrams in their chambers so that they would block the back flow and move the liquid in the inactivated chamber to the chamber next to it. Employing different sequences is also possible. Similar to the diffuser-nozzle configuration, its advantage is that it is compatible with planar design therefore friendly to integration attempts.

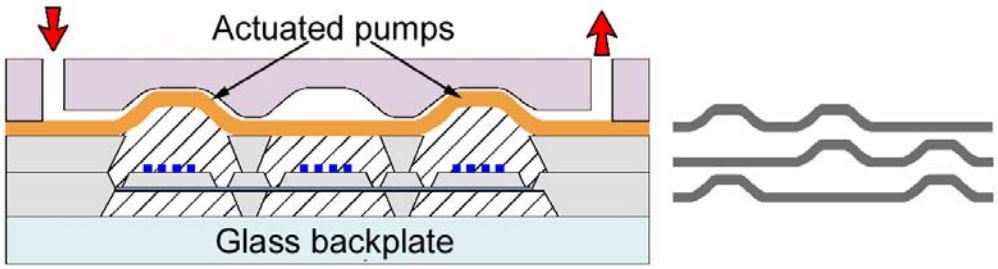

Fig. 1.3. Peristaltic pump with three chamber (left) and three-phase chamber activation sequence (right) [Gro99].

Dual Diaphragm Pumping

This specific design with two diaphragms combines diagram and check valve function together. Instead of using separate moving parts for the check valves, one of the diaphragms serves as a check valve while the other does the actuation. An example of two electrostatically actuated diaphragms in a chamber is shown in Fig. 4 [Cab01]. Diaphragms are actuated in a specific order as explained in the figure. However this scheme seems possible only in out of plane liquid flows.

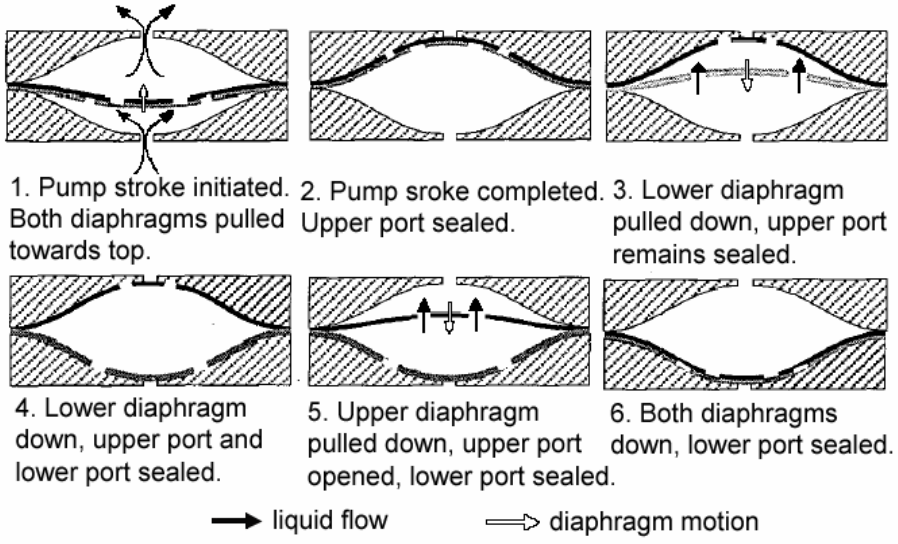

Fig. 1.4. Dual diaphragm pump [Cab 01].

Thermal Viscosity Modification

This rectification scheme takes advantage of the viscosity of the liquid change with temperature. If microheaters are placed in the inlet and outlet of the diaphragm chamber, temperature of the liquid there can be controlled. Liquid viscosity decreases with the increase in temperature. With low viscosity, more liquid volume can be displaced. An example is shown in Fig. 5 with a piezoelectrically actuated diaphragm [Mat99]. When the diaphragm moves up, it pumps the liquid in the chamber into the inlet and the outlet. Only the heater in the outlet is on. Therefore liquid viscosity in the outlet channel is low and more liquid will be displaced through the outlet than the inlet. When the diaphragm moves down, it sucks liquid from the inlet and the outlet. Now only the inlet heater is on. Therefore flow from the inlet into the chamber is more than the one

from the outlet. This way flow rectification can be achieved depending on which heater is on.

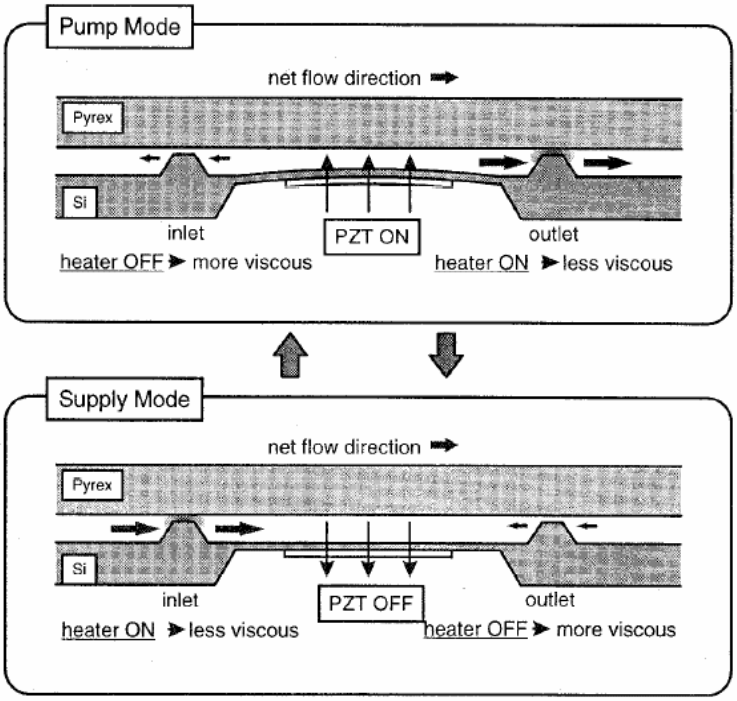

Fig. 1.5. Flow rectification by liquid viscosity modification with temperature [Mat99].

1.2.2 Non-Mechanical Pumps

Non-mechanical pumps like electro-chemical [Boh99], magnetohydrodynamic [Lem99], ultrasonic, electrohydrodynamic [Bar90] and electro-osmotic [Man94, Bur64, Ram98, Fuj02, Sel02, Che02] pumps do not have any moving parts and hence are potentially more reliable and easier to fabricate.

1.2.2.1 Electrochemical Pumps

One of the most common electrochemical pumps uses electrolysis to form bubbles to move liquid [Boh99]. A microchannel equipped with two electrodes is enough to implement this pump as shown in Fig. 6. Hence it is very easy to fabricate and integrate this pump into dosing systems. Disadvantages of this scheme are the consumption of the working liquid and difficulty to eliminate once formed bubbles. Another kind of

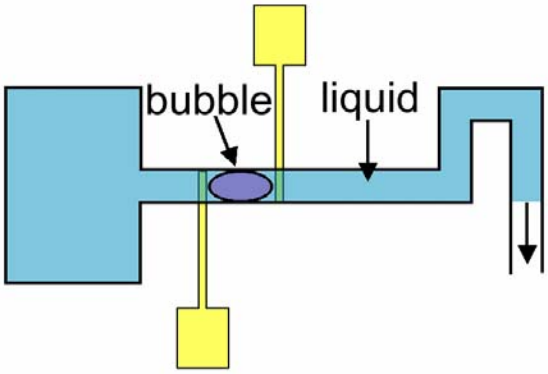

Fig. 1.6. An electrochemical pump using electrolysis to pump liquid.

electrochemical pump uses solid propellant chemicals to generate gas that can move the liquid. An example of this is shown in Fig. 7 [Cho03]. In this case a solid propellant, azobis-isobutyronitrile (AIBN) is heated with a microheater to produce nitrogen gas. The gas generation rate can be controlled with the microheater power to the desired amount of pressure to drive liquids.

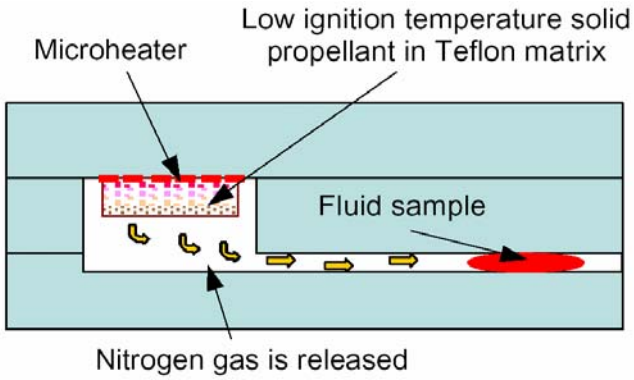

Fig. 1.7. Pump using solid propellant to generate gas to pump liquid [Cho03].

1.2.2.2 Magnetohydrodynamic Pumps

Magnetohydrodynamic pumping uses Lorentz force to move the liquid [Lem99] as shown in Fig. 8. Its disadvantage is the need for external magnet sources and conduction of high currents that can heat up the liquid. Also electromagnetic forces do not scale down well since magnetic force is inversely proportional to the third power of the dimension [Tri89].

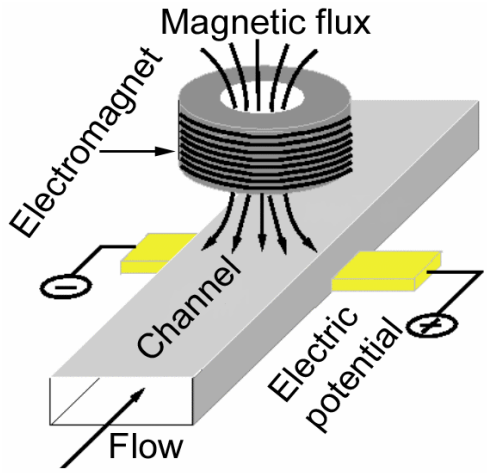

Fig. 1.8. Schematic respresentation of a magnetohydrodynamic (MHD) pump.

1.2.2.3 Ultrasonic Pumps

Ultrasonic transducers can be used to pump or mix liquids. Flexural plate wave (FPW) devices use piezoelectric materials fabricated on thin membranes to generate acoustic waves. The transducer is simply a piezoelectric film with electrodes patterned on its both sides. A high density acoustic wave generated by the ultrasonic transducer is

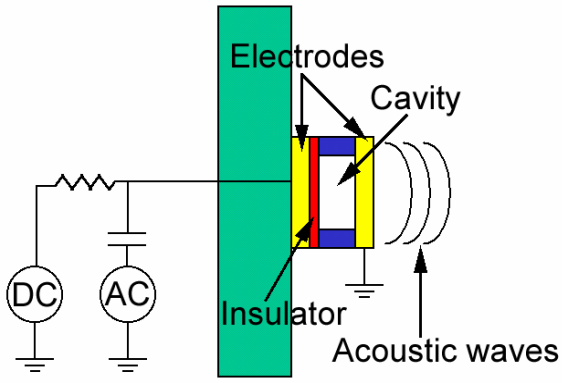

Fig. 1.9. Schematic of capacitive micromachined ultrasonic transducer (cMUT).

absorbed and scattered while propagating in the medium. Since the attenuation of the intensity of the wave is nonlinear, it causes the medium itself to move. This phenomena is called acoustic streaming. With an ultrasonic transducer like this, nozzleless jet streams

of air or liquid can be achieved [Yu03]. Another kind of ultrasonic transducer is a capacitive micromachined ultrasonic transducer (cMUT). A schematic of this device is shown in Fig. 9. This device is surface micromachined, can be compatible with CMOS and also can be used to sense the fluid's viscosity, density and temperature in addition to pumping and mixing [McL03]. However cMUT fabrication can be complicated due to the need for capacitive cavity sealing.

1.2.2.4 Electrohydrodynamic Pumps

Electrohydrodynamic pumps move the liquid by dragging it with an electric field exerted on the induced charges in the bulk of the liquid. Inducing charge in the liquid

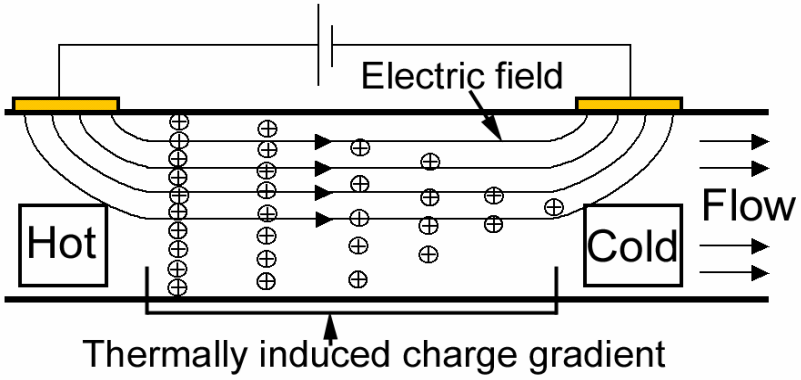

Fig. 1.10. Electrohydrodynamic pump principle using thermally induced charge gradient.

can be done by creating thermal gradient as shown in Fig. 10 or applying a traveling wave potential on the electrodes placed in the flow direction. However these pumps can usually operate on liquids with very low conductivities, like oil. Even though pumping of aqueous solutions has been shown with traveling wave potential [Fuh94], it requires frequencies in the several hundred MHz range, complicating driving circuits.

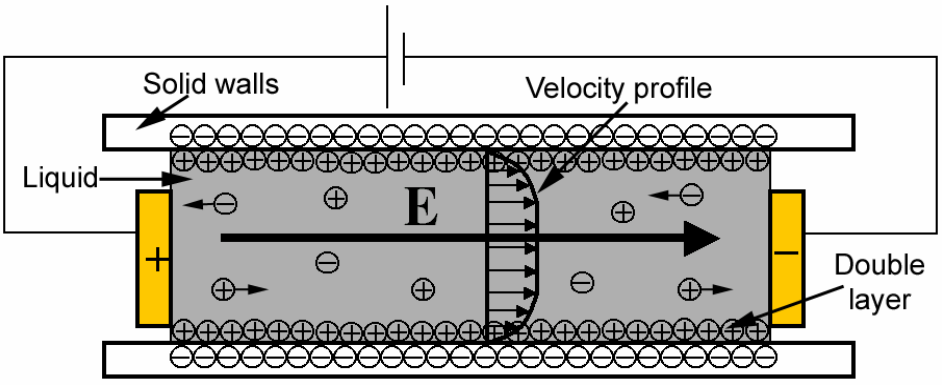

Fig. 1.11. Basic electro-osmotic flow principle.

1.2.2.5 Electro-osmotic Pumps

Electro-osmotic pumps (EOP) move aqueous solutions by dragging them from charges formed in the electric double layer between the solid and liquid interface by applying an electric field [Sha69]. This is depicted in Fig. 11. Most solid surfaces form these finite charges once they are in contact with an aqueous liquid. For example, contact between glass and water causes the glass surface to be charged because of deprotonation of surface silanol groups [Che02]. They have received much attention for biological applications such as capillary electrophoresis systems because they are easy to fabricate and integrate, can handle aqueous based liquid and create very little hydrodynamic dispersion when transporting fluid zones [Man94]. That is why in this work, EOPs are chosen for the realization of an integrated microfluidic system.

However, there are a number of issues associated with conventional EOPs, which prevent them from realizing their full potential in integrated microfluidic system. In aqueous solutions, electrode potentials larger than 1.2 V cause electrolysis followed by bubble generation, which might lead to blockage of the EOP channel if electrodes are placed inside the channel. Other researchers eliminated this by placing the electrodes across the channel at open areas such as reservoirs where bubbles can escape. Because the distance between electrodes in this scheme is large, significant flow velocities require very high voltages, beyond the range of any on chip flow control electronics.

Current microfluidic devices have mostly open channels with dimensions in the scale of tens of microns. In this scale, pressure driven flow is dominant over electro-osmotic flow. Therefore, once EOF starts pumping liquid, it causes pressure difference in these open channels. However this hydrostatic pressure build up wants to pump the liquid against EOF direction hence causing counter flows [Ric65]. This counter flow can be very large if EOP is implemented in short channels. Volume flow rate of pressure flow is proportional to r^4, where r is the radius of the channel, while that for electrokinetic flow is only r^2. That is why the use of a micromachined porous plug between the electrodes can create a high flow resistance reducing the pressure driven counter flow substantially while allowing electrokinetically generated flow. This also allows close placement of driving electrodes, assuming the electrolysis problems are solved, achieving the same flow rates, with lower drive voltages as low as 2-3 V. Previously used porous structures were either builtby packing silica beads [Pau98] or in situ polymerization of the plug inside microfluidic channels [Yu00], both of which make complex designs unrealizable and hence unsuitable for an integrated system. That is why recently, research efforts have utilized micromachined porous structures by having multiple narrow (around 1 μm) channels in parallel formed lithographically [Sel02b]. However, still this approach does not eliminate pressure driven flow significantly and the active area is much smaller than what a porous polymer can offer. That is why in this work, a new kind of an electro-osmotic pump, a porous plug electro-osmotic pump (Pp-EOP) has been developed and different driving schemes have been used as will be explained in the coming sections.

1.3 Microvalves

Microvalves can be divided into three groups: active, passive and hydrogel valves. Active valves are actuators that convert different kinds of energy into actuation of diaphragms to block or open a channel for flow. Passive valves however do not have this actuation scheme [Car01]. They just have mechanical moving parts that were activated by the flow itself. Hydrogel valves do not have any moving membrane or moving mechanical part. A patterned smart material inside the channel swells and shrinks in response to different kind of stimuli in the liquid and blocks or opens the channel. An ideal valve should be easy to fabricate, consume low power, have very small dead

volume, withstand high pressures without any leakage, should not contaminate the liquid under investigation, have small dimensions and be large-scale integratable.

1.3.1 Passive Valves

Passive valves are usually used as check valves. These are flow control components that allow flow only in one direction. This way they can rectify the bi-directional flow generated by micropumps. In that respect it is analogous to a diode in electrical circuits. A very good example to this is the nonstick polymer piston patterned in the glass capillary by in situ polymerization [Has03]. As shown in Fig. 12, this freely moving polymer piston passes flow only in one direction, while it stops the flow in the other direction with very small dead volume. Another example for a passive valve is the stop valve. These valves are usually one-time use valves. The flow in the valve region is stopped either by a pressure barrier or a hydrophobic surface. Once the applied pressure exceeds this barrier, the liquid flows through the valve and the valve cannot stop the flow anymore [Man08]. These valves are used for sample injectors.

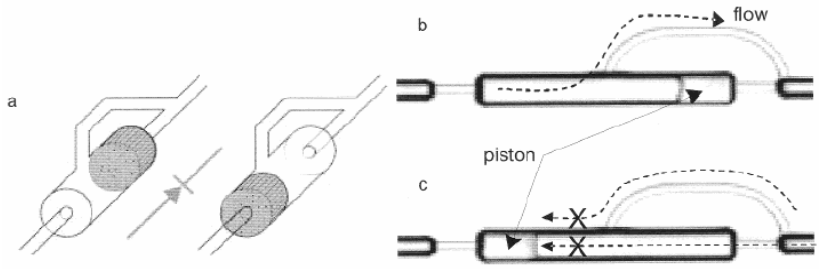

Fig. 1.12. Check valve acting as a flow rectifier. (a) Depiction of the valving mechanism, (b) valve is open, piston does not block flow (c) valve closed, piston blocks the flow [Has03].

1.3.2 Active Valves

Active valves use moving diaphragms to stop or allow a liquid flow through a channel. This can be done in two different schemes. Two capillary levels as shown in Fig. 13a. can be used. Even though this provides good seal it complicates the fabrication process and makes large-scale integration difficult. Diaphragm inline valves employing a single capillary level are simpler; however, since most micro channels are rectangular, voids always exist resulting in poor sealing as shown in Fig. 13b.

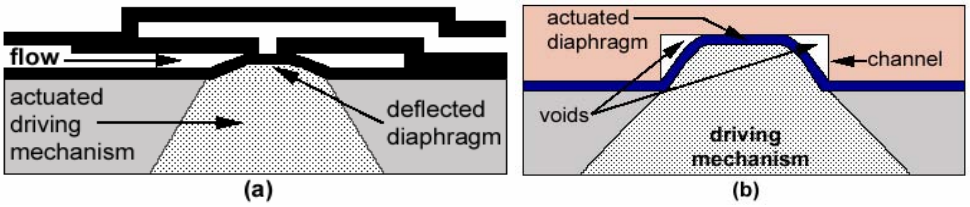

Fig. 1.13. Diaphragm valves using (a) two and (b) one level capillaries.

Different mechanisms are used to actuate diaphragms based on electrostatic, magnetic, piezoelectric, bimorph, shape memory alloy, pneumatic, thermopneumatic [Sho94] and thermal expansion methods [Car01]. Different valve designs and their comparisons have been reported elsewhere [Sho94], [Bar95]. However, several valve examples are included here.

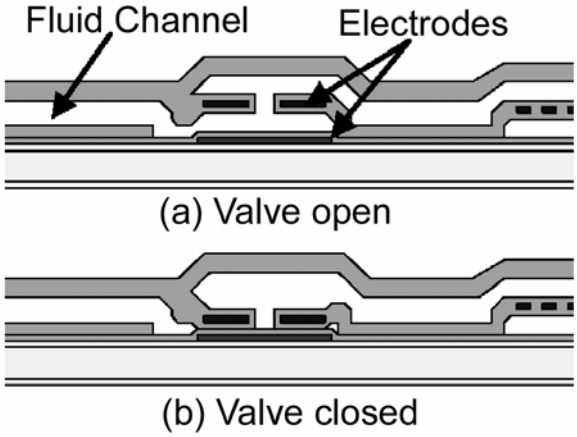

Fig. 1.14. Electrostatically actuated valve (a) opened and (b) closed [Xie03].

A good example of an electrostatically actuated valve is shown in Fig. 14 [Xie03]. A voltage of around 200 volts must be applied to the electrodes in order to close the valve. A high voltage requirement is one disadvantage of these valves even though power consumption is very small. Another disadvantage of these valves are charging of the insulating layer and stiction [Rob94] after repeated actuation.

A good example of pneumatically actuated valves [Ung00] can be seen in Fig. 15 and their large-scale integration can be found in [Tho02]. By making multi layer microchannels out of soft flexible material like silicone, fluid flow in the main flow

channel can be stopped by introducing air pressure to the control channels. This swells the control channels and blocks the main fluidic channel. Even though this is a good example of how simple valves like these can be large-scale integratable and form an integrated microfluidic system, the need for big external air pressure pumps put a limit to the size and portability of the overall system.

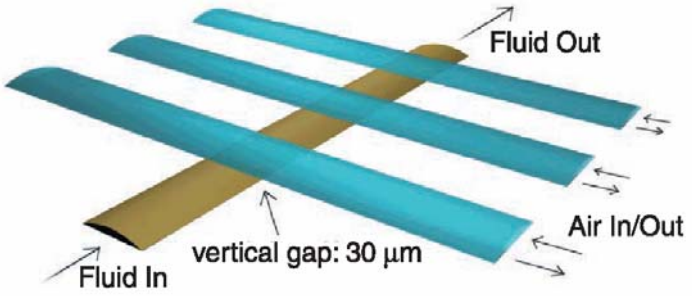

Fig. 1.15. Pneumatically actuated valves [Ung00].

Thermopneumatic valves use microheaters in a sealed cavity filled with air or a volatile fluid so that generated heat at microheaters increases the pressure inside the cavity and moves the diaphragm to block the channel. These valves are usually made by bonding wafers together, filling cavities with a fluid and sealing afterwards. A good example is shown in Fig. 16 [Ric03]. Size of the cavity puts a limit to the device size.

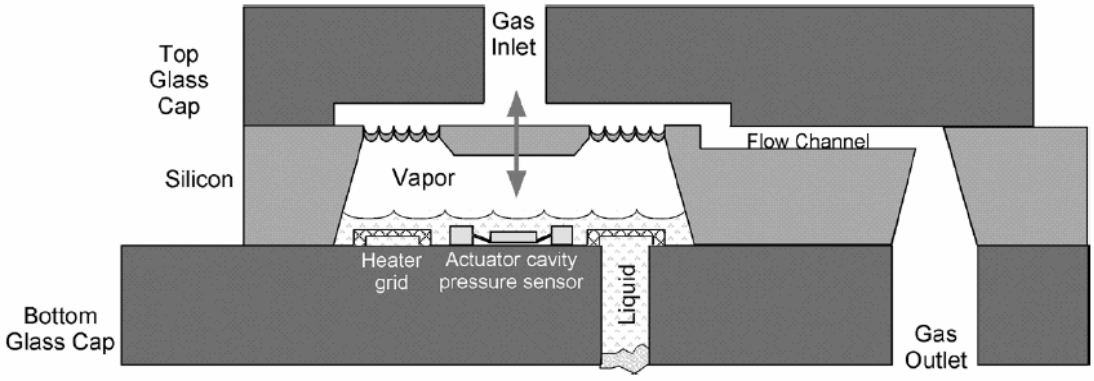

Fig. 1.16. Thermopneumatically actuated valve [Ric03].

Valves working on thermal expansion of polymers have also been fabricated. A good example of this is the thermal expansion of a sealed patch of surface micromachined paraffin. Its operation is shown in Fig. 17 [Sel03a]. These valves can be easily large-scale

integratable to form a fluidic analysis system. Low-temperature processing steps (< 65 °C) to prevent paraffin overflowing can be problematic in system integration. Also leakage of paraffin from its sealed reservoir due to a failed parylene membrane after several heating cycles can be a problem.

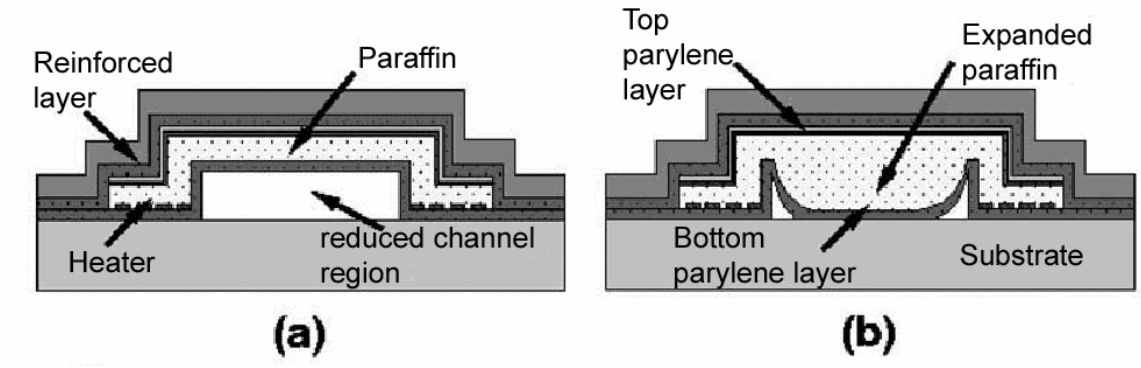

Fig. 1.17. Thermal expansion valve [Sel03a].

1.3.3 Hydrogel Valves

Hydrogel valves use hydrogels that undergo reversible volume change (swelling) with pH [Liu02], glucose concentration and temperature [Gu02,Yu03] of the liquid in which they are immersed thus plugging the microchannel. Since volume expansion of these materials can be very high, from 20% to 300%, they provide a good seal and ease the fabrication process unlike diaphragm actuators where movement can be maximum around 20% of the diaphragm dimension. So they are easier to fabricate and integrate and potentially can be more reliable. That is why in this work a thermally responsive polymer valve has been chosen for the integrated microfluidic system. Presently hydrogel materials are patterned by selective deposition or in-situ polymerization on (or between) pre-fabricated surfaces. However this work describes a microfabrication technique developed for a photoresist-like thermally responsive polymer and its integration into parylene microchannels with embedded microheaters to realize a surface micromachined inline valve as will be explained in section 6.

1.4 Analysis Methods

Integrated microfluidic systems will have wide spread usages because the clinical and life sciences have a tremendous need for DNA, protein and cell information. The number of biological or chemical analyses that need to be done is very high and increasing rapidly. Analysis methods summarized here are far from being a complete list, such as the micropump and valve summary. In this section, some of the basic analysis methods have been introduced to give an idea of what kinds of tasks need to be performed on integrated microfluidic systems because at the end these systems must be application specific. Their design and fabrication will be according to the application in mind. Current analysis systems can be divided into many categories some of which are: DNA, protein, cell and chemical analysis.

1.4.1 DNA Analysis

Genetic information of all living things is stored in the cell chromosomes. Chromosomes are long, very compact linear polymer strands of supercoiled deoxyribonucleic acid (DNA). Genes are long strings of DNA fragments grouped on chromosomes and determine characteristics of an individual. DNA is composed of nucleotides. Each nucleotide consists of a base, a sugar linkage and a phosphate bridge as shown in Fig. 18. Carbon atoms in the sugar of the nucleotide are numbered from 1' to 5', and the nucleic acid strand has free hydroxyl (or phosphate) on 3' and 5' carbon atoms [Sel03b]. There are four types of nucleotides depending on the type of base they have, which can be one of the four: adenine (A), guanine (G), cytosine (C) and thymine (T). Different numbers and combinations of these nucleotides combine together to form a single-stranded DNA (ssDNA). SsDNA molecules attach to each other through hydrogen bonds between the complimentary bases. This is called hybridization. Adenine-thymine

and guanine-cytosine are complementary of each other. Then they form double-stranded DNA (dsDNA) [Web99].

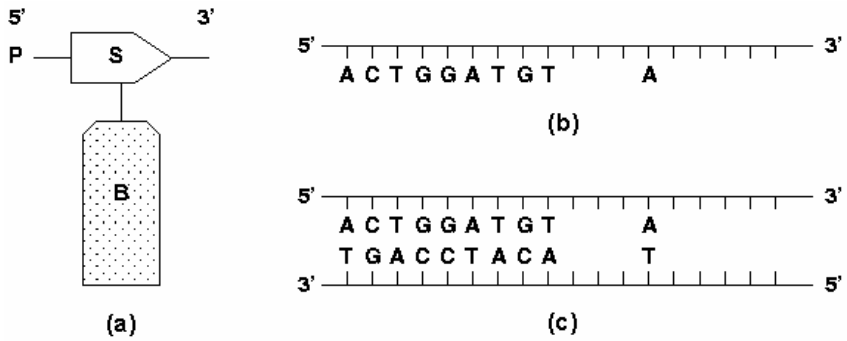

Fig. 1.18. DNA nucleotide (a), single-stranded DNA (ssDNA) (b) and double-stranded DNA (dsDNA) (c).

1.4.1.1 Polymerase Chain Reaction

Concentration of DNA samples may be too low for detection. Therefore before detection, DNA concentration may need to be amplified by replicating the original sample. This is done with a process called polymerase chain reaction (PCR). The process steps are shown in Fig. 19. It takes place in a sealed chamber where there are DNA templates, taq polymerase enzymes and adequate amounts of nucleotides and primers. Taq polymerase enzymes have the ability to scan single strands of DNA from the 5' to the 3', capture matching nucleotides from the solution and to connect them to a single strand one base at a time starting at a specific location. Primers are synthetic chains of nucleotides that bind to ssDNA at specific locations and determine the starting point of replication. The amplification starts with denaturing the template DNA into single strands by heating the chamber to 95 °C. Then the temperature is decreased to 60 °C where primers hybridize to the ssDNA. The polymerase enzyme then extends the primers and replicate the DNA molecule. After one step, DNA concentration is doubled. By repeating this process steps many times, the desired level of concentration can be achieved [Web99].

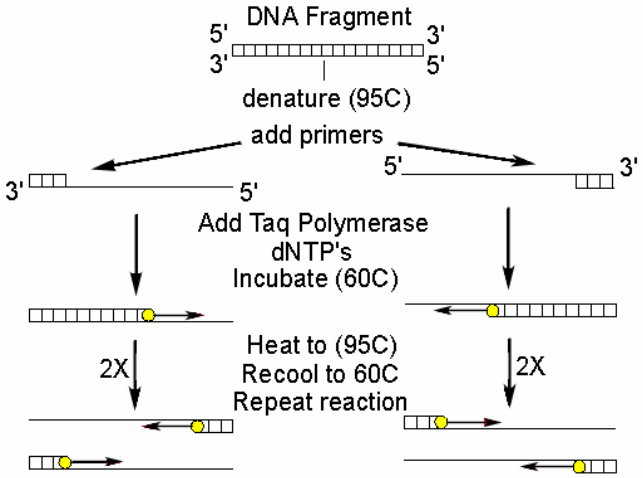

Fig. 1.19 Polymerase chain reaction (PCR) of DNA.

1.4.1.2 Restriction Endonucleases Digestion

DNA molecules are very long, up to thousands of base pair (bp) long. They have to be cut at specific locations in order to analyze them easily. Restriction endonucleases enzymes split dsDNA at specific locations. Typical restriction enzymes recognizes DNA sequences of four to eight base pairs and cut the DNA at these sites. Some restriction enzymes are shown in Fig. 20. Then the resulting DNA fragments can be separated according to size by gel electrophoresis [Man01].

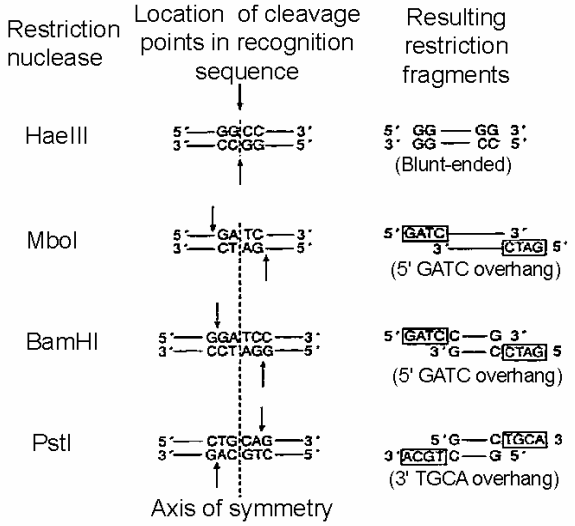

Fig. 1.20 Restriction Endonucleases digestion of DNA. 16

1.4.1.3 Electrophoresis

Electrophoresis is used to separate different sizes of DNA fragments from a mixture. If across a long channel a potential is applied, there will be an electric field in one direction. Since DNA molecules are charged, they would have a constant velocity with respect to liquid due to this electric field (electrophoretic mobility). This phenomenon is called electrophoresis. In gel electrophoresis, the long separation channel would be occupied with a polymerized gel, which has complex polymeric chains that forms a porous structure. DNA can pass through the gel but the gel raises a resistance to the DNA movement. Since gel's flow retardation is different for different sized DNA fragments, along a long separation channel, different sized DNA molecules will separate from each other while same sized ones stay close to each other forming individual bands of DNA. Usually electrophoretic separation devices have two channels: injection and separation, crossing each other as shown in Fig. 21. The injection channel is used to inject a defined sized plug of sample DNA into the separation channel. With the voltage

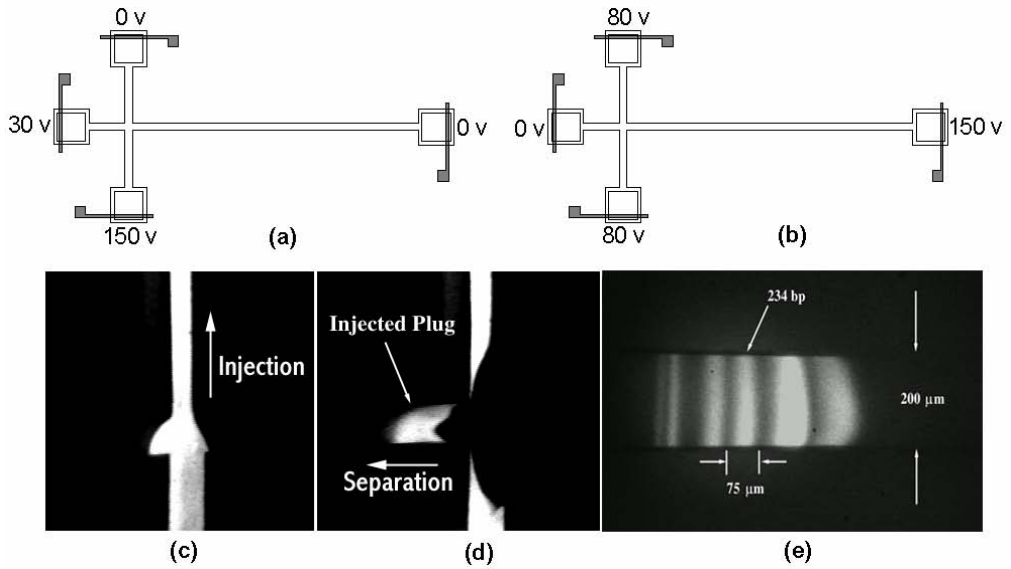

Fig. 1.21. Gel Electrophoresis of DNA with gel electrophoresis device in cross shape with separation and injection channels. Device biased in injection mode (a), device biased in separation mode (b), fluorescent image of DNA during injection (c), injected plug in the separation column (d), separated bands of DNA (e) [Web99].

configuration in Fig. 21a, DNA will flow in the injection channel as shown in Fig. 21c. Once the voltage configuration is changed to the one as in Fig. 21b, a plug of DNA sample of a predetermined size will be injected into the separation channel as shown in Fig. 21d. Then the DNA will be separated in the separation channel according to size and bands of DNA will form as shown in Fig. 21e. For example, suppose the investigated sample is a 50 base pair DNA ladder. That means the mixture has DNA with base pair sizes of multiples of 50 like 350,400,450,500 ,550 and 600 bps. Then after the separation the first band will have only 350 bp DNA since it is the smallest and will be the fastest. Then comes 400, 450 bp and so on and the last band will consist of only 600 bp DNA. These bands can be detected with an embedded photodiode, if DNA was tagged with a florescence dye and excited with a UV light [Web99].

1.4.1.4 Sanger Sequencing

Sanger sequencing is used to read out the single base sequence of a DNA. This is

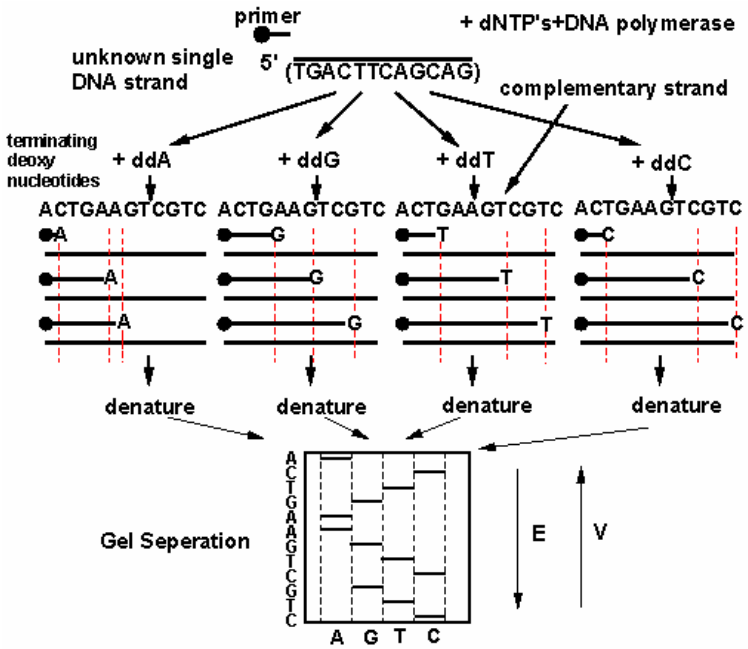

Fig. 1.22. Sanger sequencing to read out the sequence of the DNA.

shown in Fig. 22. Since sequencing of DNA requires single base pair resolution, the long DNA sample has to be cut into single base fragments. This is done in the amplification step of the process. Similar to PCR, amplification of the DNA starts at the primer location, but it is randomly terminated at locations where a specific base is present. Dideoxynucleotide triphosphate (ddNTP) are special nucleotides that terminate the polymerase duplication when captured. There are four types of them: ddATP, ddCTP, ddGTP, ddTTP. Introduction of a small concentration of dideoxynucleotides of one particular type causes this random termination. These reactions are done in four different chambers with each chamber having only one specific dideoxynucleotide. Then depending on the type of ddNTP in the chamber, each chamber will have different sized DNA fragments that have been terminated from all possible base locations of that ddNTP in the sequence of the original DNA. After that, if these DNA mixtures of different sizes are separated with electrophoresis in four different separation channels, the real sequence of the original DNA can be extracted from the relative positions of DNA bands in each separation channel [Web99].

1.4.1.5 Hybridization Techniques

Hybridization is the hydrogen bonding of two complementary ssDNA. In hybridization based analysis system, the substrate will have arrays of ssDNA with different sequences attached to the surface. Sequences of these attached DNA and locations of each array in the chip are known. Once the unknown sample is introduced, it will attach itself only to its complementary forming a double strand. Then formation of this double strand is detected by fluorescence. This is shown in Fig. 23. Electrochemical detection or cantilever-based devices (where arrays of ssDNA are patterned on cantilevers and their deflections after hybridization are measured) can also be used for

detection [Sel03b]. The hybridization technique is widely used and its main advantage is its tremendous parallelism present in large arrays. However only limited number of combinations of DNA sequences can be put on a chip.

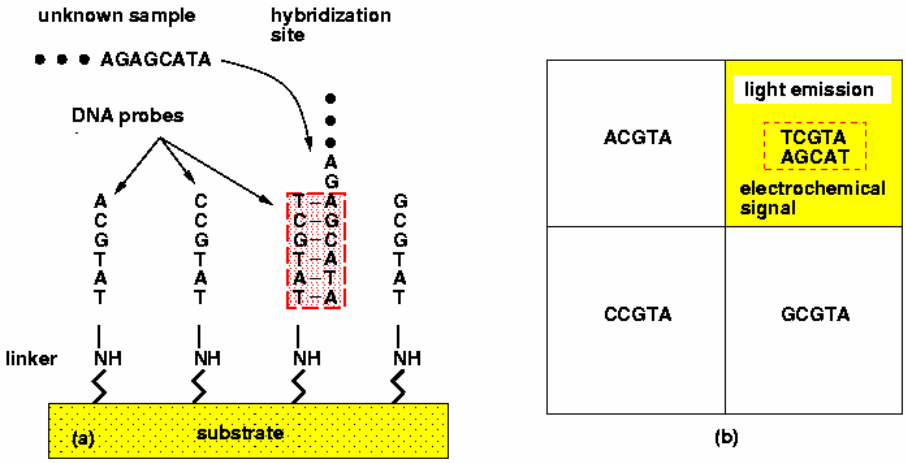

Fig. 1.23. Sanger sequencing to read out the sequence of the DNA [Web99].

1.4.2 Protein Analysis

Like DNA, proteins can be digested, separated, bound to a surface and tagged with markers [Sel03b]. DNA analysis systems have started to become mature. Similar systems developed for DNA can also be used for protein analysis.

1.4.2.1 Protein separation

Chromatography and electrophoresis are the two major separation techniques for proteins [Kha02].

1.4.2.2 Protein detection

Antibody (Ab) or immunoglobulin is a protein produced by the immune system of animals in response to the invasion of a foreign molecule. This foreign molecule is antigen (Ag) and it can be any substance that is specifically recognized by the antibody.

Immunoassays are analytical experiments that are carried out to identify and quantify target molecules through the usage of specific bindings of antibodies. Antibody based immunoassays are widely used to identify proteins, hormones, peptides and low molecular weight molecules. [Sel03b]. They represent a very important tool in clinical diagnostics and biomedical research and industry [Kha02].

1.4.3 Chemical Analysis

Detection of impurities, concentration of metal ions or chemicals in water can be achieved using integrated microfluidic systems. It requires integration of detection systems like mass spectroscopy.

1.4.4 Cell Analysis

Individual cells can be trapped on the device, and surrounded by microfluidic channels that can deliver different chemicals to the cell and electrodes that can measure its membrane potential or apply potential. Then under a microscope the reaction of the cell to different chemical or electrical stimuli can be monitored. By applying voltages to the cells, cells may be forced to divide or unite with another cell (electrofusion) or cause a pore formation in the cell membrane (electroporation).

1.5 Advantages of Integrated Systems

In traditional analysis systems large volumes of biological or organic reagents are stored in tubes and mixed in beakers. Stirring and heating are needed for chemical reactions or biomolecule amplification steps. These are done on top of hotplates. Transfer of reaction products from one step to another is done via tubes and beakers. Different separation methods, detection and analysis are employed using bench top equipment. These systems are big and expensive. They are very labor intensive. Furthermore the

analysis time is very long, as long as a day. Depiction of a traditional analysis system is shown in Fig. 24. However if all this bench top equipment can be shrunk and put on a chip, everything can be totally automated. Then the analysis time will reduce to minutes and the required volume of chemical and organic reagents reduced to micro liters. Batch fabrication will make these devices cheap so that they can be disposable and cross contamination will not be an issue. Furthermore these systems will be more accurate because everything, transportation, mixing, reactions, separation and detection are made on the same chip. There is no source of external contamination and detectors in microscale have better resolution.

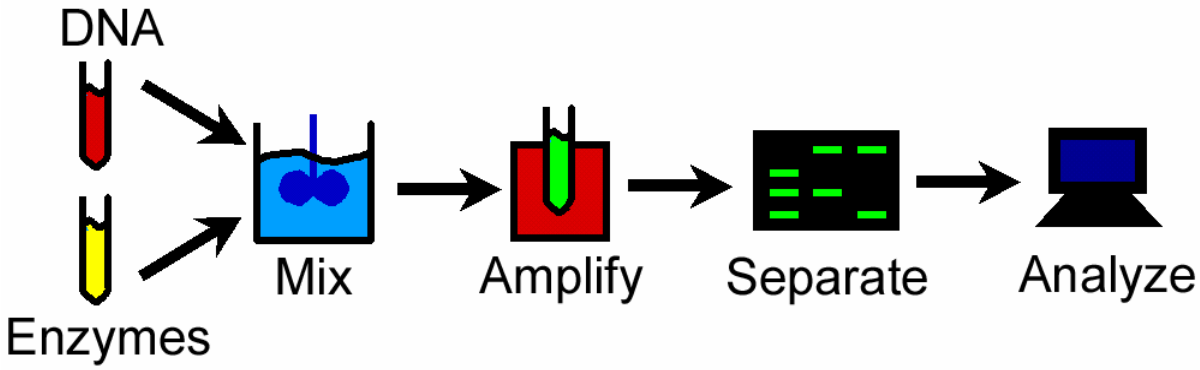

Fig. 1.24. Traditional bench top analysis system.

1.6 Realization Of An Integrated System

The methodology used in this work to achieve an integrated analysis system is to start with a simple, large-scale integratable microfluidic device (pump and valve). A microfluidic system can be realized after that by fabricating tens, hundreds of these devices together (large scale integration) on a chip with a specific application in mind. Once this is realized, an integrated microfluidic system can be integrated with integrated circuits either in monolithic or hybrid fashion to develop the final micro total analysis system that can perform many complex tasks like analyzing DNA, proteins, cells, water quality or monitoring patient's health wirelessly. This is depicted in Fig. 25. This

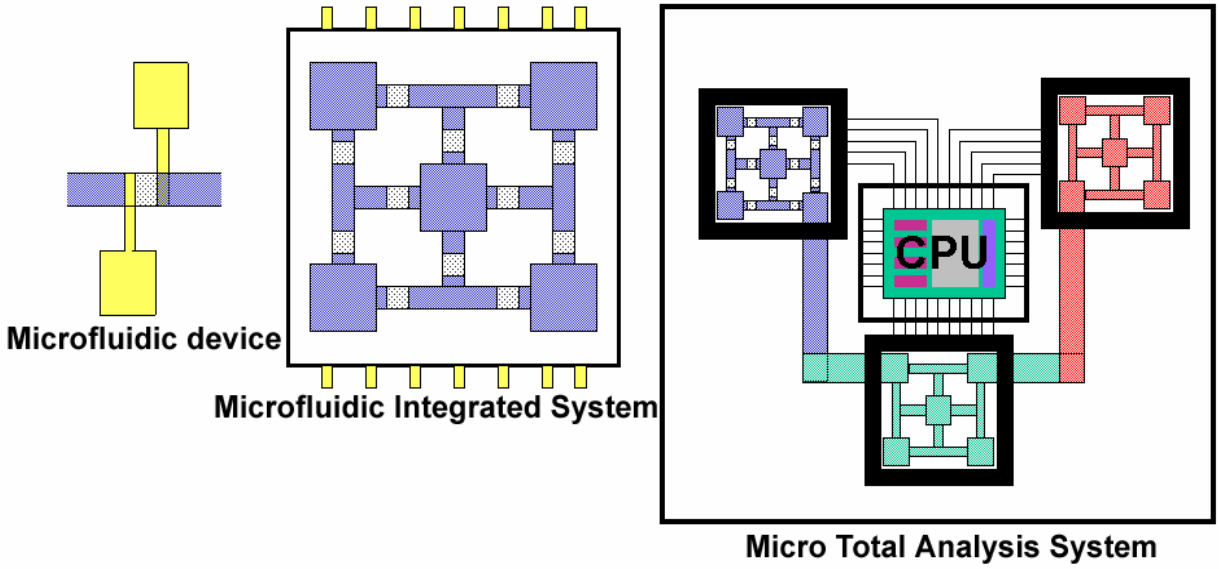

Fig. 1.25. Proposed methodology to achieve integrated systems.

methodology is very similar to the one used for the integrated electronic circuits. The revolution in the electronic industry was achieved after years of intense labor for the development of a single device, a semiconductor transistor. Once a good, reliable and integratable transistor was achieved, their large-scale integration resulted in today's highly sophisticated integrated electronic circuits. That is why a similar methodology is adapted in this work for the integrated microfluidic systems.

Proposed large-scale integratable microfluidic devices are a new kind of electro-osmotic pump and a thermally responsive polymer valve to be used in an integrated microfluidic system. This pump addresses all above-mentioned disadvantages about electro-osmotic pumps by using several approaches. The first approach is using a micromachined porous polymer and employing an AC current drive for bubble free electro-osmotic flow, thus suppressing bubble generation. In this approach electrodes are inside the microchannel on both sides of the porous plug. Using vertical electrodes results in

higher flow rates. A second approach is to use DC drive without any bubble generation problem with a liquid-bridge concept. The final approach is to use AC drive with field effect flow rectification using zeta potential modification (flowFET). With the pumps employing porous polymers, liquid-air interface can be moved back and forth precisely by applying an electrical signal. It has a simple fabrication process, no moving parts and high integration density. An AC driven flowFET device has been demonstrated to be effective and large scale integratable. Similarly, a thermally responsive polymer valve also has a simple fabrication process, no moving parts and high integration density. It is formed by the integration of a surface micromachined thermally responsive polymer with micromachined parylene channels with an embedded heater.

As a conclusion, in order to achieve an integrated microfluidic system, research contributions have been made in the following areas:

- Development of a porous plug electro-osmotic pump with no moving parts, simple fabrication process and high control over the liquid movement therefore suitable to build a totally integrated microfluidic system.
- Development of different drive mechanisms for electro-osmotic pumps: DC drive with liquid bridge and AC drive with field effect flow rectification using zeta potential modification.
- Development of an inline microvalve for aqueous liquids that uses photo-patternable thermally responsive polymers with embedded microheaters, with no mechanical part and very simple fabrication method to be used in the same integrated system.

An example of an envisioned integrated system using these devices is shown in Fig. 26.

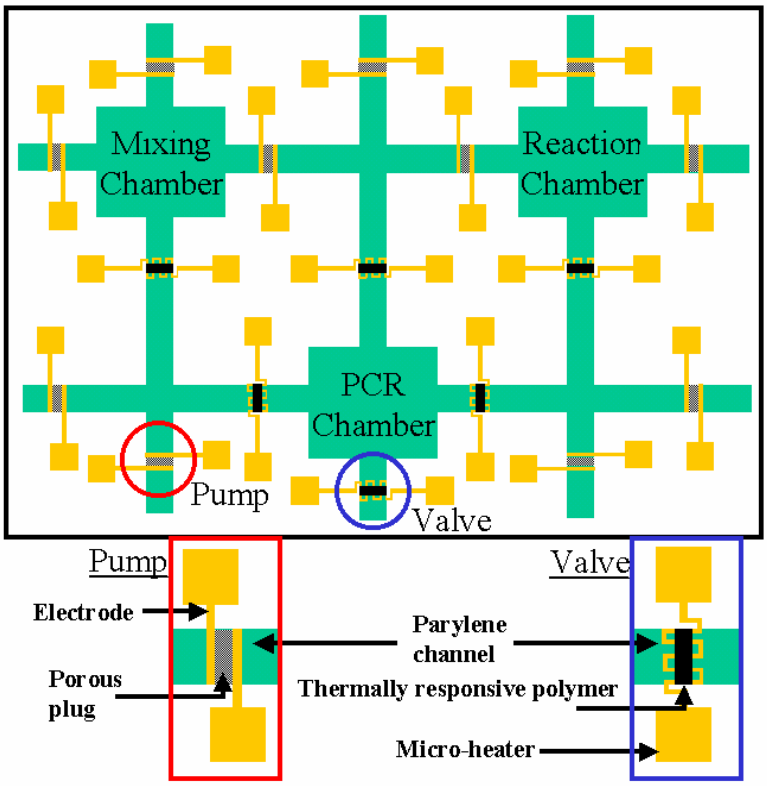

Fig. 1.26. An example of an integrated microfluidic system employing porous plug electro-osmotic pumps and thermally responsive polymer valves.

1.7 Report Organization

In this section, a brief overview of current micropumps, valves and analysis systems has been made. It has been pointed out that to realize an integrated microfluidic system, pumps and valves must be easy to fabricate, must have no moving parts and must be easy to integrate. That is why electro-osmotic pumps and thermally responsive polymer valves have been chosen to be building blocks of integrated microfluidic systems. In section 2, concepts of double layers and electro-osmotic flow are explained. Charge and potential distribution in the double layer and double layer thickness calculation are shown. In a capillary microchannel, equations for electro-osmotic and pressure driven flows are derived. It is shown that scaling down the channel radius reduces pressure driven flow but does not affect the electro-osmotic flow until the

channel radius become comparable to the double layer thickness and the double layers collapse. This explains why using porous polymer plug with submicron pore radius is advantageous for the electro-osmotic flow but not for the pressure driven flow. Also in this section, a brief modeling of flow through porous structures is shown. In section 3, electrochemistry of two-electrode and an electrolyte system is discussed. It is shown that if the amount of injected charges are small, this only charges and discharges double layer capacitance through the solution resistance. Therefore, voltage-current characteristic for this regime is linear and zero-averaged current signal applied to prevent bubble generation generates zero-averaged voltage response resulting in net zero movement. However if the amount of the injected charges is large, faradaic rectification happens. The current-voltage response becomes highly non-linear resulting in a voltage response with net average however with repeatability and reliability issues. Thus, section 3 explains how it is possible to drive net electro-osmotic flow with low frequency net zero averaged current signal and safety and linearity of high frequency signals. Section 4 talks about the fabrication and test results of a new surface micromachined porous plug electro-osmotic pump. That section shows the surface micromachining of a porous polymer. Then it gives the fabrication steps of the porous plug electro-osmotic pump with planar and vertical electrodes with their test results. Section 5 introduces two new approaches to drive electro-osmotic pumps. First approach uses a liquid-bridge. Narrow porous polymer branches with the liquid inside them connect external electrodes in electrode reservoirs to the liquid in the main channel. This way DC voltage applied to the electrodes does not cause bubble generation problems but drives an electro-osmotic flow in the main channel. Second approach introduced in section 5 is the electro-osmotic flow rectification with zeta potential modification. With this approach an AC signal in the kHz frequency range can be applied and net flow can be achieved by modulating the zeta potential of the surfaces that generate electro-osmotic flow by applying an AC signal spontaneously to an insulated gate electrode. In Section 6, thermally responsive polymer valve is introduced. Formulation of a photoresist like thermally responsive polymer is given. This is followed by its thin film formation and patterning. Fabrication of the thermally responsive polymer valve by integration of the patterned polymer film into a parylene channel with an embedded heater is shown and test results are presented. Also

this section presents results of in-situ polymerization of the same thermally responsive polymer inside glass capillaries and glass chips to form valves. Finally, thermally responsive polymer valves with adjustable critical solution temperatures from 35-74 ^{o}C are introduced. They have been in-situ polymerized inside glass capillaries and chips to form valves. The report ends with a conclusion and future work section and bibliography.

SECTION 2

DOUBLE LAYER CONCEPT AND ELECTRO-OSMOTIC FLOW

2.1 Introduction

Most solid surfaces acquire a finite charge density at the interface upon contact with an aqueous liquid. The charged surface attracts counter-ions and repels co-ions in the solution forming a double layer of ions, consisting of a compact immobile layer and a mobile diffuse layer in the liquid. If an electric field is applied parallel to the interface, mobile charges in the diffuse layer are moved, dragging the liquid with them while charges in the compact layer remain immobile. This movement of liquid as a result of the electric field is called the electro-osmotic flow (EOF).

In this section, ion concentration and potential profile across double layer is modeled using Boltzmann distribution depending on the zeta potential of the interface and ion concentration of the solution. Double layer capacitance therefore double layer thickness is explained using three different models: Helmholtz, Gouy-Chapman and Gouy-Chapman-Stern. Electro-osmotic flow is calculated using the charge and potential profile across the double layer assuming a constant horizontal electric field gradient. Affect of capillary radius scaling is discussed on pressure-driven and electro-osmotic flow. Finally flow through porous structures is modeled.

2.2 Double Layer Concept And Interface Charge and Potential Distribution

Most solid surfaces, metal, polymer and glass, acquire a finite charge density at the interface upon contact with an aqueous liquid [Hun81]. Main cause of this is the ionization of surface functional groups on the solid surface. For the case of glass and silica interface with water, surface is charged due to the deprotonation of surface silanol

groups [Che02]. The charged surface attracts counter-ions and repels co-ions in the liquid solution. Deprotonation usually leaves the solid surface negatively charged. Then the surface attracts positive ions in the solution. As a result of the electro-neutrality of the whole system, a double layer of ions is formed at

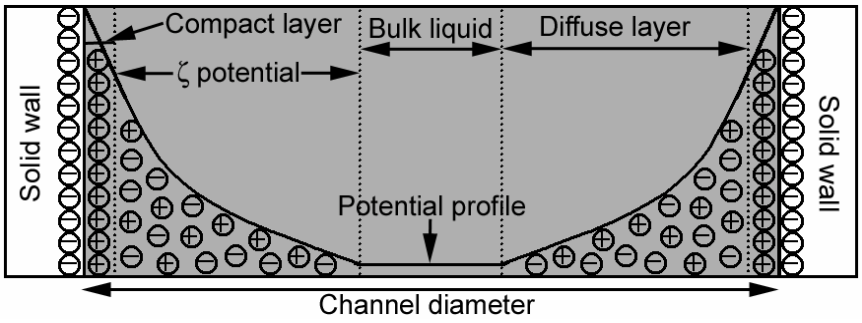

Fig. 2.1. Depiction of compact and diffuse layer concepts and potential profile between the walls of a channel and an aqueous liquid. Dimensions are not to scale.

the interface between the solid and liquid. Double layer composition is shown in Fig. 1. The first layer is the compact layer, which is very thin, in the order of an ion radius thickness, usually around 5 A°. It is also called inner Helmholtz or Stern layer. These are the positive ions attracted strongly to the solid with electrostatic forces caused by the negative charges on the solid side. The locus of the electrical centers of the specifically adsorbed ions is called the inner Helmholtz plane (IHP) [Bar01]. The compact layer is fixed. It does not move, expand or shrink. The diffuse layer extends from the compact layer towards the bulk liquid. The imaginary plane between the compact and diffuse layer is called outer Helmholtz plane (OHP). Potential drop across the diffusion layer is called the zeta potential, ζ. As the distance to the solid surface increases electrostatic force starts to diminish and ions arrange themselves loosely, which can be approximated as a Boltzmann distribution. Then the charge distribution of ions at the diffuse layer can be formulated as:

$$n_i = \overline{n}_i e^{ez_i\psi / kT} \tag{1}$$

where $\bar{n}_i$ is the average number of ith type of ion per volume in the bulk solution, e charge of one electron, z_i the valence number of ith type of ion (valence of ions when one kind of salt dissociates into two equal and oppositely charged ions), ψ, potential of ions with respect to the bulk of the liquid, k the Boltzmann constant, T is the absolute temperature. Assuming a simple electrolyte that ionizes into two equally charged ions of valence z, like DI water, then the net charge per unit volume, ρ, is given by

$$\rho = \bar{n}ez(e^{ez\psi/kT} - e^{-ez\psi/kT}) = -2\bar{n}ez\sinh(ez\psi/kT) \tag{2}$$

The charge density and potential is related with the one-dimensional Poisson equation.

$$\frac{d^2\psi}{dy^2} = -\frac{\rho}{\varepsilon\varepsilon_0} \tag{3}$$

This partial differential equation can be solved by replacing ρ with (2). A solution to this can be found in [Yan98,Yan03]. However some approximation can be done to get simpler solutions. For small $e\psi/kT$, $\sinh(e\psi/kT) \approx e\psi/kT$. Solution using this approximation is in good agreement with that from the exact solution up to $\psi=50mv$ with 1:1 electrolyte [6]. Then assuming a cylindrical channel, and using cylindrical coordinates, the Poisson-Boltzmann equation (3) becomes,

$$\frac{1}{r}\frac{d}{dr}\left(r\frac{d\psi}{dr}\right) = \kappa^2\psi \tag{4}$$

where $\kappa = (2\bar{n}e^2z^2/\varepsilon\varepsilon_0 kT)^{1/2}$ is the reciprocal of the double-layer thickness. Then the solution of (4) for a cylindrical channel of radius a is

$$\psi = \psi_0\frac{I_0(\kappa r)}{I_0(\kappa a)} \tag{5}$$

where ψ_0 is the potential at $r=a$, which is basically ζ potential of the channel wall-solution interface and I_0 is the zero-order modified Bessel function of the first kind. Therefore (5) is good for systems of ζ potentials up to 50 mv [6], , which is the case for the parylene and most of the other polymers. Then the net charge density is given by

$$\rho(r) = -\varepsilon\varepsilon_0\kappa^2\psi = -\varepsilon\varepsilon_0\kappa^2\zeta\frac{I_0(\kappa r)}{I_0(\kappa a)} \tag{6}$$

Potential profiles inside a channel of radius a=2, 1, 0.5, 0.25 and 0.15 μm were plotted in Fig. 2. Here ζ potential is assumed to be 50 mv. Liquid is assumed to be DI water with ion concentration of 7.5 μM corresponding to $\bar{n}$ =4.5x10^{21} m^{-3}. Its dielectric constant is 80. Then the double layer thickness becomes 113 nm. Calculation of this is shown in the next section. From Fig. 2, it can be seen that the effect of the potential at the interface extends about 10 times double layer thickness towards the center of the channel. As channel radius is scaled down, double-layers on both sides of the channel walls collapse. In this example this happens around a=0.75 μm. Then plug like profile starts to look parabolic and the amount of net charge gathered in the double layers drops. As a result this reduces the electro-osmotic flow efficiency.

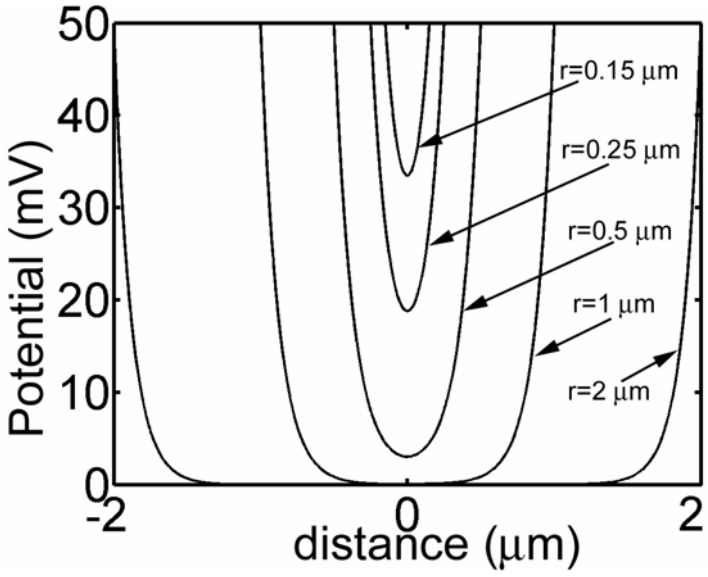

Fig. 2.2. Potential profile inside a cylindrical channel with different radiuses assuming DI water of 7.5 μM ion concentration and ζ potential of 50 mv.

2.3 Double Layer Capacitance

Three different models of double layer structures and their capacitance expressions are given starting with the simplest.

2.3.1 The Helmholtz model

This model assumes two sheets of charge, one at the metal electrode surface and the other in solution as counter-charge, having opposite polarity and separated by a distance. This actually depicts a parallel-plate capacitor, whose value is:

$$C_d = \frac{\varepsilon\varepsilon_0}{d} \tag{7}$$

where ε is the dielectric constant of the medium, ε_0 the permittivity of free space and d distance between plates. Here d can be assumed to be the double layer thickness. This double layer thickness, or Debye length can be calculated as following. However, this model assumes a constant capacitance value. In reality it changes with voltage and electrolyte concentration [Bar01].

2.3.1.1 Double layer thickness calculation

As mentioned above Debye length or double layer thickness, λ, can be approximated to be $1/\kappa$ or $(\varepsilon\varepsilon_0 kT / 2\bar{n}e^2z^2)^{1/2}$. According to this approximation, it only depends on $\bar{n}$, number of ions per volume in the solution since the rest are constants. $\bar{n}$ can be derived either from molarity information of the dominant ions or from the electrical conductivity of the liquid with known ions inside. If ion concentration is given in Molarity (M), molarity is the moles of solute per volume of solution in liter [Zum93], then this value can be converted into mol/m^3 by simply multiplying by 1000 giving the value ion concentration, c. Visiting the definition of mole (mol), 1 mole of something is 6.02x10^{23} of that thing, and this specific number is the Avogadro's number. From this, number of ions in the solution can easily be found by multiplying this number with the Avogadro's number, $\bar{n} = 6.02x10^{23}c$. Then this value can be used to calculate the double

layer thickness. Looking at the above example, 7.5 μM ion concentration in DI water means c=7.5x10^{-3} mol/m^3, $\bar{n} = 6.02x10^{23}\, x7.5x10^{-3} = 4.5x10^{21}$ m^{-3}. Then double layer thickness is 113 nm.

Knowing the electrical conductivity and related major ions is also enough to calculate $\bar{n}$. Electrical conductivity can be expressed in terms of the ionic concentrations, c, and molar conductivities, Λ of anions and cations in the solution such as

$$\sigma = \sum \Lambda_+ c_+ + \Lambda_- c_- \tag{8}$$

Here σ has a unit of S/m, Λ Sm^2/mol, c mol/m^3. Molar conductivities, Λ, of different anions and cations can be found in [Lid95]. Some of them are summarized in table 1.

Cations	Λ 10^{-4} Sm^2/mol	Anions	Λ 10^{-4} Sm^2/mol
Ag^+	61.9	HCO_3^-	44.5
H^+	349.65	OH^-	198
K^+	73.48	I^-	76.8
NH_4^+	73.5	F^-	55.4
Na^+	50.08	Cl^-	76.31
$1/3Cr_3^+$	67	$N0_2^-$	71.8
$1/2Fe_2^+$	54	HSO_4^-	52

Table 2.1. Molar conductivities of different anions and cations in water.

Therefore once conductivity of a solution is known and the major ions responsible for this conductivity, ionic concentrations can be calculated [Zen01]. For example if the conductivity of a NaCl solution is 0.01 S/m, then we know that this conductivity is due to Na^+ and Cl^-. So $0.01=(50.1+76.3)x10^{-4}c$. Then $c = 0.17$ mol/m^{-3}, $\bar{n} = 1.02x10^{23}$ and double layer thickness is 24 nm. Also total ion concentration in this solution is 340 μM. In the previous example DI water's ion concentration was assumed to be 7.5 μM. Assuming

that the DI water's ion concentration is only due to its equilibrium with the atmospheric CO_2 then the related ions are H^+ and HCO_3^-. Using equation (8), conductivity of this solution can be found to be $3x10^{-4}$ S/m. These two examples show that as ion concentration increases, conductivity of the solution increases and the double layer thickness decreases.

2.3.2 The Gouy-Chapman Model

This theory proposes a diffuse layer of charge with finite thickness extending into the bulk of the solution. Unlike Helmholtz model, the charge is not confined to an imaginary plane at the surface. The greatest concentration of excess charges would be adjacent to the electrode due to electrostatic forces and this concentration would diminish further away from the electrode as the affect of this force decreases. This theory predicts a diffuse layer capacitance of [Bar01]:

$$C_d = \left(\frac{2z^2 e^2 \varepsilon\varepsilon_0 \bar{n}}{kT} \right)^{1/2} \cosh\left(\frac{ze\zeta}{2kT}\right) \tag{9}$$

where z is the charge magnitude of the ions in a z:z electrolyte, e the charge of an electron, $\bar{n}$ is the number concentration of ion in the bulk, ζ potential drop across diffuse layer, k Boltzmann constant, T absolute temperature. Assuming at room temperature, and z:z electrolyte, equation (9) becomes:

$$C_d = 228z\sqrt{c}\cosh(19.5z\zeta) \text{ in } \mu F/cm^2 \tag{10}$$

where ζ is in volts, c in mol/cm^3, and z is an integer.

When this capacitance is plotted against applied voltage a $V_{\text{-shaped}}$ waveform is obtained. However the actual system shows a constant capacitance at much higher voltages. Furthermore at high electrolyte concentrations the V-shape disappears.

2.3.3 The Gouy-Chapman-Stern Model

In Gouy-Chapman model charges are point charges and can approach the surface arbitrarily. However this is not realistic. The ions have a finite size and cannot approach closer than ion radius. More realistic model includes two layers. A compact layer where the charges in the solution are tightly compressed against the boundary at x_2, resembling Helmholtz model and a diffuse layer where charges starting at x_2 with potential ϕ_2 resembling Gouy-Chapman model. This is shown in Fig. 3. The plane at x_2 is called the outer Helmholtz plane (OHP). Then the total double layer capacitance C_d is the series sum of C_H, compact layer capacitance and C_D, diffuse layer capacitance.

$$\frac{1}{C_d} = \frac{1}{C_H} + \frac{1}{C_D} \tag{11}$$

$$\frac{1}{C_d} = \frac{x_2}{\varepsilon\varepsilon_0} + \frac{1}{\left(2\varepsilon\varepsilon_0 z^2 e^2 n^0 / kT\right)^{1/2} \cosh(ze\phi_2 / 2kT)} \tag{12}$$

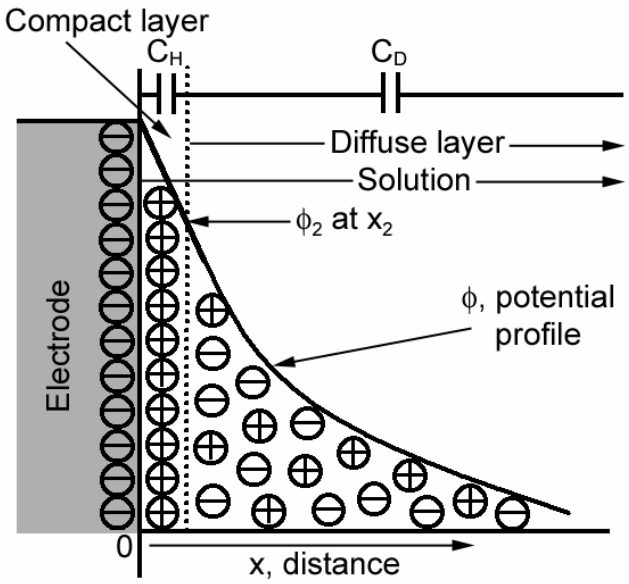

Fig. 2.3. Depiction of compact and diffuse layer concepts and potential profile at the electrode- solution interface.

The result is shown in Fig. 4 and this is in good agreement with the behavior of a real system even though more refinement in the model has to be done to get exact

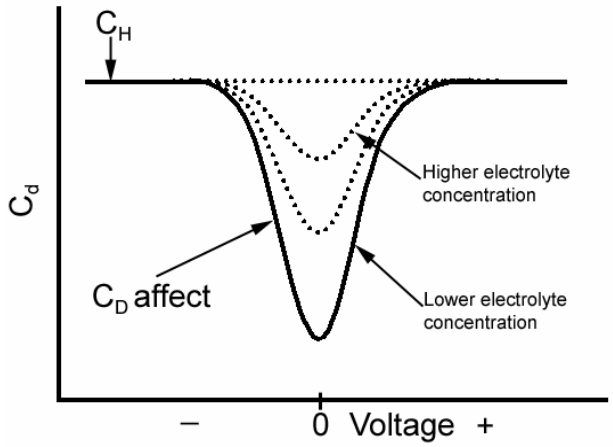

Fig. 2.4. Qualitative behavior of C_d derived with Gouy-Chapman-Stern model over a wide potential range and electrolyte concentration.

matching like potential dependence of compact layer capacitance. Since compact layer thickness is around 5 A°, its capacitance is very large and can be neglected most of the time. So in order to approximate double layer thickness and double layer capacitance, the Gouy-Chapman model is appropriate.

2.4 Electro-osmotic Flow

As explained in the previous section, a double layer forms between channel walls and aqueous liquids. This produces a layer of charges in the compact and diffuse layer. If a tangential electric field is applied, mobile charges in the diffuse layer can be moved by

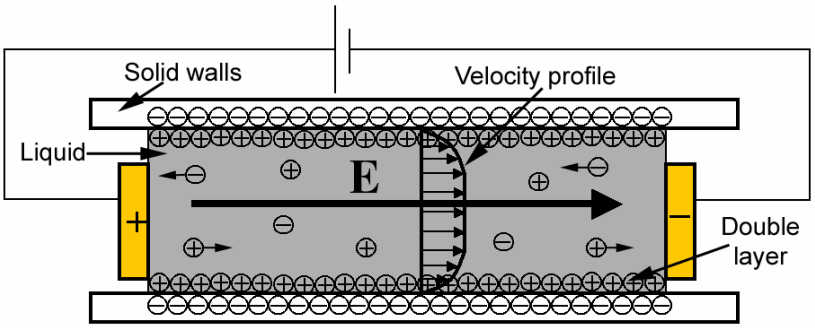

Fig. 2.5. Depiction of electro-osmotic flow: double layer formation, dragging of liquid through surface charges with a tangential electric filed and resulting velocity profile.

this electric field dragging the liquid with them while charges in the compact layer remain immobile. Therefore, as previously mentioned, the outer Helmholtz plane turns out to be a slip surface where the fluid has zero velocity, however at its extent towards the channel center, the fluid assumes a slip velocity, v_0. This liquid movement as a result of the electric field dragging the liquid through the excess charges at the interface between the channel walls and the liquid is called the electro-kinetic or electro-osmotic flow (EOF). The idea is depicted in Fig. 5. If channel radius is assumed to be much larger than the double layer thickness then the electro-osmotic flow is a plug flow with a constant velocity of v_{eo} with a constant tangential electric field unlike the parabolic profile with a pressure driven flow, which disperses the reagents being transported.

Again assuming a cylindrical channel and cylindrical coordinates, in the presence of an applied potential gradient and pressure gradient, liquid motion equation is

$$\frac{d^2v}{dr^2}+\frac{1}{r}\frac{dv}{dr}=-\frac{P_z}{\eta}-\frac{E_z}{\eta}\rho(r) \tag{13}$$

$$v(a)=0,\ \frac{dv}{dr}\Big|_{r=0}=0,\ \text{boundary conditions}$$

where $v(r)$ is the velocity at distant r from the center of the channel, a the radius of the channel, P_z pressure gradient across the channel, E_z is the electric field magnitude, $\rho(r)$ is the net charge density from (6) and η is the liquid viscosity. Boundary conditions say that velocity is zero at the wall surface and velocity gradient is zero at the center of the channel. Then the solution of (13) is a sum of a Poisseuille flow term due to pressure gradient and an electrokinetic term [Ric65].

$$v(r)=\frac{P_z}{4\eta}(a^2-r^2)-\frac{\varepsilon\varepsilon_0\zeta E_z}{\eta}[1-\frac{I_0(\kappa r)}{I_0(\kappa a)}] \tag{14}$$

The overall velocity of the liquid is the superimposition of pressure driven and electro-osmotic flow terms. If the electrokinetic term is investigated separately then electro-osmotic velocity is

$$v_{eo}(r) = -\frac{\varepsilon\varepsilon_0\zeta E_z}{\eta}[1-\frac{I_0(\kappa r)}{I_0(\kappa a)}] \tag{15}$$

For channel dimensions much larger than double layer thickness, around 10 times larger, $a\kappa>>1$, $I_0(\kappa r)/I_0(\kappa a)$ becomes negligible. Then electro-osmotic slip velocity equation reduces to classical Helmholtz-Smoluchowski equation

$$v_{eo}(r) = -\frac{\varepsilon\varepsilon_0\zeta E_z}{\eta} \tag{16}$$

According to equation (16) electro-osmotic velocity is the same for all r values, resulting in a perfect plug flow. However this is only true for channel dimensions much larger than double layer thickness.

Volumetric flow rate can be found by integrating equation (14) for $v(r)$ over the channel cross-section. Then the volume flow rate is

$$q = 2\pi\int_0^a v(r)rdr = \frac{\pi P_z a^4}{8\eta} - \frac{\pi\varepsilon\varepsilon_0\zeta E_z a^2}{\eta}(1-\frac{2I_1(\kappa a)}{\kappa a I_0(\kappa a)}) \tag{17}$$

where I_1 is the first-order modified Bessel function. In this equation, it is important to notice that pressure driven volume flow due to pressure gradient is proportional to a^4, whereas electro-osmotic volume flow is only proportional to a^2, cross sectional area. That is why scaling down is advantageous for electro-osmotic flow. This can be seen in Fig. 6. Again assuming DI water with ion concentration of 7.5 μM, viscosity of 10^{-3} Pa.s, $\zeta=50$ *mv*, it is clear that for channel radius values greater than 1 μm, pressure driven flow dominates over electro-osmotic flow. However for channel dimensions less than 1 μm,

electro-osmotic flow starts to dominate. By equating equation (17) to zero, the maximum pressure that electro-osmotic flow can generate or in other words the maximum backpressure that it can withstand can be found. This is shown in Fig. 7 for different applied voltages therefore different electric field magnitudes assuming same conditions

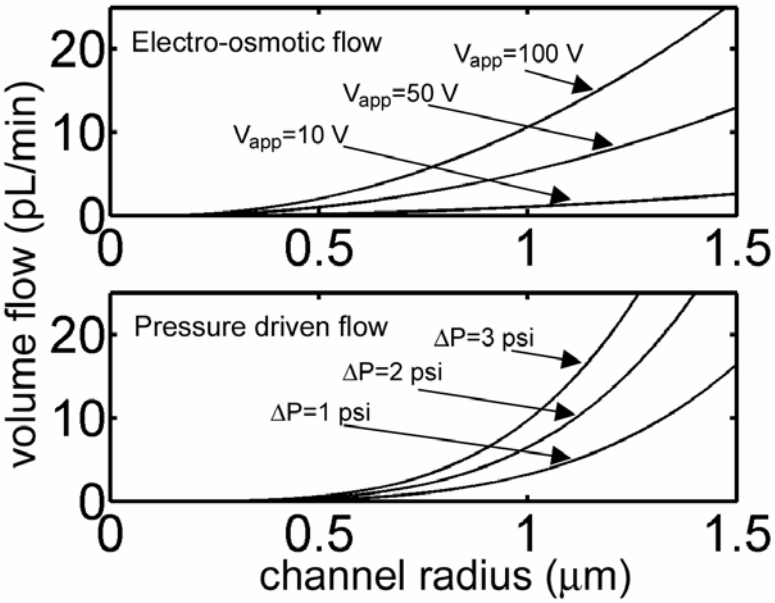

Fig. 2.6. Volume flow rates for electro-osmotic flow at different electric field magnitudes and pressure driven flow at different pressure difference across 50-μm long cylindrical channel as the channel radius is scaled down.

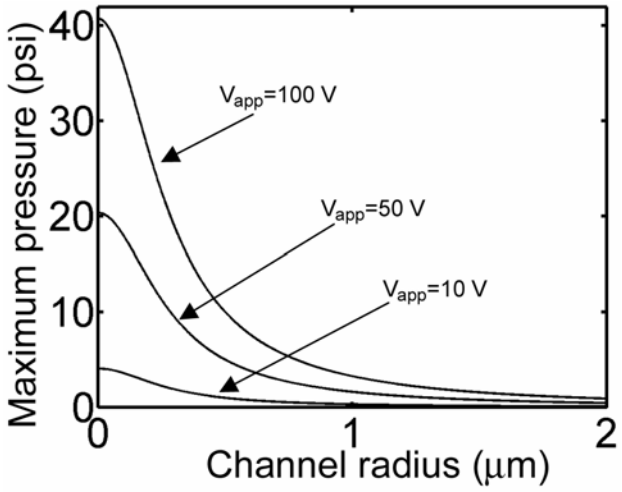

Fig. 2.7. Maximum pressures that can be generated with electro-osmotic flow with the same assumptions used in Fig. 6 with different electric field magnitudes as channel radius decreases.

as in Fig. 6 with a channel of 50-μm length. It can be seen that as we scale down the channel dimension below 1 μm, the pressure that can be generated (back pressure) increases. That is the motivation behind scaling down channels and using porous structures with pore sizes less than 1 μm: to remove pressure driven flow and eliminate back-pressure and but allow electro-osmotic flow therefore have a high control over liquid flow with the electro-osmotic flow since it does not have any moving parts and it is controlled by voltages.

However, after some point, scaling down does not work favorably for the EOF. If the channel radius is kept decreasing and if it becomes comparable to the double layer thickness, as explained in the double layer section, double layers collapse. This results in the reduction of net charges in the double layer therefore reduction of the electro-osmotic flow mobility. Electro-osmotic flow mobility can be defined as follows:

$$Q_{EOF} = Mobility_{EOF} \cdot A \cdot E \tag{18}$$

$$Mobility_{EOF} = -\frac{\varepsilon\varepsilon_0\zeta}{\eta}\left[1 - \frac{2I_1(\kappa r)}{\kappa a I_0(\kappa a)}\right]$$

where A is the cross-sectional area of the channel and E is the electric field magnitude. If this mobility is plotted for decreasing channel radius while keeping the liquid same, that is keeping the double layer thickness the same, there will be a drop in the EOF mobility if the channel radius becomes comparable to double layer thickness ($a < 10\lambda$). This is shown in Fig. 8. For this case, DI water is used. Its double layer thickness is around 0.1 μm. As can be seen from the graph, below channel radius of 1 μm, there is a sharp decrease in EOF mobility. Above channel radius of 2 μm, mobility assumes a constant value, which is given by the classical Helmholtz-Smoluchowski equation ($\varepsilon\varepsilon_0\zeta/\eta$). Therefore the difference in the EOF mobility can be very high between a nanochannel and a micro channel. From Fig. 8, EOF mobility of a channel with a radius of 5 μm is 5.5 times the EOF mobility of a nanochannel of a radius of 150 nm. Therefore, there is a

range for channel dimensions where pressure driven flow is eliminated and electro-osmotic flow mobility is high. This range can be somewhere between 1 μm and 100 nm

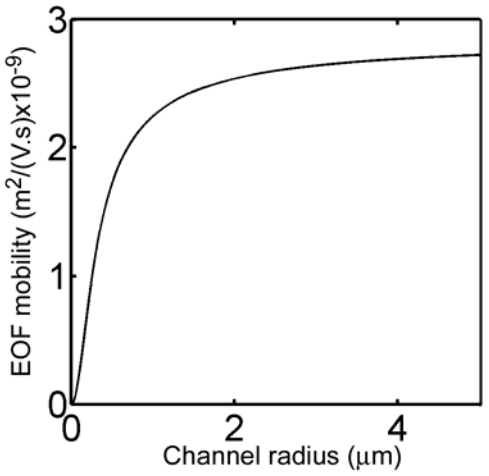

Fig. 2.8. EOF mobility decrease with decreasing channel dimension (with channel radius, double layer thickness ratio decreasing).

depending on the double layer thickness. If the liquid's ion concentration is increased, this will decrease the double layer thickness hence sharp decrease in EOF mobility will shift to smaller channel dimensions (submicron values). As will be shown in section 5, in liquid bridge concept, difference in electro-osmotic mobilities between nanochannels of a porous polymer and a micro-channel can be used to generate net hydraulic pumping in the electrical field free regions of a microchannel.

2.5 Modeling Flow Through Porous Medium

A porous structure can be modeled as a packing of parallel cylindrical channels with a radius of a as shown in Fig. 9. To characterize a porous structure two new parameters must be defined, tortuosity, τ and porosity, Ψ. Tortuosity is defined as

$$\tau = \left(\frac{L_e}{L} \right)^2 \tag{19}$$

where L_e is the average length of travel for flow along the pore path and L is the physical length of the porous structure. Porosity is defined as:

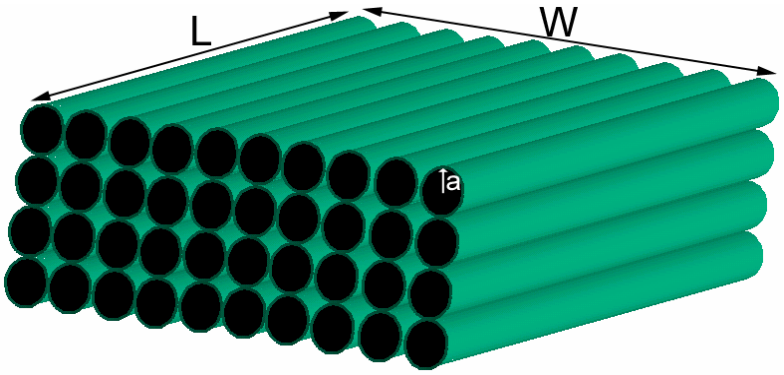

Fig. 2.9. Model of a porous structure as a pack of parallel cylindrical channels of radius *a*.

$$\Psi = \frac{U_e}{U} \tag{20}$$

where U_e is the void volume and U is the total volume of the porous structure. Then the effective cross-sectional area of the porous structure can be estimated as:

$$A_e = \frac{\Psi WL}{\sqrt{\tau}} = \frac{\Psi A}{\sqrt{\tau}} \tag{21}$$

where W is the physical width and A is the physical cross-sectional area of the porous structure. Similar to flow rate equation (17) of a cylindrical channel of radius a, the flow rate of the entire porous structure can be found to be

$$Q = -\frac{\Psi P_z A a^2}{8\eta\tau} - \frac{\Psi \varepsilon\varepsilon_0 \zeta E_z A}{\eta\tau}\left(1 - \frac{2I_1(\kappa a)}{\kappa a I_0(\kappa a)}\right) \tag{22}$$

where P_z is the pressure gradient across the porous structure, which is $\Delta P/L$, where ΔP is the pressure difference upstream and downstream of the porous structure. E_z is the electric field magnitude, which is $\Delta V/L$, where ΔV is the applied potential across the porous structure [Zen01].

2.6 Circuit Model For The Fluid Flow In Microchannels

In fluid dynamics, one of the most basic terms is the Reynold's number. It can be simply defined as the ratio of the fluid's inertial forces to its drag forces. It is unitless and can be expressed as following:

$$\mathrm{Re} = \frac{UL\rho}{\eta} = \text{Reynolds number} \tag{23}$$

where U is the characteristic speed of the fluid, L is the characteristic dimension of the channel, ρ is the density and η is the viscosity of the liquid. The Reynolds number is significant because it determines the flow regime of a fluid, either as a turbulent, laminar or in between. Turbulent flow is the flow where chaotic flow is possible. However in the laminar flow, there is no turbulence, no chaotic liquid movement. The pressure changes linearly with the volume flow rate, similar to Ohm's law. A graph of flow regimes corresponding to its Reynolds numbers is given in Fig. 10. The flow is laminar for Re < 1000. For microchannels used in this work, typical liquid speed is 100 μm/s, and typical dimension is 33 μm. Viscosity of water is 10^{-3} Pa.s and its density 1000 kg/m^3. Then the Reynolds number for this flow is 0.003. This is indeed very low. Therefore the flow is

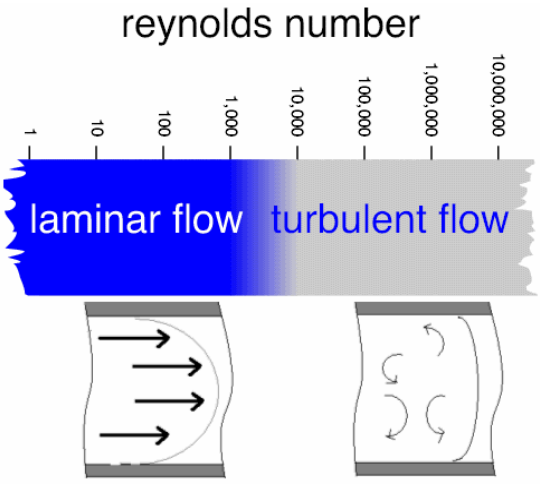

Fig. 2.10. Flow regimes and Reynolds numbers.

definitely laminar. This means that pressure driven liquid flow in this work can be easily modeled using linear elements like resistors.

Since the liquid flow in microchannels is laminar, the pressure in the fluidic system is linear with the flow rate just like voltage is linear with current in electrical circuits. In order to model and solve a linear systems, any other linear system can be used. The electrical domain has all the simulation and modeling tools for analysis of a linear system. So it is advantageous to convert quantities from other systems like fluidic or mechanical systems into electrical system, make calculations and solve the problem in that system and then convert it back to the original system. Conversion from a fluidic system to an electrical system is very simple. Pressure, *P*, simply corresponds to voltage, *V*. Volume flow rate of the liquid, *Q*, corresponds to current, *I*. The microfluidic channel has a hydraulic resistance to liquid flow, R_{hyd}, just like an electrical resistance, R_{el} has a resistance to current flow as expressed in the Ohm's law as following:

$$V=I\cdot R_{el} \text{ (Ohm's law)} \qquad P=Q\cdot R_{hyd} \text{ (Laminar flow)} \qquad (24)$$

Therefore a microfluidic channel can be modeled as a resistor in the circuits model. The value of the hydraulic resistance changes for cylindrical and rectangular channels and channels with porous material. Their values can be found by using equations in Table 3.

	Hydraulic Resistance	**Terms**
Cylindrical	$\frac{8\eta L}{\pi a^4}$	a radius, L length
Rectangular	$12\eta L\left\{H^3W-\frac{192}{\pi^5}H^4\sum_{m=0}^{\infty}(2m+1)^{-5}\tanh[\frac{(2m+1)\pi W}{2H}]\right\}$ or simply $\frac{12\eta L}{H^3(W-0.6H)}$ for $W >> H$	η viscosity, L length, W width, H height.

Porous	$\frac{8\eta L\tau}{a^2\Psi WL}$	a pore radius, τ tortuosity, Ψ porosity.

Table 2.2. Hydraulic resistance formulas for different channel types.

In a similar manner, an electro-osmotic pump can be modeled. As seen at the beginning of this section, the volume flow rate through an electro-osmotic pump has two components, pressure driven and electro-osmotic flow.

$$Q_{total} = Q_{pressure} + Q_{EOF} \tag{25}$$

So the whole device can be modeled as an ideal current source giving a constant electro-osmotic flow and a resistor due to pressure driven flow. This electrical representation is a Norton equivalent circuit representation. Same thing can be represented as an ideal voltage source and a resistor as shown in Fig. 11 corresponding to Thevenin equivalent circuit representation. R_{hyd_EOP} is the hydraulic resistance of the electro-osmotic pump.

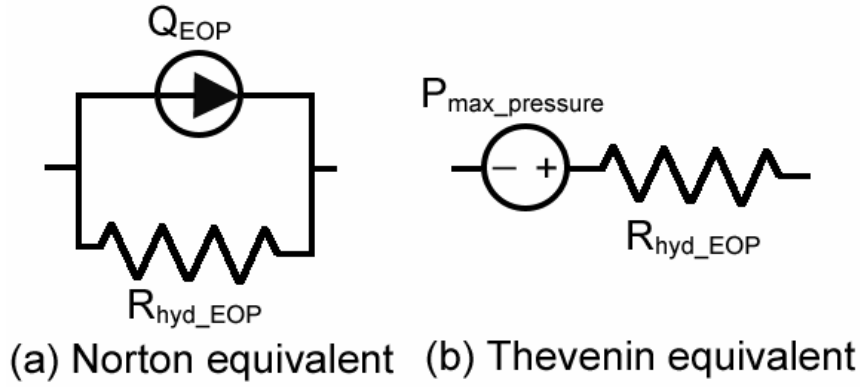

Fig. 2.11. Equivalent circuits of EOP.

The bigger it is, better for the pump because then there would be less back pressure. And that is what exactly a porous plug does as explained previously. Q_{EOP} is the maximum flow that an electro-osmotic pump can generate. It is the measured volume flow rate

when the pump faces zero hydraulic resistance. This can be achieved by having an open, very short microfluidic channel just upstream of the pump. Usually this is the value that is measured. Once this value and pump's hydraulic resistance is known, its P-Q relation can be modeled. $P_{max_pressure}$ is the pressure when there is zero flow. Then there is a simple relation between Q_{EOP} (max. flow) and max. pressure which is:

$$P_{max_pressure} = Q_{EOP} \cdot R_{hyd_EOP} \tag{26}$$

An open channel corresponds to a short-circuit in electrical circuits. Indeed if we take the Norton representation and connect two ends with a wire, the current on that wire would be Q_{EOP}. That corresponds to the maximum flow the pump generates in agreement with the definition before. $P_{max_pressure}$ is the maximum pressure that the pump can generate. This is achieved by closing one end of the channel, thus introducing an infinite hydraulic resistance. This means an open circuit in the equivalent circuit. With the two end's of the Norton equivalent circuit left open circuited, voltage across the hydraulic resistance of the pump is R_{hyd_EOP} x Q_{EOP}, again consistent with equation 26.

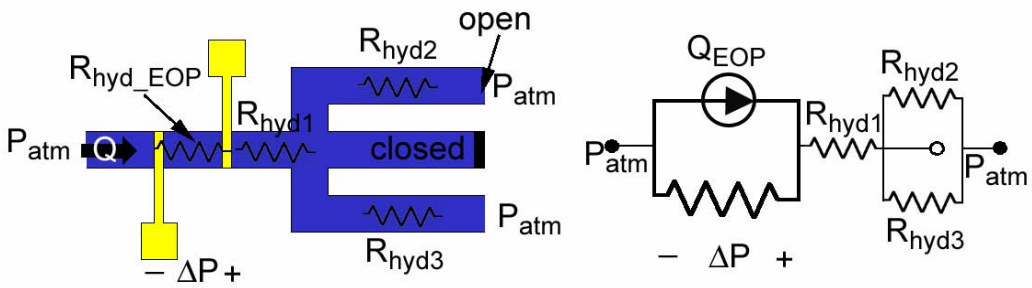

Fig. 2.12. An example of microfluidic system and its equivalent electrical circuit.

The conversion from a microfluidic system to an electrical circuit can be best understood with an example as given in Fig. 12. This figure shows a fluidic system with an electro-osmotic pump and multi microchannels and its equivalent electrical circuit. Then using same methodology, analysis of more complex microfluidic systems with cascaded pumps and channels can be done easily.

2.7 Pressures Generated Due To Droplets in Reservoirs

The gravitational forces in microchannel can be neglected because the mass is very small inside the channel, there is no height difference and the other forces like surface tension dominates over them. However this is not true for the droplets in the reservoirs. The droplets in the reservoirs have big masses generating pressures in the microchannels. That is one of the main reasons why pressure driven flow is not desirable because even a small volume difference in reservoirs can generate big flows in microchannels which can not be controlled. Here a droplet will be modeled as a rectangular prism. If there is a height difference of Δh between reservoirs, then the pressure and the volume flow rate that it causes in a microchannel with hydraulic resistance of R_{hyd} can be found to be:

$$P = \rho \cdot g \cdot \Delta h \qquad Q = = \rho \cdot g \cdot \Delta h / R_{hyd} \tag{27}$$

where ρ is the density of the liquid and g is the gravitational acceleration (9.8 m/s^2). For example, a typical microchannel has dimensions of 20 μm height, 200 μm width and 2 mm length with reservoirs on its both sides. Then this channel has an hydraulic resistance of 1.6×10^{13} $Pa.s/m^3$. A height difference of 5 mm generates a pressure of 49 Pa. This corresponds to a volume flow rate of 184 nL/min (liquid velocity of 750 μm/s). These values are very big in an open channel like this. In order to zero this pressure effect, a voltage value of around 106 volts must be applied across the reservoirs assuming a zeta potential of 20 mV for the channel. However, the effect of pressure due to droplets in reservoirs can be easily eliminated with porous structures since they introduce a very high hydraulic resistance into the channel. That is the motivation for surface micromachining a porous polymer and integrating it into parylene channels in this work as will be shown in section 4.

2.8 Conclusion

In this section, double layer and electro-osmotic flow concepts are discussed. It started with the explanation of the formation of double layers at the interface between aqueous liquids and solid walls. Then charge distribution and potential profile of double layers are given. Effects of channel radius reduction on them are also discussed. This is followed by the definition of the electro-osmotic flow. Flow velocity and volume flow rate in a cylindrical channel are given and shown to have two terms: pressure driven flow and electro-osmotic flow. Pressure driven flow elimination and electro-osmotic flow domination are shown as the channel dimension becomes submicron. It is also pointed out that electro-osmotic flow mobility drops as the channel radius becomes comparable to the double layer thickness as double layers collapse. This is followed by a brief modeling of flow through porous structures. Finally, equivalent electrical model of a fluidic system with microchannels and electro-osmotic pumps is introduced to model and solve the liquid flow in that system.

SECTION 3

ELECTRODE KINETICS AND FARADAIC REACTIONS

3.1 Introduction

Electrochemistry is the study of processes and factors that affect the transport of charges across the interface between an electronic conductor (an electrode) and an ionic conductor (an electrolyte). In electrolyte, the charge transport is achieved by the motion of ions whereas in the electrode it is due to electrons. Typical electrolytes are usually liquid solutions containing ionic species like H^+, Na^+, Cl^- in water or other non-aqueous solvents, but can also be fused salts (molten NaCl-KCl eutectic), ionically conductive polymers (Nafion) and conducting solids (sodium β-alumina). Typical electrodes are solid metals (platinum, gold, palladium), liquid metals (mercury drop electrode), carbon (graphite) and semiconductors. Electrochemical cells are systems composed of generally two electrodes separated by at least one electrolyte phase [Bar01]. The overall chemical reaction in the cell consists of two half-reactions, occurring at the electrodes. Usually, only one of the half-reactions is of interest and the electrode at which this occurs is called the working electrode. The current is passed between this working electrode and a counter (auxiliary) electrode. Then the voltage of the working electrode is measured with respect to a nearby reference electrode, a standardized, stable electrode staying in its own compartment and electrolyte and having a known constant interfacial potential. This way negligible current passes through the reference electrode and its potential stays constant. Some common reference electrodes are normal hydrogen electrode (NHE) and saturated calomel electrode (SCE). This measurement involves only electrode-electrolyte interface of the working electrode, giving information of chemical reactions occurring only on that electrode. That is why three-electrode electrochemical cell is very useful in electrochemistry to learn about the nature of the reaction and to record the potential

across the interface. However if only two electrodes are used, then two electrode-electrolyte interfaces are connected together with the solution resistance. In this case, the voltage-current data cannot give information about individual reactions happening at each electrode. Nevertheless, its voltage-current relationship can be modeled.

In this section, potential-current relationship of electrochemical cells will be discussed. This is done to understand the net zero averaged low frequency AC current drive and high frequency AC voltage drive used for the electro-osmotic pumps which are basically electrochemical cells consisting of two electrodes and an electrolyte that will be explained in the next section. With electrodes inside the microchannels DC voltages or currents cannot be used because these cause electrolysis therefore bubble generation, which blocks the channel and fails the pump. Therefore zero-averaged AC current signals at low frequencies (below 10 Hz) are used to suppress bubble generations in Section 4. As will be explained in this section, the voltage response of the electrochemical cell to this current drive is non-linear. Therefore the voltage response can have a net average value and this can be used to drive liquid in the electro-osmotic pump. Furthermore in Section 6, high frequency (>10 Hz, usually around 1 KHz) symmetric zero averaged voltage signals are used to drive the flow field effect transistor (flowFET). Since in this regime, the electro-chemical cell is linear, this drive does not generate any net flow in the electro-osmotic pump. However, the flow can be rectified with the field effect of the gate electrode as will be explained in that section.

3.2 Faradaic And Non-Faradaic Processes

Two kinds of processes occur at the interface between the electrode and the electrolyte: non-faradaic and faradaic processes [Bar01]. The first process occurring after the current application is the non-faradaic process, a capacitive mechanism, charging of the double layer. If the injected charges are constrained only to charge and discharge of the double layer, then there will not be any chemical reaction and electrode can be used

for biological tissue stimulation safely. Once the injected charges exceeds these limits faradic processes (chemical reactions) will start involving the exchange of electrodes across electrode-electrolyte interface [Rob90]. This process can be assumed to be linear for small current values, but it becomes very non-linear even at small current levels. Therefore the current applied to the electrochemical cell, $I(t)$, will be the sum of faradic ,$I_f(t)$, and non-faradic currents $I_{nf}(t)$ as given by:

$$I(t)=I_f(t)+I_{nf}(t) \tag{1}$$

3.2.1 Non-Faradaic Processes

In non-faradaic processes, external currents can flow (at least temporarily) even though at the electrode-electrolyte interface no charge-transfer reactions occur. This can happen due to processes like adsorption, desorption and changes in the double layer due to applied potential and solution ion concentration change. Therefore charging double layer capacitance is a non-faradaic process and does not cause any charge-transfer reaction. Since this only involves a capacitor and the solution resistance, the system is linear within the charge injection limits. However, even double layer capacitance is not an ideal linear capacitor. The double layer thickness changes as the potential across the double layer changes as explained in the previous section. This makes the double layer capacitance non-linear. It also has a voltage rectification property [Vet67]. In this work, for simplicity this capacitance is assumed to be linear. In practice, the non-faradic impedance is not a simple capacitor. It has a constant phase angle (CPA), which is usually less than 90° [Ric02]. This can be formulated as:

$$Z_{CPA} = K(j\omega)^{-\beta} \tag{2}$$

where K is the magnitude with units of $\Omega \cdot s^{-\beta}$ and β is the deviation from a pure capacitance ($0<\beta<1$). $\beta=1$ means it is a pure capacitor. This empirical relation can be said to represent the impedance of the double layer capacitance in the presence of surface

roughness effects of the electrode. β is related to the degree of the surface roughness. Rougher surfaces give lower β value [McA95].

The amount of charge that can be accommodated by this charging is very small, around 20 μC per real electrode area in cm^2. Real electrode area is different than the geometrical electrode area because of the roughness of the metal surface. For simplicity, it can be assumed that real electrode area is 1.4 times greater than the geometric area assuming platinum electrodes (Surface roughness factor of 1.4) [Ros90]. With the typical electrode dimensions used in this work of 30 and $200x10^{-4}$ cm^2, this corresponds to 1.7 nC. Assuming a 1 second pulse, which is usually used in electro-osmotic pumping with low frequency current drive, then the current magnitude is 1.7 nA. This is much less than current level of around 300 nA used in this work to drive this pump. Therefore the pump is operated beyond this linear region. However if a 1 KHz AC signal is applied, then the safe current limit will be 1.7 μA, which is much bigger than the ones applied to flowFETs. Therefore flowFETs operate in the safe linear region. That is why they cannot generate any net flow without zeta potential modification.

3.2.2 Faradaic Processes

Faradaic processes involve the transfer of charge between the electrode and the electrolyte. Two general types of charge transfer can occur at the electrode. The electrode can either supply (reduction) electrons to or sink (oxidation) from chemical species in the electrolyte. The resulting chemical reaction will have the form:

$$R \rightarrow O + ze^- \text{(Oxidation)} \quad (3)$$

$$O + ze^- \rightarrow R \text{ (Reduction)} \quad (4)$$

where R and O are the reduced and oxidized species, and z is the number of electrons transferred in a single reaction. If the electrode material is reactive it can also play a role in the chemical reaction, typically as:

$$M \rightarrow M^{z+} + ze^{-} \tag{5}$$

where M is the electrode metal. These reactions are called faradaic processes because they are governed by Faraday's Law (the amount of chemical reaction happening is proportional to the electrical current passed). Reactions occurring at the electrodes are heterogeneous reactions because it only happens across the electrode-electrolyte interface unlike homogenous reactions occurring everywhere in the medium at the same rate. Therefore reaction rates at the electrode depend on mass transfer of reactants to the interface and electrode surface. Because of that electrode reactions are described in units of mol/s per unit area:

$$Rate(mols^{-1}cm^{-2}) = \frac{i}{zFA} \tag{6}$$

where i is the current, F is the Faraday constant, z the number of electrons and A the electrode area.

3.3 Nernst Equation

The potential at which the energies of electrons in the electrode and electrolyte donor/acceptor sites are equal is called the standard electrode potential, E^o. At electrode potentials more positive than E^o, oxidation occurs, and at potentials more negative than E^o, reduction occurs. The potential of the electrode is then given by [Bar01]:

$$E = E^o + \frac{RT}{zF} \ln \frac{a_o}{a_R} \tag{7}$$

where a_o and a_R are the chemical activities of the oxidized and reduced species at the electrode surface, R is the gas constant and T is the temperature. Since it is more convenient to work with the aqueous concentration of a chemical species than its chemical activity, the Nernst equation is usually expressed in terms of concentrations.

The activity of a chemical species, x, is related to its concentration, c_x, by an activity constant γ_x, where $a_x = \gamma_x c_x$. Then Nernst equation becomes:

$$E = E^{o'} + \frac{RT}{zF} \ln \frac{C_o}{C_R} \tag{8}$$

where the formal potential $E^{o'}$ is given by:

$$E^{o'} = E^{o} + \frac{RT}{nF} \ln \frac{\gamma_o}{\gamma_R} \tag{9}$$

The formal potential is a convenient formulation for avoiding activities, which is important since activity coefficients are almost always unknown. This potential is an experimentally measured quantity, which will vary from medium to medium and is usually quoted in the literature for several common background electrolytes. In general, the concentration of species at the electrode will depend on the mass transport from the bulk solution. This is a function of concentration, geometry and diffusion constant for each reactant, as covered in the next section.

3.4 Mass transfer

Mass transfer is the movement of materials from one part of a solution to another. A stationary electrode immersed in an unstirred electrolytic solution is given a constant potential. If there is an electroactive substance in the vicinity of the electrode, a heterogeneous charge transfer will occur at the metal/liquid interface. At the same time concentrations at the electrode will start to change, which sets off mass transport to the electrode from the bulk. There are three fundamental sources of this motion: diffusion, migration and convection. Diffusion is the movement of a chemical species resulting from a concentration gradient. Migration is the movement of a charged particle in an electric field, and convection is the result of stirring or hydrodynamic transport. The generalized equation for mass transfer is given by:

$$J_i = -Dgrad(C_i) - \frac{z_i F}{RT} D_i C_i grad(\phi) + C_i \nu \tag{10}$$

where J_i is the flux of species i, D_i is the diffusion coefficient, C_i the concentration, z_i the charge, ϕ is the potential in the solution and ν is the hydrodynamic flow respectively. For simplicity, in this work migration and convection terms will be ignored and only semi-infinite diffusion term will be considered. Then equation 10 turns into Fick's second law:

$$\frac{\partial C_i(x,t)}{\partial t} = D_i \frac{\partial^2 C_i(x,t)}{\partial x^2} \tag{11}$$

3.5 Butler-Volmer Model For Electrode Kinetics

Whenever net charge transfer occurs at an electrode surface, the interface is no longer at equilibrium, and a voltage appears across the electrode. Since the chemical reaction is controlled solely by the rate of this chemical charge transfer process, this is called an activation-controlled process. The resulting current-potential relation is the Butler-Volmer equation []:

$$i_f = FAk^0 \left[C_O(0,t) e^{-\alpha(E-E^{0'})/zV_t} - C_R(0,t) e^{(1-\alpha)(E-E^{0'})/zV_t} \right] \tag{12}$$

where E is the electrode potential, k^0 is the standard rate constant, A is the frequency factor in the rate expression, α is a constant that is about 0.5, V_t is kT/q, which is 26 mV. At equilibrium, the net current is zero. Then the electrode adopts a potential depending on the concentrations of O and R based on Nernst equation. Then from equation (8):

$$E_{eq} = E^{o'} + \frac{RT}{zF} \ln \frac{C_O^*}{C_R^*} \tag{13}$$

where E_{eq} is the equilibrium potential of the electrode, C_O^* and C_R^* are the molar concentrations of *O* and *R* in the bulk solution. Then any potential that is different than E_{eq} applied to the electrodes will create a current. This potential difference is called the overpotential and can be expressed as:

$$\eta = E - E_{eq} \tag{14}$$

Then assuming α=0.5 the current-overpotential can be found to be:

$$i_f = i_0 \left[\frac{C_O(0,t)}{C_O^*} e^{-\eta / 2zV_t} - \frac{C_R(0,t)}{C_R^*} e^{\eta / 2zV_t} \right] \tag{15}$$

where i_0 is the exchange current and its value can be determined for each reaction.

3.6 Equivalent Models For Small And Large Overpotential Changes

As apparent from equation 15 and equation 11 electrochemical systems are non-linear. The linearity can be only realized by applying small signal amplitudes or larger signals at high frequency so that the charges injected into the system would not exceed safe linear region limits. For example if a large amplitude sine perturbation signal is applied, the system cannot be investigated with linear approximation. In this case the measured impedance of the system is a function of the frequency and the amplitude of the sine perturbation signal [Kaz95]. Small signal model is for small electrode overpotential modifications around the equilibrium potential. That is $|\eta| < zV_t$. Assuming a single electron reaction, then this is $|\eta|$<26mV. It will be shown that small signal model can be approximated to be composed of only linear circuits elements, resistors and capacitors. However, for larger signals, the reality is more complex than this. It requires non-linear components and exact solutions for equations (15) and (11). This non-linear affects for larger overpotential changes are also summarized.

3.6.1 Linear Approximation Of The Faradaic Response

For small overpotential changes, η, electrode surface concentrations can be assumed to be the same as the bulk values (no mass transfer). Then for single electron reactions and $\alpha=0.5$ equation (15) becomes:

$$i_f = i_0\left[e^{-\eta/2V_t} - e^{\eta/2V_t}\right] \tag{16}$$

Again for small η values exponential can be approximated as 1+x and the faradaic impedance can be found to be a simple resistance:

$$R_{ct} = \frac{V_t}{i_0} \tag{17}$$

This resistance is called the charge-transfer resistance. In this case, mass transfer is not considered because the concentration change is assumed to be small. Then the overall electrochemical cell can be represented by the equivalent circuit shown in Fig. 1. In this figure C_d is the double layer capacitance and R_l is the solution resistance. However mass

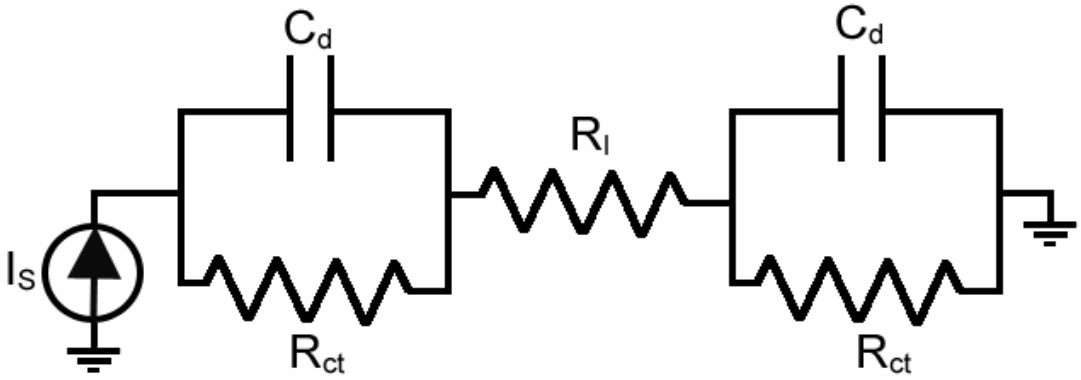

Fig. 3.1. Equivalent electrical circuit of the electrochemical cell for small signals.

transfer affect for small signals can also be added. This will simply be a mass-transfer impedance, which considers only semi-infinite diffusion, usually called Warburg impedance (an RC circuit with a constant phase, usually 45°) in series with the charge-transfer resistance. Since the diffusion of ions from the bulk of the solution to the

interface happens at a finite rate, this gives rise to this impedance to the current flow through the cell, especially at low frequencies. The expression of the Warburg impedance can be given as:

$$Z_W = (1-j)\sigma^{-0.5} \tag{18}$$

where ω is the angular frequency with unit of s^{-1} and σ is the diffusion coefficient with units of $\Omega s^{-0.5}$ [McA95]. Furthermore, for a more accurate model C_d can be replaced with the constant phase angle impedance as explained earlier. This is shown in Fig. 2.

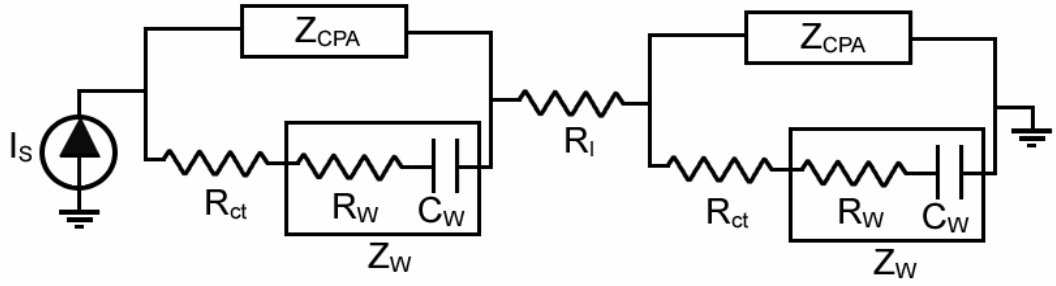

Fig. 3.2. More accurate equivalent electrical circuit of the electrochemical cell for small signals.

3.6.2 Limit Current Of Linearity

Non-linearity of the electrode-electrolyte interface was first studied by Schwan. He saw that even though for small current AC amplitudes this interface is linear and the measured impedance is linear, as the amplitude of the applied AC signal is increased, the interface becomes non-linear, as does the impedance of the electrochemical cell. From his experimental results Schwan derived an empirical limit current of linearity, which was defined as the current at which the cell impedance deviate 10% from its linear value [McA92a]. His empirical results showed that this limit current of linearity varies with frequency according to the following relation:

$$i_L = i_1 \omega^{1-m} \tag{19}$$

where i_1 is a constant, ω is the angular frequency and m is a constant where $0<m<1$. Experimentally it was seen that m varies slowly with frequency over the range of 0.01 Hz to 10 kHz. Measured and calculated current limits of linearity using the above equation for platinum electrodes in 0.01 M KCl solution is shown in Fig. 3. Here m varies from 0.08 to 0.3 over the plotted frequency range [Sim80]. From this figure, at 1 Hz the

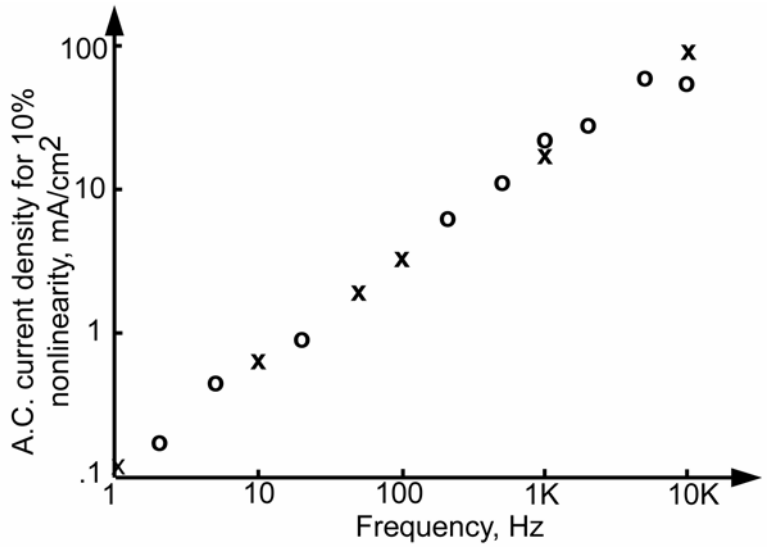

Fig. 3.3. Measured (o) and calculated (x) AC limit current of linearity of platinum electrodes in 0.01 M KCl solution vs. frequency [Sim80].

non-linearity starts at 6 nA current for the typical electrode dimensions used in this work of $30x200x10^{-4}$ cm^2. However this value increases to 6000 nA at 10 kHz. This suggests that at low frequencies nonlinearity is reached very easily. R_{ct} is the main cause of the non-linearity at low frequencies and C_d or Z_{CPA} is the main cause of non-linearity at high frequencies [McA92b]. This nonlinearity at low frequencies will be discussed next.

3.6.3 Model For Nonlinearity At Low Frequencies

Non-linearity of the electrode-electrolyte interface at low frequencies, frequencies that are very close to DC (f < 5 Hz), is dominated by the nonlinearity of the faradaic

current-overpotential relation. Qualitatively, voltage-current nonlinearity can be seen from the DC voltage-current curve of an electrochemical cell. If a DC overvoltage is applied across the interface, the resultant steady state current is measured and if this is repeated for various voltage values, a graph that looks like the one in Fig. 4 can be achieved. Figure 4 shows the steady-state current vs. overpotential of a platinum electrode in saline solution (0.9% NaCl). Assuming this I-V characteristic holds for very low AC signals, if an AC large voltage signal is applied like shown in Fig.4, the resultant current would be like the one also shown in the same figure, very much distorted [Til73]. The nonlinearity is apparent. Also some rectification of the current can be seen. The reverse of this will also be true. If a large AC current signal is applied, resultant potential will also be distorted and rectified.

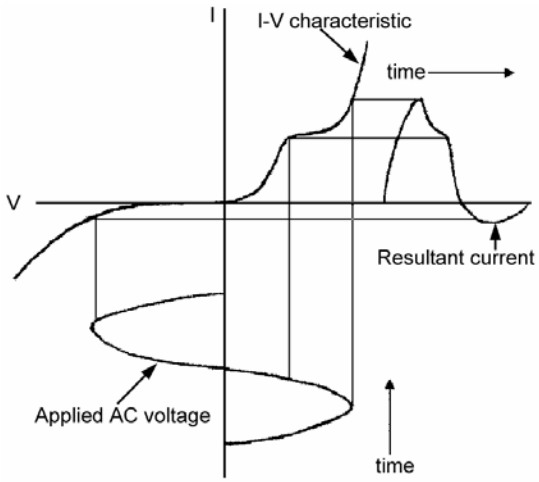

Fig. 3.4. Illustration of the non-linear relationship between voltage and current of an electrochemical cell with large signal magnitudes [Til73].

This non-linearity is apparent in the derivation of the charge-transfer impedance, R_{ct}, which is equal to the overpotential across the interface divided by the faradic current. As explained earlier I_f is related to η by the Butler-Volmer equation (15).

$$R_{ct} = \frac{\eta}{I_f} = \frac{\eta}{I_0}(e^{\frac{(1-\alpha)z\eta}{V_t}} - e^{\frac{-\alpha z\eta}{V_t}})^{-1} \quad (20)$$

In the linear approximation, the exponential was simplified as explained earlier. However for large signal amplitudes, $I_f > 10I_0$, Butler-Volmer equation (15) turns into:

$$I_f / I_0 = e^{\frac{(1-\alpha)z\eta}{V_t}} \quad (21)$$

From this R_{ct} can be derived as:

$$R_{ct} = \frac{V_t}{(1-\alpha)zI_f}\ln(\frac{I_f}{I_0}) \quad (22)$$

For large signal values such that, $I_f > 10I_0$, $\ln(I_f/I_0)$ is almost constant therefore R_{ct} can be assumed to be inversely proportional to I_f [McA92a]. So this nonlinearity can still be modeled with the circuit in Fig. 1. However now R_{ct} will not be a constant but its value will change inversely with the current passing through it. In Fig. 5, non-linear R_{ct} value

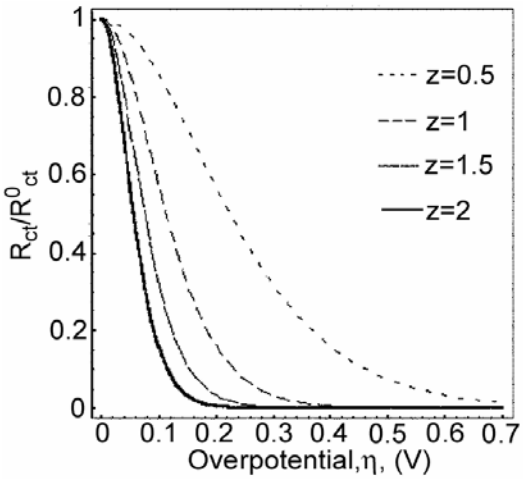

Fig. 3.5. R_{ct} value calculated using equation (20) divided by the small signal R^0_{ct} value in equation (17) vs overpotential across the interface [Ric02].

was calculated using equation (20), divided by the small signal linear resistance value that was given by equation (17) before and plotted against the amplitude of the overpotential voltage across the interface. From this graph, it can be seen that R_{ct} is linear only for very small overpotential values.

3.6.4 Faradaic Rectification

Due to non-linearity of the current-voltage relationship of the electrochemical system, an alternating current signal $i=I\cdot sin\omega t$, causes a shift in the time-average value of the potential, displacing it from the equilibrium value by a small overpotential voltage [Vet67]. This effect is called faradaic rectification. Even though the applied current signal has zero time average, the overpotential will then have a net average. Also applied sinusoidal current can be rectified and a direct current component, I_{dc}, can appear if the applied current density exceeds a critical value. This critical value increases with increasing frequencies. Rectification property of electrode-electrolyte interface has been known since 1900's. In those days, electrolytic rectifiers were used to charge accumulators. They were even used to detect 100 kHz wireless signals [Ged87].

3.6.5 Stronger Non-Linearities At Low Frequencies

Apart from the non-linearity coming from the charge-transfer reactions, if the amplitude of the applied overpotential across the electrode-electrolyte is increased further, there would be stronger non-linearities than predicted by the Butler-Volmer equations. This deviation is shown in Fig. 6a for a platinum electrode in 0.9 % NaCl solution. For this particular case, for $0.1<\eta<0.35$ volts, there is a good agreement between the Butler-Volmer results and the experimental results. However, out of this range, the response is no longer determined by the charge transfer control and the nonlinearity is stronger. This behavior is due to other reactions and/or due to

mass transport control like diffusion. In Fig. 6b, tafel plots of the same experimental results are plotted. (The plots of log(i) vs. η are called tafel plots. They make easier to evaluate electrode kinetics [Bar00].) The peak around ±0.5 volt in the tafel plots, can be attributed to the oxidation of Pt for anodic potentials and to the reduction of dissolved oxygen for cathodic reactions. For voltages less than 0 volt, the reaction is limited by the diffusion of oxygen to the cathode, which causes the abrupt deviation around that voltage, and remains constant till –0.5 volts. At very high voltages, V > +1 oxidation of water and Cl^- ions cause the sharp increase in the current. And at values V < -0.7, the oxidation of water molecules cause that sharp increase [Ric02]. Reactions happening at high overpotentials and related mass transport control are next discussed with alternating current electrolysis.

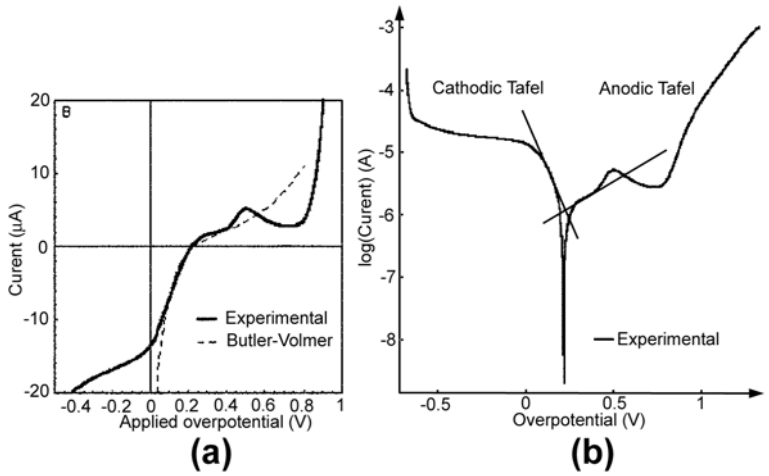

Fig. 3.6. Deviation from Butler-Volmer equation at even larger overpotential (a) and tafel plots of the same experimental results [Ric02].

3.7 Voltage Time Response During Electrolysis With Alternating Currents

If a constant current is applied to the electrode, substance *O* starts to be reduced to products *R* at a constant rate. At the beginning, this reaction is activated controlled as expressed in the Butler-Volmer equation. However as the current is continued to be applied,

the overpotential starts increasing to even higher values. This causes even stronger non-linearities since now the reaction rate is mass transfer controlled. Since for simplicity, convection and migration are neglected, then the reaction rate is controlled by the diffusion of the reacting species from the bulk to the electrode surface. Hence this is now a diffusion-controlled process. Then the potential of the electrode varies according to the Nernst Equation as the ion concentrations change resulting in concentration overpotential. Assuming semi-infinite diffusion on planar electrodes, then the concentration of species changes with a constant current as following:

$$C_O(x,t) = C_O^* - \frac{i}{zFAD}\left\{2\sqrt{\frac{Dt}{\pi}}e^{\frac{-x^2}{4Dt}} - xerfc(\frac{x}{2\sqrt{Dt}})\right\} \tag{23}$$

where C_O^* is the initial concentration, D is the diffusion constant and x is the distance from the electrode surface [Bar01]. Eventually concentration of O drops to zero. The time the concentration drops to zero since the start of the application of the current is called the transition time, τ. Its value is related to the concentration and diffusion coefficients and can be found by equating equation 23 to zero [Ber53] at x=0, at the electrode surface. Then the time constant is:

$$\tau = \frac{C_O^{*2}\pi z^2 F^2 D}{4(I_f / A)^2} \tag{24}$$

The electrode potential up to this transition time can be found using the Nernst equation:

$$E = E^{o'} - \frac{RT}{zF}\ln\frac{D_O}{D_R} + \frac{RT}{zF}\ln(\frac{\sqrt{\tau}-\sqrt{t}}{\sqrt{t}}) \tag{25}$$

If current application goes on after this transition time, the potential of the electrode rises rapidly since the flux of *O* is insufficient to the surface until it finds another reduction process like the reduction of the metal electrode itself. This is depicted in Fig. 7. Sudden voltage jump after the current application is due to the liquid's bulk resistance and is shown in the figure as i_0R_l. Electrochemical analysis method using the application of only one current step to the electrochemical cell and then recording the potential-time response is called the choronopotentiometry.

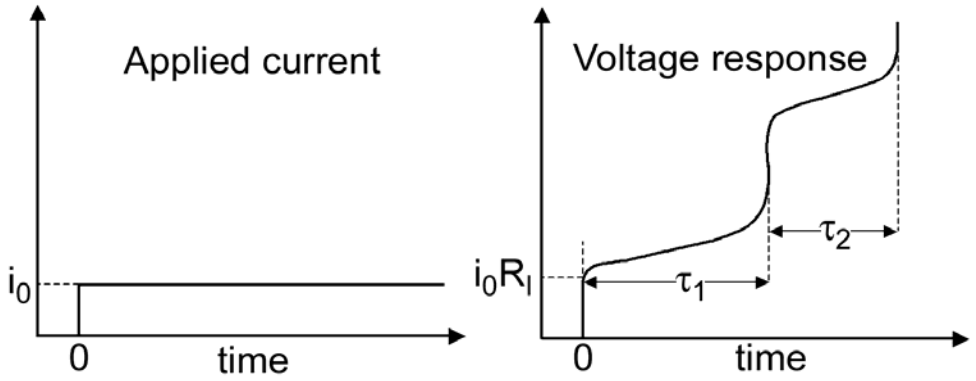

Fig. 3.7. Voltage response of an electrochemical cell to a constant current signal.

If the direction of current is reversed at some stage of the reaction, the re-oxidation of *R,* which had been produced in the previous cathodic stage, will happen, leading to the formation of *O.* This can be done periodically. In electrochemistry, this is used for electrochemical analysis of the reactions and it is called cyclic chronopotentiometry. Then the voltage response would look like the one shown in Fig. 8 depending on t_1, t_2, i_1, i_2 values. In this work, alternating currents with characteristic of

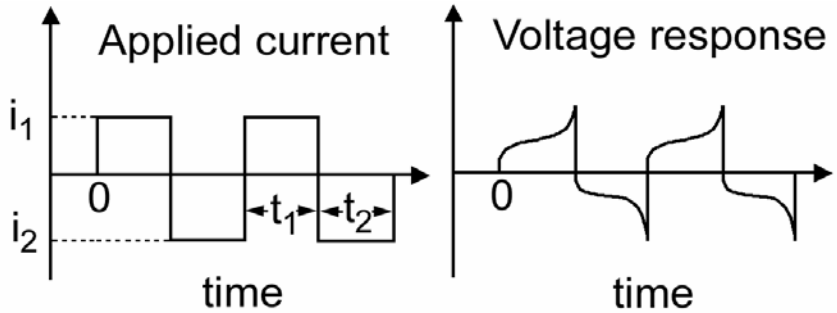

Fig. 3.8. Depiction of voltage response of an electrochemical with periodic current reversal.

$i_1t_1=i_2t_2$ were tried to drive electro-osmotic pumps in Section 4. This current drive is called the biphasic current drive and suppresses the bubble generation significantly.

An experimental result of this drive is shown in Fig. 9. 30% duty cycled, asymmetric square current signal at 2 Hz with pulses of equal charges is applied to the two electrodes of the pump, and the resulting voltage response was recorded. The operated liquid is DI water at equilibrium with the atmospheric carbon dioxide. The voltage response is measured using an interface circuit and oscilloscope (Hewlett Packard, Inc. HP54645A) as shown in Fig. 10. The interface circuit uses operational

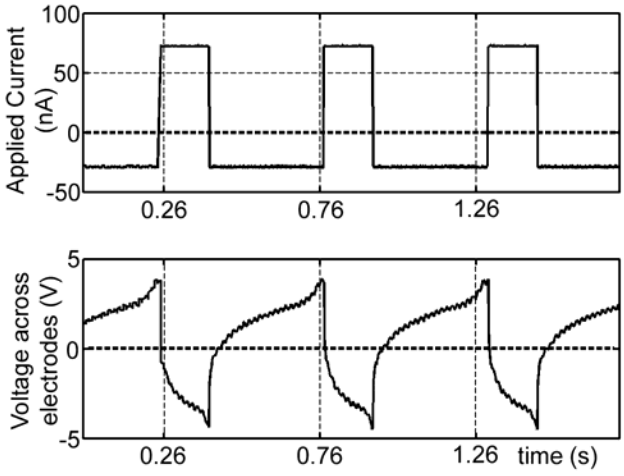

Fig. 3.9. Applied current signal (top) and voltage response (bottom) for two electrode electrochemical cell (Electro-osmotic pump) with DI water.

amplifiers (Burr-Brown, Inc., OPA445) to source the desired current waveform controlled by the function generator (HP33120A) and to measure the applied current signal and the voltage response with an oscilloscope. The applied current-time product is accurate within 95-98%. The resulting voltage response is very similar to what was expected for electrolysis with alternating currents as depicted in Fig. 8 with the solution resistance voltage drop included. In this example, only one reaction happens. If the

duration of the pulse is increased, it will switch to other reactions like oxygen evolution creating a net voltage response as will be discussed later.

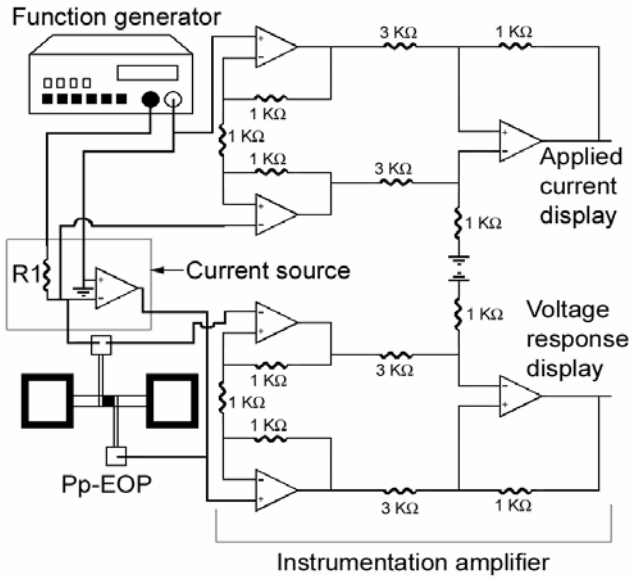

Fig. 3.10. Setup to measure voltage response of porous plug electro-osmotic pump (pp-EOP).

3.8 Current Voltage Relationship During Electrolysis

The voltage response of the electrochemical cell when a current is passed which causes electrolysis can be expressed as following [Atk98]:

$$E = E_{eq^+} \eta_R - \eta_L - I \cdot R_s \tag{26}$$

where η_R and η_L are the overpotentials of left and the right electrodes and $I \cdot R_s$ is the solution's ohmic resistance drop. From the Butler-Volmer equation and assuming a single electron transfer with α=0.5, the overpotential terms can be found to be [Atk98]:

$$E = E_{eq} - IR_s - \frac{4RT}{F} \ln \frac{I}{A\sqrt{j_{OL} j_{OR}}} \tag{27}$$

where j_{OL} and j_{OR} are the exchange current densities for left and the right electrode respectively. Also if the overpotential component due to concentration change (due to the diffusion limited case) is included using the Nernst equation, the total voltage due to electrolysis with an applied current can be found to be [Atk98]:

$$E = E_{eq} - IR_s - 2\frac{4RT}{F}\ln g(I) \tag{28}$$

$$g(I) = \left(\frac{I}{A\sqrt{j_{OL}\, j_{OR}}}\right)^2 \sqrt{\left(1-\frac{I}{Aj_{\lim,L}}\right)\left(1-\frac{I}{Aj_{\lim,R}}\right)}$$

where $j_{lim,R}$ and $j_{lim,L}$ are the current densities at the time of the maximum rate of diffusion. This happens when the reactant concentration at the electrode surface becomes zero as explained before. No current can exceed this value unless another reaction starts to take place.

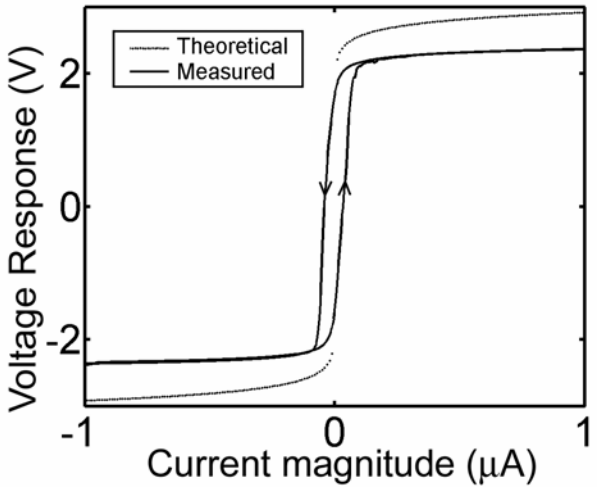

Fig. 3.11. Measured and theoretical voltage response of the electro-chemical cell to current sweep.

Experimentally, the voltage current response of the electrochemical cell in question (pp-EOP in this case) is measured using precision semiconductor parameter analyzer (HP4156a). The current level is swept from -1μA to 1 μA and then back to –1 μA and the voltage is recorded. The result is shown in Fig. 11. As expected the voltage-

current response of the cell is similar to a diode's and is very nonlinear. The expected theoretical voltage response from equation 28 is also plotted in the same figure. It can be seen that after very small current values, the voltage response saturates and becomes almost constant. This voltage is almost the same for both negative and positive current values and can be labeled as V_{sat}.

If an asymmetric current signal is applied with a duty cycle of *du*, then neglecting the time needed for double layer charging and surface oxidation and assuming that the frequency of the signal is small enough so that the electrode reactions reach the diffusion limited case in both positive and negative current cycle, the net voltage response over one period will be:

$$V_{net}=V_{sat}(1-2du) \tag{28}$$

This shows that the net voltage is directly proportional to the duty cycle of the signal. It will be seen later in section 4 that the experiments done with the electro-osmotic pumps verify this.

3.9 Theoretical Non-Gassing Limits For AC Current Drive

Electrolysis of water leads to generation of gas bubbles that can be deadly for the operation of the electro-osmotic pump. Zero averaged AC drive signal is applied to prevent this from happening before evolved gas can nucleate to form bubbles. Then the question is how much charge in one pulse can be injected into the electrochemical cell before evolving any gas. If it is done within the limits, the chemical processes happening at the electrode in one pulse can be reversed in the coming negative pulse. This way there will not be any gas generation. This has been investigated by Brummer et al [Bru77].

Their results give a conservative charge limit for platinum electrodes in saline solutions that will not cause any gassing. These results are important to identify the kinds of electrode reactions. In Fig. 12, voltage response of saline solution to biphasic current pulses of ±50 mA/cm^2, injecting ±1200 μC/cm^2 charge is shown. Different types of reactions occurring at the electrode are labeled in this figure. These reactions are:

HO: Hydride Oxidation (plus double layer)

DL: Double Layer

OF: Oxide Formation (plus double layer)

OE: Oxygen Evolution

O_2R: Oxygen (and oxide) Reduction

OR: Oxide (and oxygen) Reduction

HF: Hydride Formation (plus double layer)

HE: Hydrogen Evolution

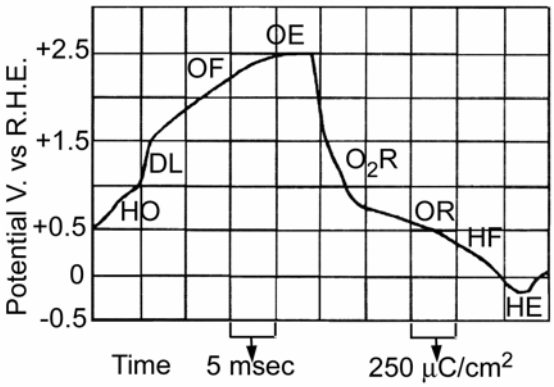

Fig. 3.12. Potential of platinum electrode with respect to reversible hydrogen reference electrode (R.H.E) in response to biphasic current pulses of 50 mA/cm^2 magnitude [Bru77].

The biphasic current stimulation can have two modes: lead and lag. In the lead mode, the electrode is first an anode and then a cathode (first the positive pulse, then the negative). The lag mode is the reverse of this. Their results showed that in the lead mode non-gassing limit is 420 μC/cm^2 and in the lag mode it is 490 μC/cm^2 [Ros90]. Again,

with the typical electrode dimensions used in this work of $30x200x10^{-4}$ cm^2, this corresponds to 24 nC. Assuming 1 second pulse, this is 24 nA current and assuming 1 KHz signal 24 μA. Considering the typical current values used in this work of around 100-350 nA for the low frequency alternating current drive, their value is considerably smaller. Yet, these practical, considerably higher values of current amplitudes used in this work led to no bubble generation within the test period of around half an hour. The reason for that is that the small value in Brummer's work shows just a theoretical, very safe limit of current that the reaction happening in one pulse will be totally reversed in the next cycle by assuring that there will not be any hydrogen or oxygen evolution stage at all. However in practice, HE and OE stages can also be used as long as the evolved gases do not nucleate and form bubbles. Then these evolved gases will be reduced in the negative cycle or some of the evolved gas will dissipate into the bulk because of the liquid flow. In this case, bubble nucleation criteria become very important which is a very complicated phenomenon and depends on current density, electrode roughness and already existing air pockets in the vicinity. In that sense, this drive will have repeatability and reliability issues. However, it is important to notice that with 1 KHz AC drive, even very safe limits of no gassing at all are not exceeded. Therefore for microfluidic systems where biological or chemical analysis will be made, high frequency AC drive is favored because it will generate orders of magnitude less products than low frequency current drive approach that may be fatal for the biological or chemical reagents under study.

3.10 Voltage Time Response Causing Net Flow

Even though the low frequency current drive can have repeatability and reliability issues, it generates a voltage response with non-zero average that can drive electro-osmotic pumps with suppressed bubble generation. The flow measurements of electro-osmotic pumps using this drive will be presented in the next section. However, now, qualitatively the voltage-time response of this drive will be discussed. Figure 13 shows an example of the resulting voltage response of a vertical electrode device with a 65 μm

long porous plug (this will be introduced in the next section) to the zero averaged injected current signal at 5 Hz with 30 % duty cycle and 700 and –300 nA amplitudes. The voltage response of the current drive is non-linear and changes with frequency. In that figure, sudden straight jumps at current switching points are due to solution resistance and are marked as SR. OF shows oxide formation and OR oxide reduction.

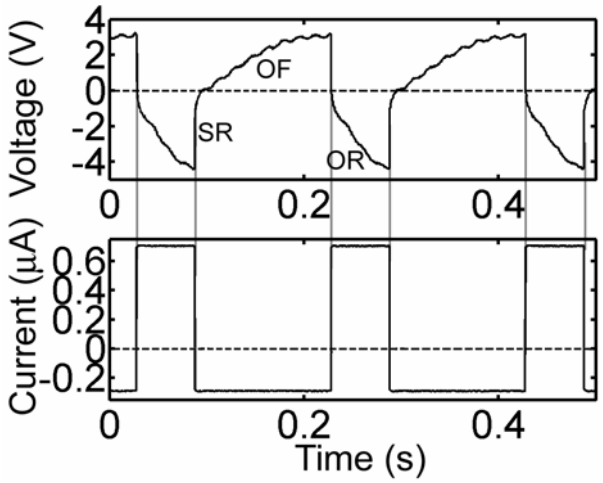

Fig. 3.13. Measured voltage response of a vertical electrode device with a 65 μm long plug and a 30% duty cycle current input with +700 and -300 nA amplitudes at 5 Hz, not causing any net movement.

These terms also include double layer capacitance charging and discharging. However, this drive does not cause any net voltage big enough to cause any net electro-osmotic liquid movement because the reaction does not become diffusion limited or it does not switch to other reactions. This is evident from the voltage response's being not saturated. However, the drive in Fig. 14 does. This is the same current drive as before but at 1 Hz. In this figure two different reactions can be identified, OF and oxygen evolution marked as OE. In the negative cycle, these are reduced with oxygen reduction marked as O_2R and OR [Bru77]. This drive generates big enough net voltage to drive net flow verified by observing the flow because the voltage response saturates. At frequencies higher than around 2 Hz, the voltage response does not saturate because the charging of the double layer and thin film oxide formation on the electrode surface take around 0.3 s for the 300

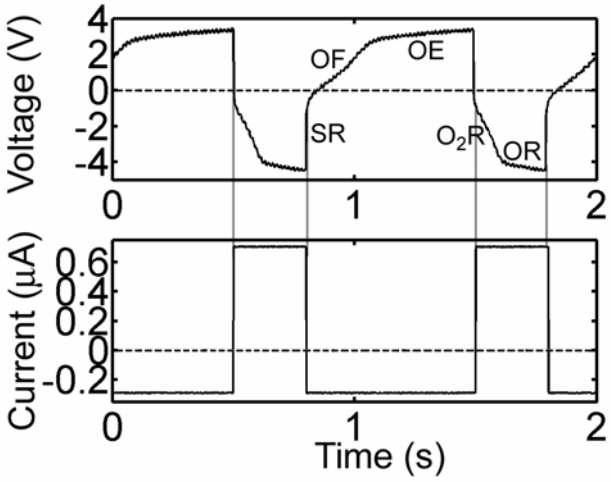

Fig. 3.14. Measured voltage response of a vertical electrode device with a 65 μm long plug and a 30% duty cycle current input with +700 and -300 nA amplitudes at 1 Hz, causing net movement.

nA cycle and 0.13s for the –700 nA cycle. This explains the frequency dependence of the drive. After a critical frequency value, the voltage response will saturate and the voltage response will have a net value. If the frequency is decreased further, the net voltage will become bigger because the time needed to go into saturation will be negligible compared to the duration of the current cycle. Therefore, in order to get net movement, the applied current must be long enough to go into the diffusion-limited case and even to other reactions. However in that case electrodes get corroded and the device performance degrades and repeatability and reliability become an issue. Also as the frequency goes below 1 Hz or the amplitude of the current signal is increased, bubbles may be generated more easily. However observations showed that zero averaged current drive at frequencies higher than 5 Hz is more immune to bubble generation than the same frequency zero averaged voltage drive. Therefore, current drive at frequencies higher than 5 Hz must be preferred for electro-osmotic pumps even though this does not generate net flow. Then diffuser nozzle configuration [Ols99] or AC flow rectification [Mut04] methods (explained in Section 5) can be used to generate net flow. Salt gel [Tak03] or liquid bridge [Mut04] approaches (explained in Section 5) can also be used to generate net flow with DC voltages without bubble generation problems. Therefore these methods must be preferred instead of the low frequency current drive.

3.11 Conclusion

In this section, a brief explanation of an electrochemical system consisting of two metal electrodes and an electrolyte has been done to try to understand the safe operation limits of electro-osmotic pumps. The reactions happening at the electrode-electrolyte interface are divided into two: faradaic and non-faradaic reactions. Non-faradaic reactions are due to charging and discharging of double layers at the interface and they do not cause any chemical reactions. This can be assured by limiting the amount of charges injected into the system. High frequency (~KHz) excitation used in this work is within this safe limit. As the amount of charges injected exceed these safe limits, charge transfer will occur across the interface causing faradaic reactions. This reaction can be assumed to be linear for only very small current values as studied by Schwan. For larger overvoltage values, the voltage-current relation will be nonlinear, similar to a leaky diode as expressed in the Butler-Volmer equation. In this regime, the system is in charge-transfer control regime, meaning there are abundant reactants around and the reaction rate is limited to the rate charges cross the interface. However, there is even a more non-linear regime beyond this governed by the mass transfer, specifically diffusion. As the reactions go on at the electrode surface, the reactants are depleted. The only way, they can be supplied to the electrode surface is by the mass transfer (diffusion) from the bulk. Therefore in this regime, the voltage-current response of the system is diffusion controlled. The safest and most reliable way of operating the pumps is by using low current values so that only non-faradaic reactions and totally reversible electrode surface oxidation and reduction without diffusion would happen. However, within these values the net voltage response is very small. This would not create a useful net flow in the electro-osmotic flow. Other flow rectification methods must be used for this safe drive. If high amplitude current signal at low frequency is applied and reversed, the voltage-current relationship will be governed by both charge-controlled and diffusion controlled

regimes, causing high nonlinearities. This creates net flows in electro-osmotic flow. However, bubble nucleation, which depends on current density, surface roughness and already formed bubbles at the vicinity, limit the current levels that can be put on the system. Then combined with the electrode corrosion, this drive has repeatability and reliability issues. Therefore other drives must be used to drive electro-osmotic pumps as will shown in section 5.

SECTION 4
SURFACE MICROMACHINED POROUS-PLUG ELECTRO-OSMOTIC PUMP

4.1 Introduction

In this section, a porous plug electro-osmotic pump (pp-EOP) is introduced and discussed. This device has been fabricated by surface micromachining a porous polymer plug and integrating it into a parylene channel with embedded electrodes. The schematic of the pumping device is shown in Fig. 1, where the porous plug is placed in the center of the microfluidic channel and on each side of the plug is an electrode. As a voltage is applied between the electrodes an electric field is formed acting on the double layer of charges at the interface between liquid and the walls of the pores of the porous plug thus giving rise to electro-osmotic flow (EOF). The key design parameters for this device are the pore size, channel width, porous plug length and the electrodes type, spacing and width.

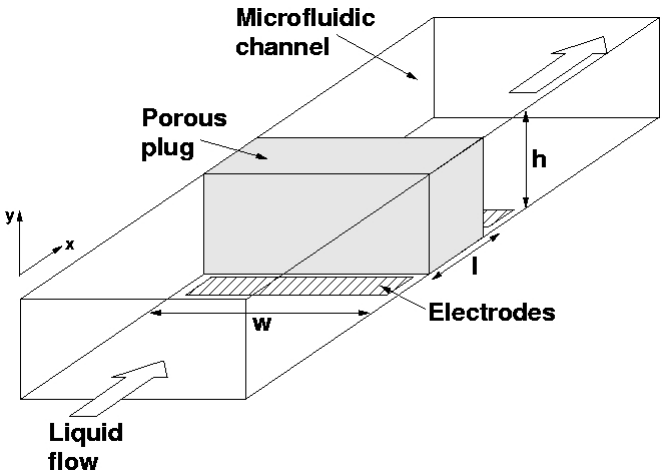

Fig. 4.1. EOF pump schematic

This section also introduces different electrode types, planar and vertical employed in the electro-osmotic pump. The fabrication section explains the casting technique developed to micromachine the porous polymer plug and gives fabrication processes for porous plug electro-osmotic pumps with both planar and vertical electrodes. In the results and discussion section, porous polymer is characterized and electro-osmotic mobilities of different devices are measured. This is followed by a discussion of a new drive, periodic, asymmetrical, net zero average AC current signal in a specific frequency range to suppress bubble generation while producing non-zero average voltage thus a net lateral motion. Test results of this drive are presented mentioning its reliability and repeatability issues therefore advising to use other drives.

4.2 Electrodes

Two different electrode configurations have been considered. First, a planar electrode pair is used on both sides of the porous plug as shown in Fig. 2(a). The new vertical electrode design is shown in Fig. 2(b). The equipotential and field lines have been plotted in Fig. 2 (c) and (d) for both electrode configurations.

The vertical electrode pair provides a nearly constant field profile in the x-direction for all values in the y-direction; hence across the porous plug. In addition, the vertical electrodes provide much larger surface area than the planar design, thus larger currents can be used before any bubble generation occurs since bubble nucleation is proportional to the current density. Larger currents result in higher voltages and consequently larger flow velocities. Furthermore, for the same current amplitudes, vertical electrodes have much better resistance to bubble generation and are, therefore, more stable. Using an electrode gap space $w=50\ \mu m$ and width $s=30\ \mu m$, porous plug (and vertical electrode) height $h=20\ \mu m$, and voltage difference between the plates of $\Delta V=5\ Volts$, the magnitude of the electric field |E| has been plotted for both electrode configurations as shown in Fig. 3. From Fig. 3, the magnitude of the electric field for the vertical electrode pair is constant $E_x=5\ Volts/50\ \mu m = 10^5\ V/m$ for all values of x. The field magnitude for the planar electrode pair decreases moving from the electrode surface

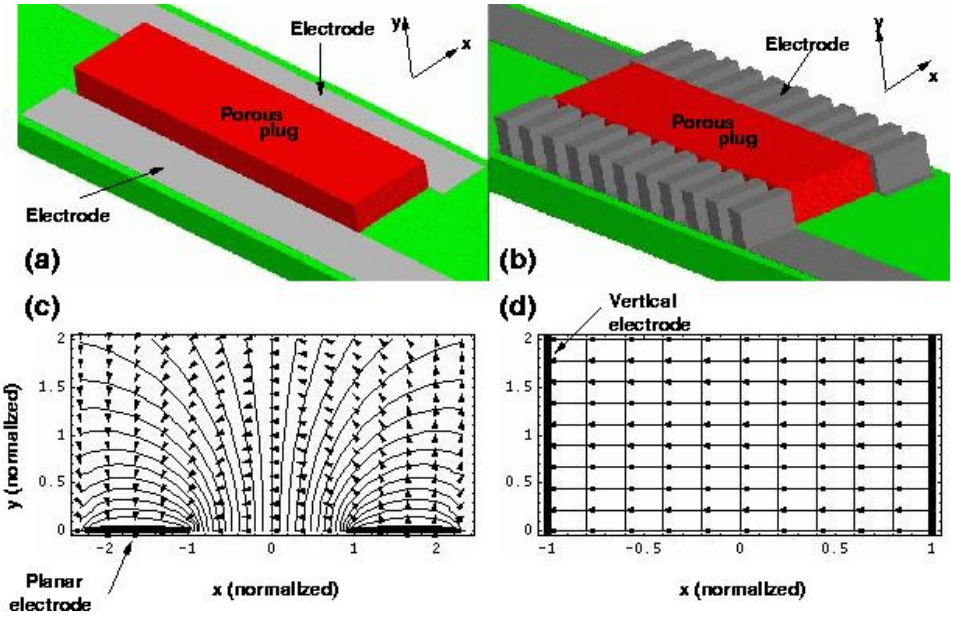

Fig. 4.2. Electrode configurations (a) planar (b) vertical (pillar) and corresponding equipotential and electric field lines for (c) planar (d) vertical. The units of plots (c) and (d) have been normalized with 1 corresponding to 25 μm. Flow is along x axis.

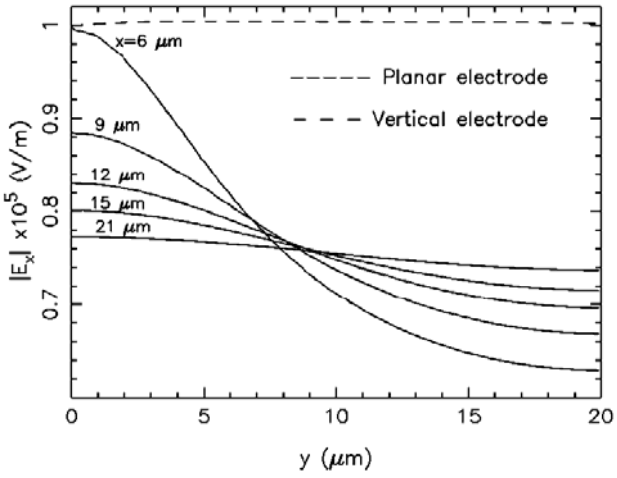

Fig. 4.3. Simulation results of two-dimensional planar (solid line) and vertical (dotted line) electrodes. First electrode is located at *x=0*. The gap between electrodes is *50 μm*. Applied voltage is *5 Volts*. The distance *y* is from substrate surface (0 μm) to 20 μm.

to the top of the channel, hence increasing the y distance. The average electric field magnitude for the planar electrode pair shown here is $0.75x10^5$ *V/m*. Thus the 2-d

simulation of electric fields shows 1.3 times increase in the average electric field magnitude.

More importantly, the surface area exposed to the fluid has been drastically increased with the vertical electrode configuration. Using the dimensions of the planar electrodes mentioned earlier, the exposed surface area of single electrode is $A_p=(200)(30)\ \mu m^2=6000\ \mu m^2$. For a vertical electrode configuration as mentioned earlier with 9 pillars each 20 μm tall and 10 μm wide the total exposed surface area for a single electrode is $A_v=204000\ \mu m^2$, corresponding to a 3.4 time increase in electrode area.

4.3 Device Fabrication

The fabrication development of the pp-EOP is done in two steps. The first development step is concerned with the technology to cast and pattern the porous plug material. The second process development step is to integrate an existing surface micromachining process technology [Man01,Car01,Web99,Sel02a] with the porous plug process steps. The final pp-EOP devices are fabricated using low temperature surface micromachining technology. The planar electrode devices use a four-lithography mask process while the vertical electrode fabrication process requires five.

4.3.1 Porous plug (pp) fabrication

The key element of the new electro-osmotic pump is the porous plug, where a new porous polymer, poly(butyl methacrylate-co-ethylene dimethacrylate) is used. The porous material is formed by casting its monomer solution along with porogens inside a mold. The monomer solution was prepared by mixing 0.8 g ethylene dimethacrylate (EDMA), 1.18 g butyl methacrylate (BMA), 20 mg azobisisobutyronitrile (AIBN), 2.214 g 1-propanol and 0.486 g 1,4-butanediol (Sigma-Aldrich, Corporation). The key to the utility of the porous material is that the pore size can be easily adjusted from tens of

nanometers to couple microns by changing the volume percentage of 1-propanol in the porogenic mixture (1-propanol and 1,4-butanediol) of the monomeric solution as shown in Fig. 4 [Yu00]. An interesting property of the new porous material is that the surface

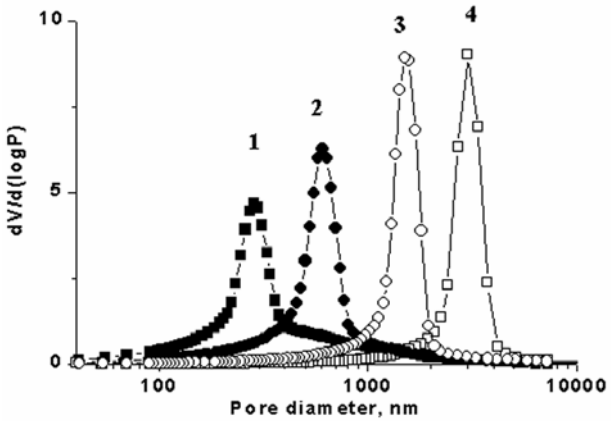

Fig. 4.4. Pore size distribution profiles of monolithic polymers with different percentages of 1-propanol. Percentage of 1-propanol in the porogenic mixture (1-propanol and 1,4-butanediol): peak 1) 80%; 2) 78%; 3) 76%; 4) 74%. [Yu00]

charge density of the pore walls, and hence zeta potential, can be controlled by adding different percentages of the aqueous solution 2 -acrylamide-2-methyl-1-propanesulfonic acid (AMPS) (Sigma-Aldrich, Corp.) dissolved in water [Pet98].

The main challenges in casting the polymer are caused by its low viscosity and inability to polymerize in the presence of oxygen. These major processing difficulties are overcome by using a three step casting procedure as shown in Fig. 5. First, a square opening in the glass wafer is wet-etched in a $7HF:3HNO_3:10H_2O$ solution with a Cr/Au (20/100 nm) mask to a depth of 20 μm. The cavity etched in the glass wafer is the mold for the low viscosity monomer. The polymer solution is bubbled with N_2 gas for 5 minutes to remove the dissolved O_2 inside. Then the cavity, or mold, is filled with the monomer solution. The process wafer, typically oxidized silicon is then placed in contact with the glass wafer and the monomer solution. The solution trapped between two wafers

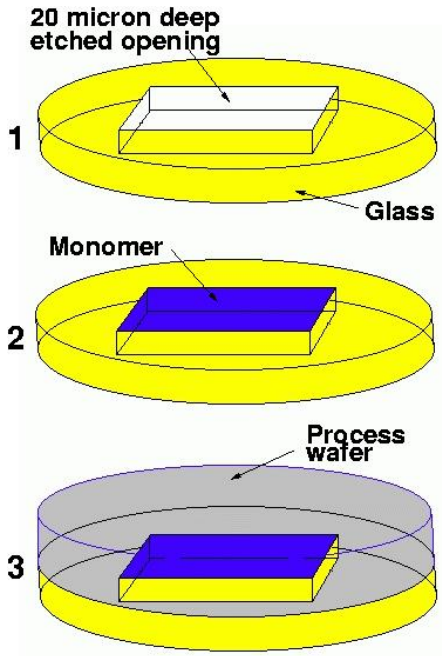

Fig. 4.5. Three step casting process of the porous polymer solution. After casting, solution is polymerized either by heat or *UV* exposure. After polymerization, since the liquid becomes solid with solvents inside the pores, wafers separate easily.

is polymerized by either heating on a hotplate at 55°C for an extended period of time (typically 10 hours or more) or by *UV* polymerization. Adhesion of the porous polymer to silicon, silicon oxide and other polymer films, such as parylene-C, is aided by deposition of a few monolayers of an adhesion promoter (10:10:1) Deionized (DI) H_2O:isopropyl alcohol (IPA):gamma-methacryloxytropyl trimethoxy silane (A174, Specialty Coating Systems, Inc.) under low pressure (10 mTorr) for 3 hours. Exposing parylene and oxide coated substrates to a short oxygen plasma typically increases the effectiveness of the adhesion promoter.

The casting process forms a 20 μm thick film of porous polymer on top of the process wafer. In order to pattern the porous polymer a metal (Ti) mask is defined using a lift-off process. The unmasked polymer areas are etched in an O_2 plasma (Semi-Group,

Inc.) at *50 mTorr* and *150 Watt* power. Figure 6 shows an example of a patterned porous polymer structure between two planar metallic electrodes.

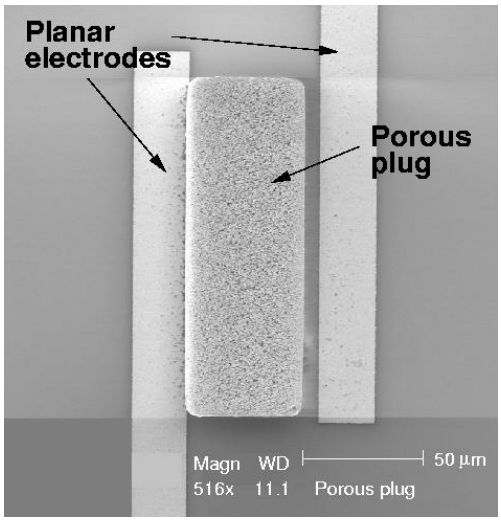

Fig. 4.6. Scanning electron micrograph (SEM) of patterned porous polymer plug. Patterning of the polymer was done by reactive ion etching unmasked areas. Ti was used as a mask, which was patterned by a lift-off process.

Photo definition of the porous polymer with *UV* light (365 nm) is also possible. However, this requires large energy density on the order of *1.5 J/cm*^{2}. During this period, the sample also needs cooling because the added heat increases the material polymerization rate. The resulting pattern typically has low resolution (*~50 µm*) due to shifts of the monomer solution. A contact aligner may improve the resolution, but will require extensive modification.

4.3.2 Pp-EOP fabrication

The fabrication of the pp-EOPs integrates the fabrication of the porous polymer plug, described in the previous section to an existing surface micromachined process technology [Man01,Car01,Web99,Sel02a]. Two fabrication processes are used to form the two different electrode structures. The fabrication of the planar electrode devices is

presented first. The fabrication of the vertical electrode devices requires an additional lithography and nickel electroplating steps to form the tall, vertical electrodes.

4.3.2.1 Planar electrode devices

A simplified fabrication sequence of the pp-EOP is shown in Fig. 7, which uses four lithography steps

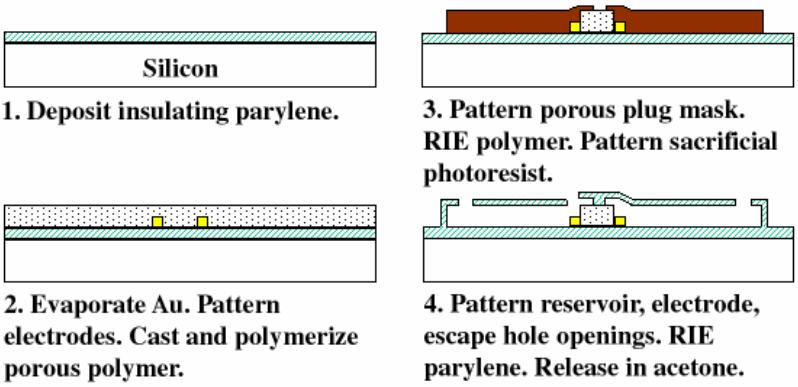

Fig. 4.7. Simplified process flow for a planar electrode pp-EOP device.

and low temperature processes. Since all process steps are low temperature, the substrate can be any desired material (e.g. silicon, glass, plastic). For silicon substrates, the process begins by vapor depositing a 5 μm thick p-xylylene (parylene-C) for electrode insulation. The parylene layer forms the bottom layer of the channel. A thermal oxide (about 1 μm thick) can also be used as the insulation layer. A 200 nm layer of gold (Au) is next electron-beam (e-beam) evaporated and patterned forming the planar electrodes. The 20 μm-thick porous polymer plug is formed and patterned as explained in the previous section. Next a 20 μm-thick layer of photoresist is patterned as a sacrificial layer to form the channel and reservoirs. In this step, extra care should be paid in clearing the resist on top of the porous plug to avoid a resist bridge. The resist is only removed on a small section on the top of the plug. Next, a 4 μm thick layer of parylene is vapor deposited to form the walls of channels. A layer of 20 μm-thick photoresist is then used as a mask to

plasma etch holes on the parylene (Gas: 100 sccm O_2; Pressure: 100 mTorr pressure; RF Power: 100 Watts). This etch defines the reservoir and electrode openings and a 30x60 μm^2 bubble escape hole near the porous plug. The sacrificial resist under the channels is next removed in an acetone bath. The escape hole decreases the sacrificial etch time and allows trapped air present between the plug and the reservoir that are intentionally or unintentionally generated during testing to escape. Fig. 8 shows a picture of a finished device.

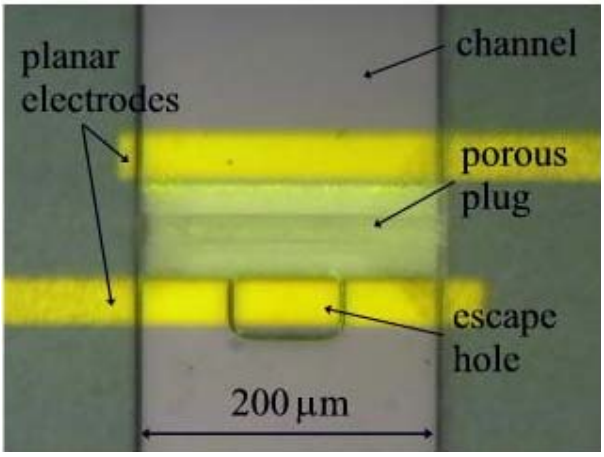

Fig. 4.8. Microscope photograph of a fabricated planar electrode pp-EOP device.

4.3.2.2 Vertical electrode devices

The fabrication process for the vertical electrode devices on silicon substrates begins by growing a 2 μm thick oxide isolation layer for the electrodes. A Cr/Au (30/500 nm) electroplating seed layer is e-beam evaporated. The Au layer is patterned and etched. A 20 μm thick photoresist electroplating mold is patterned (pillar openings). A 20 μm thick nickel layer is electroplated on the exposed gold layer (sulfamate, MacDermaid, Inc.). Following the nickel electroplating step, the photoresist mold is removed. The Cr adhesion is then removed. The 20 μm thick porous plug is fabricated using the process outlined in the previous section. Next a 20 μm thick layer of photoresist is patterned forming the sacrificial layer for the microfluidic channels and reservoirs. The resist is

only removed from a small section on the top of the plug. A 5 μm thick layer of parylene is then vacuum deposited forming the walls of the channels. Next, a 20 μm-thick photoresist layer is used as a mask to etch reservoir and contact pad holes in the parylene in an O_2 plasma (Semi-Group, Inc.). The sacrificial photoresist is released in an acetone soak. Figure 9 shows a simplified process flow for fabricating the vertical electrode pp-EOP device. Figure 10 shows a microscope photograph of a fabricated vertical electrode pp-EOP.

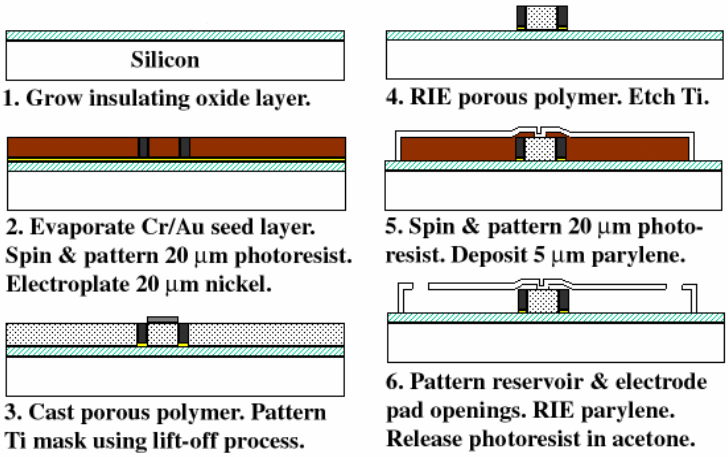

Fig. 4.9. Fabrication process flow for a vertical electrode pp-EOP device.

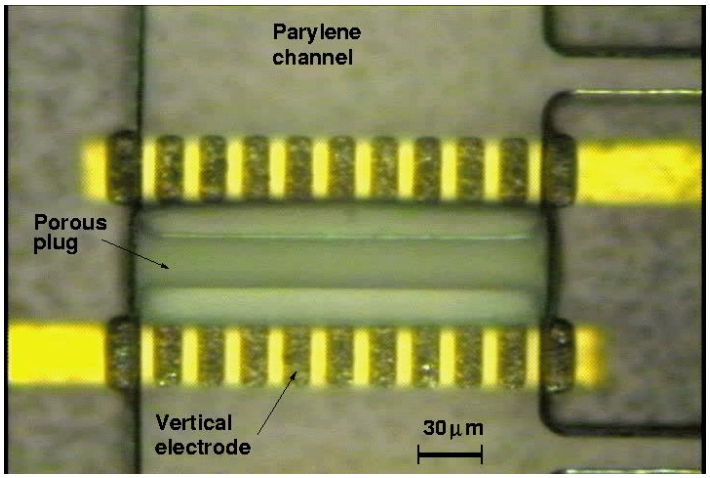

Fig. 4.10. Top view of a fabricated vertical electrode pp-EOP device.

4.4 Porous Polymer Characterization

As explained in section2, tortuosity, τ and porosity, Ψ values of a porous polymer structure are important to characterize the flow through it. Especially the ratio of τ/Ψ must be known since both the electro-osmotic flow and the pressure driven flow through the porous structure has this term in their expression as shown in section 2 and repeated below in equation 1.

$$Q = -\frac{\Psi P_z A a^2}{8\eta\tau} - \frac{\Psi\varepsilon\varepsilon_0\zeta E_z A}{\eta\tau}\left(1 - \frac{2I_1(\kappa a)}{\kappa a I_0(\kappa a)}\right) \tag{1}$$

From the macro scale measurements, using mercury intrusion porosimetry it is known that $\tau\approx2$ and $\Psi\approx0.6$, corresponding to $\tau/\Psi\approx3.3$. Porosity can be found by weighting the wet and dry polymer to determine the void and the total volume. τ/Ψ ratio can be found by measuring the liquid resistance of a column with and without the porous polymer (Zen01). The electrical resistance with and without the polymer plug in the channel is shown below.

$$R_{el_with} = \frac{\rho_1 L\tau}{\Psi A} \qquad R_{el_without} = \frac{\rho_1 L}{A} \tag{2}$$

From this, the ratio of resistance with and without the porous polymer can be found to be:

$$\frac{R_{el_with}}{R_{el_without}} = \frac{\tau}{\Psi} \tag{3}$$

Experiments have been done to measure this resistance ratio to find the τ/Ψ. In the same parylene channel, two devices have been fabricated, one with just two planar electrodes and the other with the electrodes and the porous plug in between. The gap between the electrodes is 40 μm and the channel has a cross section of 20x200 μm^2. 0.1 M NaCl

solution is used to fill the parylene channel. The resistivity of the solution can be calculated from equation 8 in section 2. The conductivity of the solution is: σ=0.1x1000x(50.08+76.31)x10^{-4}=1.26 S/m. The resistance of the solution without the polymer is then: $R_{el_without}$=40x10^{-6}/(1.26x20x200x10^{-12})=7900Ω. To measure the resistances an LCR meter (HP4284a) is used. Because of the double layer capacitances in series with the solution resistance, measurements must be done in frequencies around 200 KHz and above but below the effect of other parasitic capacitances (Boh00) start to interfere like the oxide capacitance and the solution capacitance. The measurement are

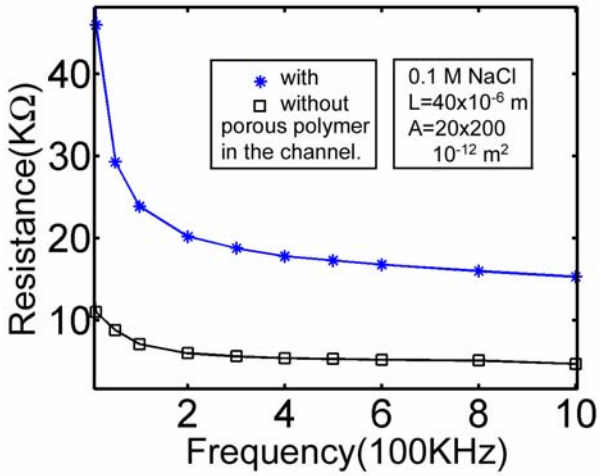

Fig. 4.11. Resistance measurements of the device with and without the porous polymer.

shown in Fig. 11. This shows a solution resistance of around 6000 Ω, which is close to the calculated value. The ratio of resistances from 200 KHz to 1 MHz changes from 3.14 to 3.37 with an average value of 3.27, which is almost the same as the macroscale result of 3.3. So this value can also be used for micromachined porous plug in the flow calculations.

4.5 Results and Discussion

Device test results presented in this section have been measured for devices with a 82% 1-propanol porogenic mixture porous plug material corresponding to a 200-300 nm

average pore size. Devices with both planar and vertical electrodes have been analyzed. All devices have been tested with DI water only.

Two different measurements have been made on the pp-EOPs. First, electro-osmotic velocities of the devices with planar and vertical electrodes are measured as well as parylene channels with just planar electrodes but no porous plugs for different magnitudes of applied voltages. This is done to characterize the electro-osmotic mobilities of devices and to find the zeta potential of the porous plug indirectly. Second, the velocity of the DI water-air interface is measured for a current stimulus. The current stimulus is a low frequency, zero net current (and zero net charge) pulsed current signal which produces a net non-zero average voltage response, which has been found to suppress bubble formation at the electrode interface as explained in the previous section. The net direction of the flow is determined by the duty cycle and the nonlinear behavior of the electrode interface.

4.5.1 Electro-osmotic Velocities Versus Applied Potential

Electro-osmotic mobilities of the electro-osmotic pumps can be found by plotting their electro-osmotic velocities versus electric fields across electrodes. Since DC voltages cannot be applied to the electrodes inside the channel (they cause bubble generation), symmetrical AC square voltage waveforms with amplitudes as high as 4 volts are applied to devices at 1 Hz. The liquid velocity is measured by measuring the velocities of 1 μm latex bead in field free regions. When the AC voltage is applied beads move back and forth with net zero movement. Since the applied voltage frequency is low (1 Hz), this movement can be recorded to measure the maximum displacement in either negative or positive cycle of the applied signal. However, this method allows voltage magnitudes of maximum of around 4 volts since bigger amplitudes result in bubble generation.

Measurements are done for planar electrode porous plug pumps with a plug length of 65 μm, vertical electrode porous plug pumps with a plug length of 65 μm and a parylene channel with two inside electrodes but no porous plug separated by 65 μm. The results are shown in Fig. 12. It is clear that for the same applied voltages, vertical electrode

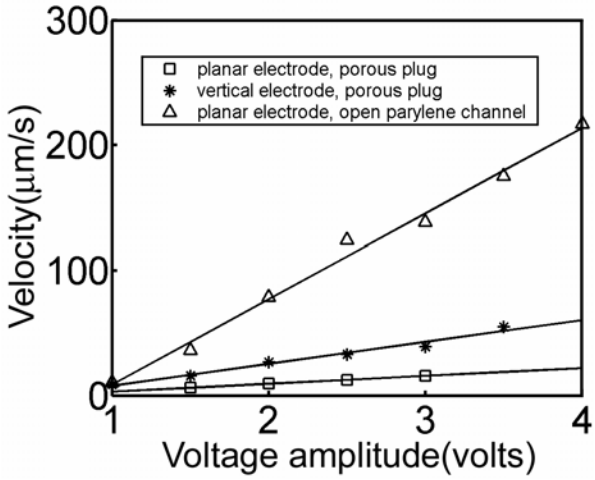

Fig. 4.12. Electro-osmotic liquid (DI water) velocity versus applied voltage magnitude of two electrodes with a gap of 65 μm inside parylene channel and of planar and vertical electrodes with 65 μm long porous plugs in between.

porous plug device gives higher velocities compared to planar porous plug device. This is due to non-uniform electric field across the porous plug with planar electrodes. Vertical electrode device velocities are 2.8 times higher than the planar electrode ones. This is higher than the expected improvement of 1.3 found from electric field simulations. Since, with vertical electrodes, electric field magnitude can be found simply dividing the voltage by the electrode gap (this is not true for the planar electrode), electro-osmotic mobility of this device can be found to be 1.14×10^{-9} $m^2/V.s$. From equation 1, with values of $\tau/\Psi=3.3$, and average pore radius of 150 nm (to calculate the double layer collapse affect), zeta potential of this porous polymer can be found to be –27 mV. For vertical electrodes, 3 volt DC drive corresponds to a flow rate of 4.8 nL/min. This gives a maximum pressure that can be generated of 1540 Pa.

Similarly, electro-osmotic mobility of the parylene channel can be found. In this calculation, since measurements are done with planar electrodes, a correction factor must be included for the electric field magnitude. This factor is 2.8 as found for the porous plug devices. Then the electro-osmotic mobility of the parylene channel is 1.24×10^{-8} $m^2/V.s$. This corresponds to a zeta potential value of -18mV for the parylene channel.

4.5.2 Low Frequency Zero Averaged Current Drive

In conventional EOP of aqueous solutions gas bubbles are generated at the electrodes due to application of high potential. The amount of gas generated is proportional to the amount of net charge transferred across the electrode/electrolyte interface to the H^+ ions in solution resulting in a steady current. The flow velocity is also linear with the applied voltage. Bubble generation can be suppressed if the driving waveform has zero net current where reactions going on during positive current cycle would be significantly reversed under negative cycle before any reactant gas molecules had enough concentration to nucleate a bubble.

As explained in the previous section when two electrodes in a cell are in contact with water they have a linear current-voltage relationship under low voltages or high frequencies. In these regimes a zero average current results in zero average voltage, and therefore no net fluid movement. At low frequencies, however the cell shows a non-linear current-voltage characteristic due to activation control as expressed in Butler-Volmer equation [Sel02b], [Boc73]. Also further non-linearity arises as potential is increased due to switching from activation controlled to diffusion controlled state [Sel02b] and due to switching to other reactions like electrode oxidation; hence a zero-averaged current signal yields a non-zero averaged voltage and net motion. Net fluid motion is then obtained if a current waveform of the shape shown in Fig. 13 is applied at low frequency (DC to 5 Hz).

The flow velocity is measured by first filling the open reservoir on one side of the channel with water. The water naturally wicks into the channel and stops at the plug due

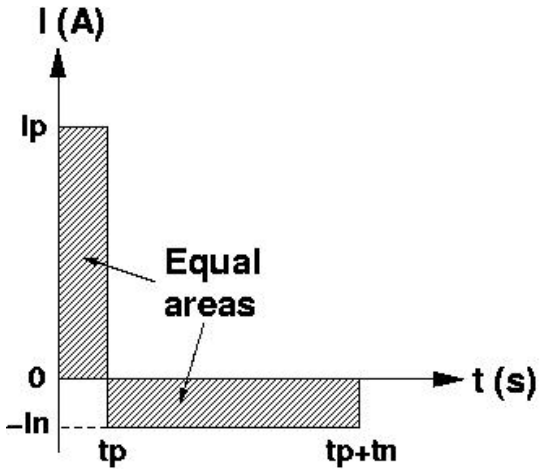

Fig. 4.13. Characteristics of the applied current signal with duty cycle $D = t_p/(t_p+t_n)$, frequency $f = 1/(t_p+t_n)$ $(I_p \cdot t_p = I_n \cdot t_n)$.

to high surface tension. However wetting of the polymer is an issue. In some cases it gets wet by itself and then fills the other side of the channel slowly due to surface tension in the channel especially with plug lengths less than 100 μm. In other cases, the polymer is wetted by introducing acetone from the other side of the channel. Acetone wets the polymer. Since it evaporates very quickly, water gets sucked into the polymer and wetting it but not going any further in the channel. Then the periodic current signal is applied to the cell and the DI water-air interface movement velocity is recorded. However these velocity measurements may have offset errors due to surface tension movement component. Later the measurements are done using latex beads in field free region after the whole channel is primed.

DI water-air interface movement velocity is recorded using the flow velocity measurement apparatus, shown in the schematic in Fig. 14. Flow velocity is measured for devices with both planar and vertical electrodes. Water-air interface movements in response to applied current signals are recorded using a color CCD camera (Topica TP-8002A) attached to a microscope. The interface movements are digitized with a video capture hardware (30 frames/s) and analyzed using a commercial software package (Adobe Premiere).

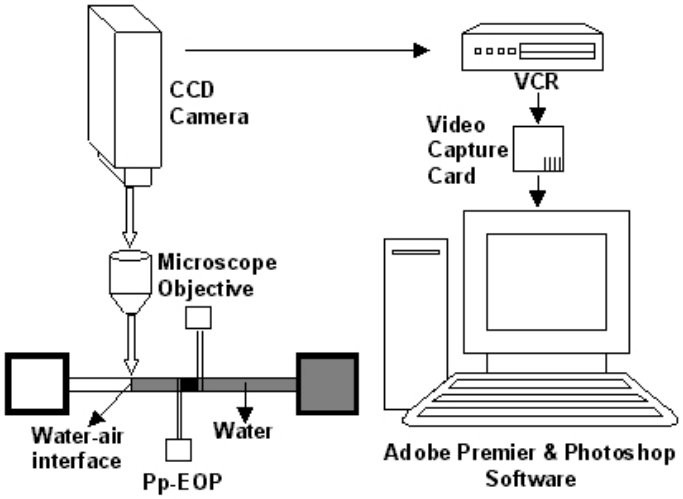

Fig. 4.14. Water-air interface flow velocity measurement apparatus.

4.5.2.1 Planar electrode measurements

A 30 % duty cycle step current signal with +700, -300 nA amplitudes at different frequencies is applied to the cell and the DI water-air interface movement velocity is recorded. The forward and reverse movement of the water-air interface inside the channel is shown in Fig. 15. The direction of the flow can be changed by reversing polarities of the signal. The resulting fluid velocity is a function of the frequency of the injected signal. Fig. 16 shows the frequency response of the net velocity of water-air interface. The maximum velocity was 1.8 μm/sec at 0.8 Hz. Although, this device is slow, it can be used for precise pumping. 50 μm long porous polymer has a hydraulic resistance of 1.48×10^{16} Pa.s/m^3. Then the maximum pressure that can be generated with these pumps is

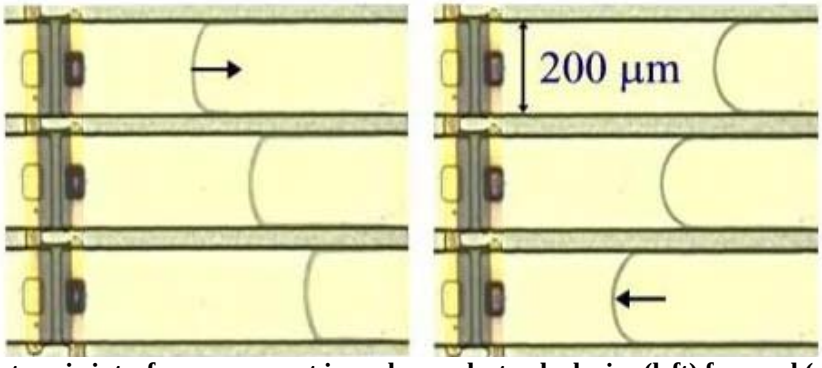

Fig 4.15. Water-air interface movement in a planar electrode device (left) forward (right) reverse.

107 Pa. This is a very low pressure value and it cannot be measured experimentally with the current setup. That is another reason why the generated flow does not go through the escape holes. However this low-pressure value is enough to generate flows in microfluidic channels. Furthermore cascading them can increase it. Since they consume small chip area, they can be cascaded in large scale.

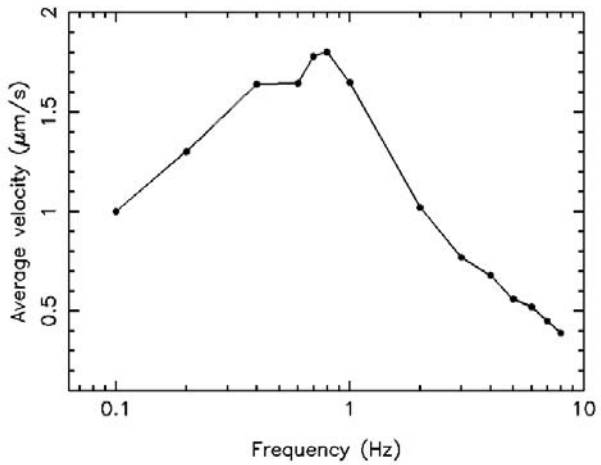

Fig 4.16. Average velocity of water-air interface with straight channel as a function of drive frequency.

However, since the purpose is to use this device in integrated microfluidic systems, faster motion can be achieved simply by necking-down the channel. Fig. 17 shows a 200 μm wide regular channel necked down to 50 μm and 20 μm from the end of the plug at a 45º angle. The measured flow rates are shown in Fig. 18.

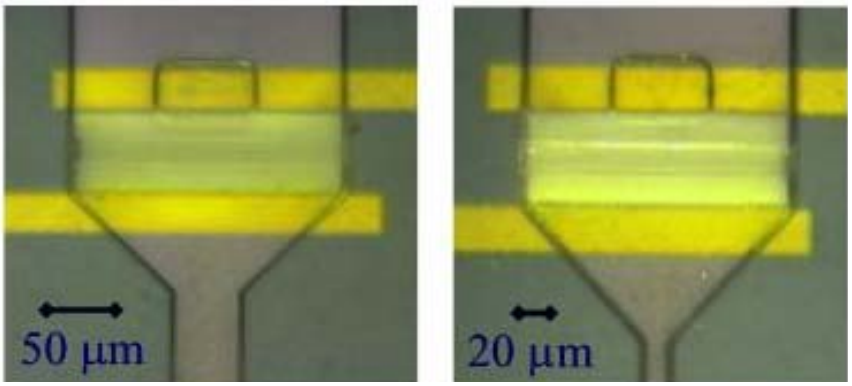

Fig. 4.17. Devices with "necked-down" channel from 200 μm to (left) 50 μm (right) 20 μm .

The 50 μm device has a maximum velocity of 4.8 μm/s at 0.8 Hz whereas the 20 μm device has a maximum of 13.9 μm/s at 0.8 Hz. These devices all show the same velocity vs. frequency profile with a peak around 0.8 Hz. Flow rate reduction below 0.8 Hz is due to bubble growth below that frequency reducing the flow rates and finally blocking the whole flow. Flow rate increase up to that frequency is consistent with the argument made for low frequency asymmetrical current drive. In order to go to diffusion limited region, it takes a finite amount of time. Therefore as the duration of a current cycle is increased it stays longer in the diffusion limited case and hence results in larger net flow.

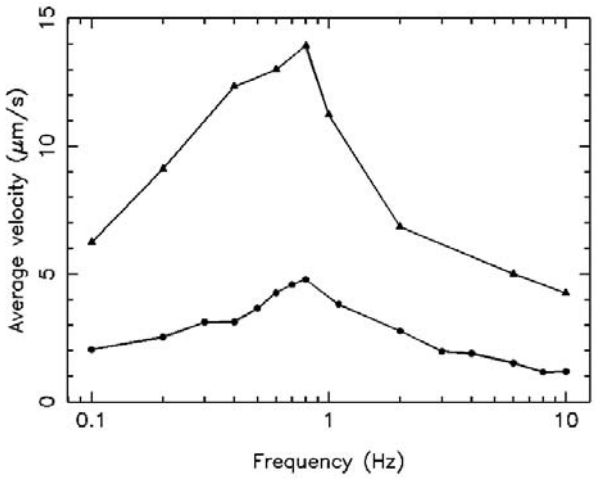

Fig. 4.18. Average velocity as a function of frequency with *necked-down* channel from 200 μm to 50 (circles) and 20 μm (triangles).

4.5.2.2 Vertical electrode measurements

Water-air interface movements in response to applied current signals are recorded using the same measurement system shown earlier. A 30 % duty cycle step current signal with +350, -150 nA amplitudes (smaller than planar electrode devices) at different frequencies is applied to the cell and the DI water-air interface movement velocity is recorded. The forward and reverse movement of the water-air interface inside the channel

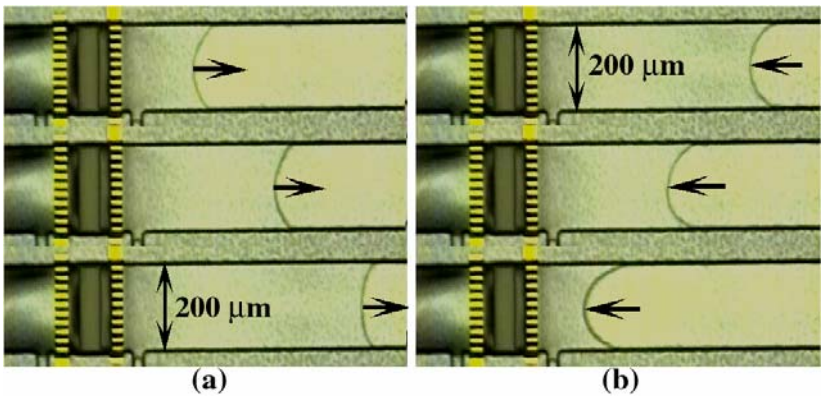

Fig. 4.19. Water-air interface movement for vertical electrode device (a) forward (b) reverse.

is shown in Fig. 19. Fig. 20 shows the effect of duty cycle on average velocities. Signals at same frequencies are applied with same amplitude-duration product. Velocities increase with smaller duty cycle. This implies that short current pulses with high amplitudes produce

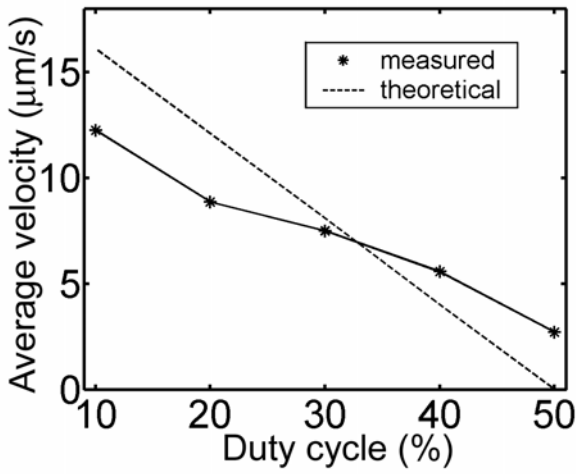

Fig. 4.20. Average water-air interface velocities of a device with 130 μm long plug in response to different duty cycled step current signals at the same frequencies with same amplitude, duration products.

higher velocities. This is in good agreement with the net voltage analysis of the electrochemical cell made in the previous section. The theoretical results shown in this figure is calculated by first finding the net voltage generated with different duty cycled signals using equation 27 in section 4. Then this value is used with the electro-osmotic

mobility of the vertical electrode porous plug device that has been found in the previous section to find the average velocity. However, limit to this increase is bubble generation. If the current amplitude increases too much at lower duty cycle, unstoppable bubble generation happens before an opposite cycle can start.

Figure 21 shows the net velocity of water-air interface in response to current signals at different frequencies. Similar to the planar electrode devices, the flow rate increase with lower frequency value can be explained with a finite amount of time (around 0.1 s) required to reach the diffusion limited case. However in this case the increase continues for even frequency values below 0.8 Hz because the device is more immune to bubble generation with vertical electrodes. The maximum velocity is around 16 μm/sec. This is equivalent to a flow rate of 3.8 nL/min, which shows around 9-fold increase compared to the device with planar electrodes. R_{hyd_EOP} for this device is $3.58x10^{16}$ Pa.s/m^3. Then the maximum pressure that can be generated is 2463 Pa.

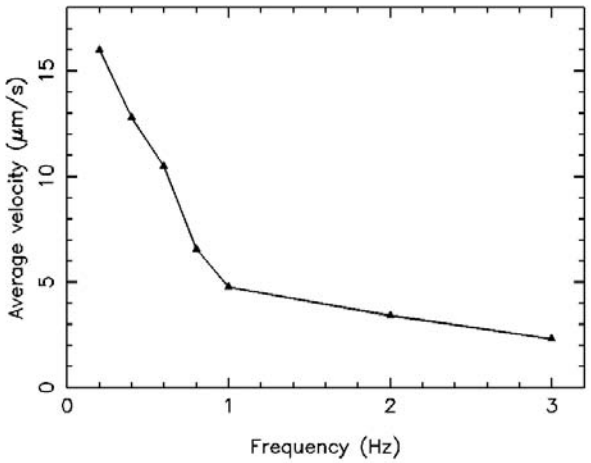

Fig. 4.21. Average water-air interface velocities of the device with 130 μm long plug as a function of frequency.

4.6 Conclusion

A new device, a porous plug electro-osmotic pump (pp-EOP) has been introduced. It has been realized by surface micromachining a porous polymer and

integrating it into parylene channels with embedded electrodes. The micromachined porous polymer plug created a high resistance to hydrostatic pressure driven flows permitting the construction of very compact pumping devices. This device is surface micromachined and can be fully batch fabricated. It has no moving parts, capability to generate precise nL/min flow rates and highly integratable, which make it a good choice for building fully integrated microfluidic systems.

The porous polymer was characterized by resistivity measurement and found to have a tortuosity/ porosity ratio of 3.3. Vertical electrodes consisting of 20 μm high, 10 μm wide pillars separated by 10 μm gap were used to establish a uniform electric field at the active area of the pump and to increase electrode surface area making the device more immune to bubble generation for the same current amplitude since bubble generation was proportional to current density. The electro-osmotic velocities of the devices were measured using 1 Hz symmetric voltage waveforms up to 4 volt magnitude. The Vertical electrode device was found to have a mobility of 1.14×10^{-9} $m^2/V.s$, 2.8 times greater than the planar ones. 3 V DC generated a 4.8 nL/min volumetric flow rate. This corresponded to a maximum pressure of 1540 Pa that could be generated with 3 volt DC. A new drive, low frequency zero averaged asymmetric current drive has been tried. Its experimental results have been presented. It has been seen that this drive produced net non-zero average voltage response. The net direction of the flow was determined by the duty cycle and the nonlinear behavior of the electrode interface. The vertical electrode device produced volumetric flow rates of $Q_{max} \approx 3.8$ nL/min. Even though this AC current drive technique allowed the use of voltages larger than 1.2 volts with suppressed bubble generation, electrodes got corroded and the device performance degraded and repeatability and reliability became an issue. Therefore other driving methods must be used with porous plug electro-osmotic pumps as will be shown in the next section.

SECTION 5

ENHANCED ELECTRO-OSMOTIC PUMPING WITH LIQUID BRIDGE AND FIELD EFFECT FLOW RECTIFICATION

5.1 Introduction

In the previous section, it was demonstrated that polymer plugs with sub-micron pores could suppress unwanted pressure-driven flow and allow electro-osmotic flow in a microchannel. Electro-osmotic pumps were fabricated driving EOF through these polymer plugs with average pore diameter of ≈300 nm inside parylene channels [Mut02]. In these devices electrode placement and biasing schemes played a critical role in the EOF velocity. These parameters must be used judiciously to maximize EOF while suppressing generation of electrolytic gas bubbles that obstruct flow. Bubble suppression was achieved using an asymmetric low frequency zero net charge current signal applied directly across the porous plug [Mut02]. In this scheme, unidirectional flow was achieved through Faradaic rectification [Vet67] of the corresponding time averaged plug voltage. Flow velocities of 14 μm/s were achieved with maximum velocities limited by the nonlinearity of the plug *IV* characteristic. However this driving scheme was found to have reliability and repeatability problems.

This section presents two separate concepts related to the electrode placement and biasing strategy that further abate generation of bubbles in the main flow. In the first concept the drive signal is applied to a main EOF porous plug through high flow resistance porous bridges present outside the main flow. In the second approach, metal

electrodes are located within the main channel across a series of dielectrically isolated narrow channels. Bubble generation is suppressed with a high-frequency square wave drive, and net unidirectional flow is achieved by modulation of the zeta potential on the narrow channel surfaces. Flow velocities of 10-66 μm/sec in 20 μm-high channels have been achieved by these two methods.

5.2 DC Drive Through Liquid Bridges

The detrimental effects of bubbles can be eliminated if bubbles are generated outside the main flow path. This can be achieved by placing electrodes outside the main flow channel as shown in Fig. 1. The electric field is then applied to the main central EOF porous plug through narrow liquid bridges. To be effective, these bridges must have low electrical resistance but high flow impedance. The use of gelatinous liquid bridges in EOF pumps has been discussed by Takamura [Tak03,Ala01]. Takamura used a long series of narrow necked channel regions to provide high resistance to pressure driven flow while achieving current conduction through a conductive gel that produced EOF. In our case, we use a short porous plug embedded in the main channel making this implementation compact and suitable for microfluidic chips that require multi pump configurations. Net pumping is generated through a difference in the effective electro-osmotic mobility between nanochannels of porous plugs and the main microchannel. As

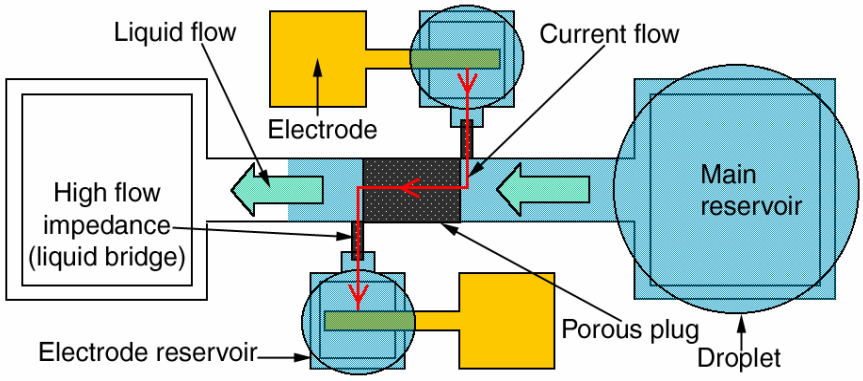

Fig. 5.1. Schematic of porous plug electro-osmotic pump (Pp-EOP) with liquid bridge connections.

discussed in Section 2, if the channel radius size becomes comparable to the double layer thickness, electro-osmotic mobility decreases. Since this happens in the pores of the porous polymer, electro-osmotic flow rate through the porous polymer will be less than the flow rate in the microchannel creating a net flow in the electrical field free regions of the microchannel. This way on-chip pumping can be achieved without exposing the biological or chemical samples to electric fields. This also enables the usage of electrochemical and conductivity detectors, which have been impaired by the high voltage fields in electrophoresis systems.

5.2.1 Advantage of Porous Polymer

The effect of using porous bridges is next examined. As explained in Section 2, porous structure can be modeled as a packing of parallel cylindrical channels with a radius *a*. The electrical resistance of the porous polymer with a liquid of resistivity, ρ_1 in its pores can be found to be:

$$R_{el} = \frac{\rho_1 L \tau}{\Psi A} \tag{1}$$

where τ is the tortuosity, Ψ is the porosity, *W* is the physical width and *A* is the physical cross-sectional area of the porous structure [Zen01].

Similarly, a hydraulic resistance can be defined for the liquid flow in micro domain since the Reynolds number is low and the liquid flow is laminar. The hydraulic resistance of the porous structure as given in Section 2 is:

$$R_{hyd} = \frac{8\eta L \tau}{a^2 \Psi A} \tag{2}$$

where η is the viscosity of the liquid and a is the radius of the pore. For this porous polymer a=150 nm, τ=2, Ψ=0.6. To evaluate the significance of having a porous polymer in the channel, the flow in a channel with a radius of 15μm is examined in the presence and absence of the porous plug. Having the plug increases the electrical resistance only 3.3 times. However, the hydraulic resistance increases 10,000 times, effectively blocking pressure driven flow. The hydraulic resistance of 50 μm long, 200 μm and 20 μm high porous polymer is 1.48×10^{16} Pa.s/m^3 whereas the same sized rectangular channel's is 4×10^{11} Pa.s/m^3. Therefore, in the analysis below, pressure driven flow through the porous polymer will be assumed to be zero.

5.2.2 Electro-Osmotically Induced Hydraulic Pumping

In section 2, it was mentioned that liquid velocity inside the microchannel can be thought of as a superimposition of a pressure and electro-osmotic driven flow. As explained in Section 2, electro-osmotic volume flow, Q_{EOF} can be shown to be:

$$Q_{EOF} = Mobility_{EOF} \cdot A \cdot E \tag{1}$$

$$Mobility_{EOF} = \mu_{EOF} = -\frac{\varepsilon\varepsilon_0\zeta}{\eta}\left[1 - \frac{2I_1(\kappa r)}{\kappa a I_0(\kappa a)}\right]$$

Electric field magnitude, E, in that expression can be expressed in terms of electrical current, I, flowing through the cross section of the microchannel and solution resistivity, ρ_{el}, as following:

$$E = \frac{V}{L} = \frac{IR_{el}}{L} = \frac{I\rho_{el}L}{LA} = \frac{I\rho_{el}}{A} \tag{2}$$

Then Q_{EOF} turns out to be:

$$Q_{EOF} = \mu_{EOF} \cdot \rho_{el} \cdot I \tag{3}$$

This means that the electro-osmotic volume flow is only proportional to the electro-osmotic flow mobility, solution resistivity and the electrical current magnitude. Therefore, in a homogenous network of microchannels, even though the cross-section or the length of the channel changes, as long as the same current flows through the microchannel, there can not be any hydraulic pressure driven flow induced by the electro-osmotic flow. However in non-homogenous systems, where different liquid resistivity, viscosity and electro-osmotic flow mobility can exist, electro-osmotically induced hydraulic pumping is possible in field free regions, where there is no current flow.

If liquids with different resistivity in contact with each other are used and current is applied across this non-homogenous system, in that system internal pressures will be generated at the nodes of the fluidic network that would drive pressure driven flows in field free regions where there is no electrical current flow [Chi02]. Similarly, the same net flow can be achieved if channels with different electro-osmotic mobility are used. Electro-osmotic mobility will be different for different zeta potential and different liquid viscosity. Zeta potential of a surface can be changed by coating or through field effect modification. In fact, zeta potential of a channel in a T intersection of three channels has been changed by coating the surface with surfactants to generate net flow in the field free region [Cul00]. Simulation results made on a T junction with electric potential applied to only two ports show that hydraulic flow can be generated in the third port (in the field free region) depending on the ratio of zeta potentials and the ratio of the widths of the two intersecting channels [Bia00].

Lastly, as mentioned previously, electro-osmotic mobility will be different for micro and nanochannels due to double layer overlap. The new pump with the liquid

bridge approach introduced in this section uses this mobility difference to generate pressure driven flow in field free regions of the microchannel as depicted in Fig. 2. In the field free regions, region 3, electro-osmotic flow is zero because there is no current flow in there. Current flows in regions 1, 2 and 4, creating electro-osmotic flow in these regions. However, since electro-osmotic mobility of region 1 and 2 is different, it creates a pressure in region 2 and this pressure creates the pressure flow, Q_{P3}, in region 3, in the field free region and in region 4 through the porous plug branch. However, since the hydraulic resistance of region 3 (main channel) is much less than the one in region 4 (porous plug), its pressure driven flow, Q_{P3} is much greater than Q_{P1}. Therefore Q_{P1} can be neglected compared to Q_{P3}. These can be expressed as following:

$$Q_{EO1} + Q_{P2} = Q_{EO1} + Q_{P1} + Q_{P3} \Rightarrow Q_{P2} = Q_{P1} + Q_{P3} \approx Q_{P3}$$

$$Q_{EO2} = Q_{EO1} + Q_{P1} + Q_{P3} \Rightarrow Q_{EO2} - Q_{EO1} = Q_{P1} + Q_{P3} \approx Q_{P3} \quad (4)$$

$$Q_{P3} = Q_{P2} = (\mu_{EOF2} - \mu_{EOF1}) \cdot \rho_{el} \cdot I \quad (5)$$

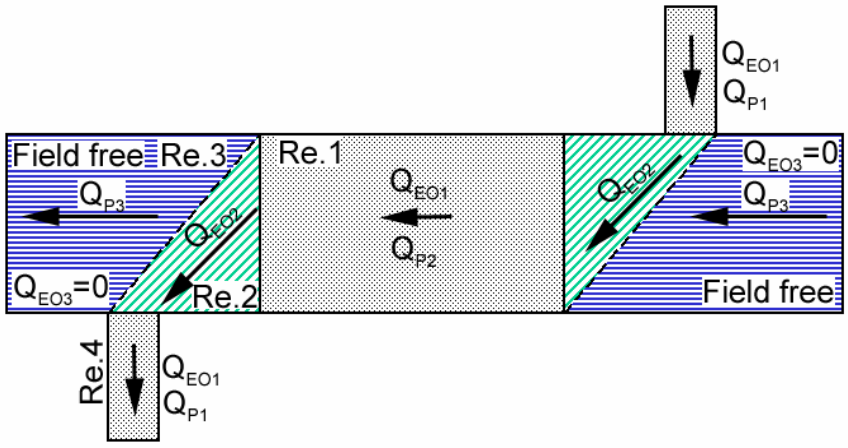

Fig. 5.2. Hydraulic pressure generation due to electro-osmotic mobility difference.

From the above expressions, it can be seen that the net flow in the field free region is directly proportional to the current magnitude, liquid resistivity and the mobility difference. If a liquid with higher ion concentration is used, current has to be increased in order to maintain the flow rate.

5.2.3 Fabrication and Test Results

Devices are fabricated with a four-mask surface micromachining process described in the previous section. Figure 3 shows a fabricated device. Devices are tested

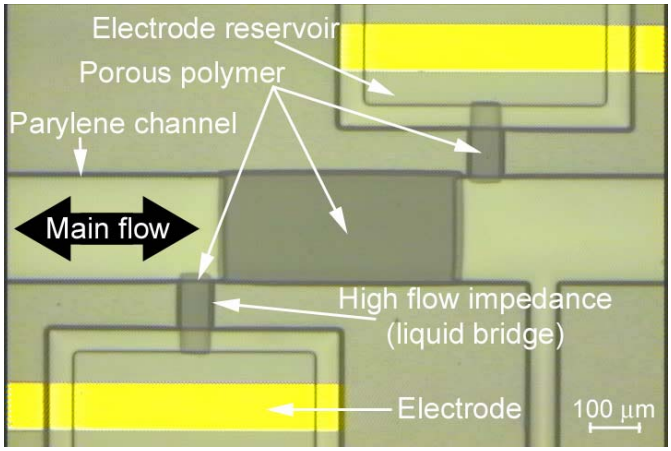

Fig. 5.3. Top view of fabricated Pp-EOP with liquid bridge.

with DI water in equilibrium with atmospheric carbon dioxide. Figure 4 shows the forward and reverse liquid flow in the main channel when a DC voltage is applied and reversed, respectively. Measured results of water-air interface velocities with different

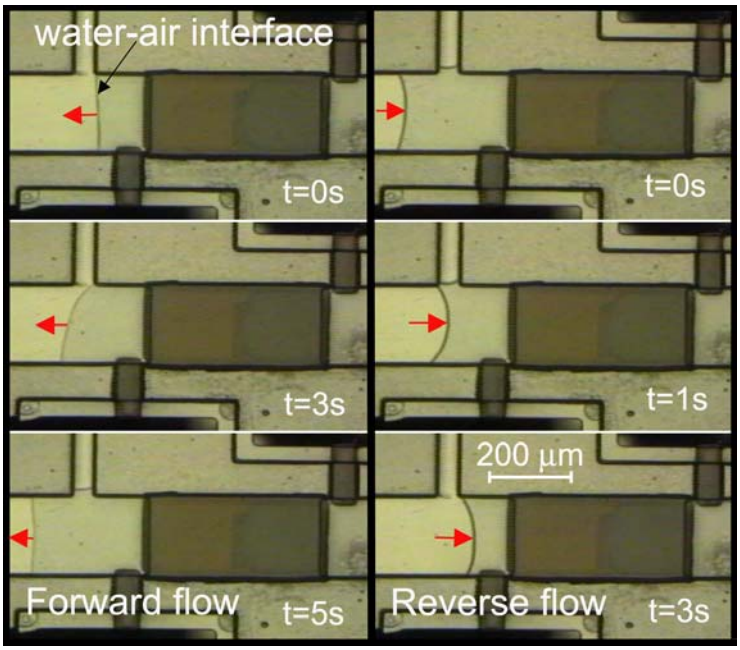

Fig. 5.4. Forward and reverse water-air interface movement with DC voltage applied and polarities reversed respectively.

DC voltage magnitudes are in Fig. 5. Velocity increases linearly with the applied voltage, therefore the current in the channel as expected from the above analysis. At 50 volt DC, volume flow rate is 1.76 nL/min. The hydraulic resistance of the device is the parallel combination of the main plug and one branch plug. This value is 5.7×10^{16} Pa.s/m^3. Then the maximum pressure this device can generate is 1673 Pa. A suitable figure of merit is the ratio of zero-flow pressure head per unit voltage per real estate area of the device. Takamura's device yields a figure of merit of 4.2×10^{-4} PaV^{-1} μm^{-2} while this device yields an estimated 3.7×10^{-4} PaV^{-1}μm^{-2}.

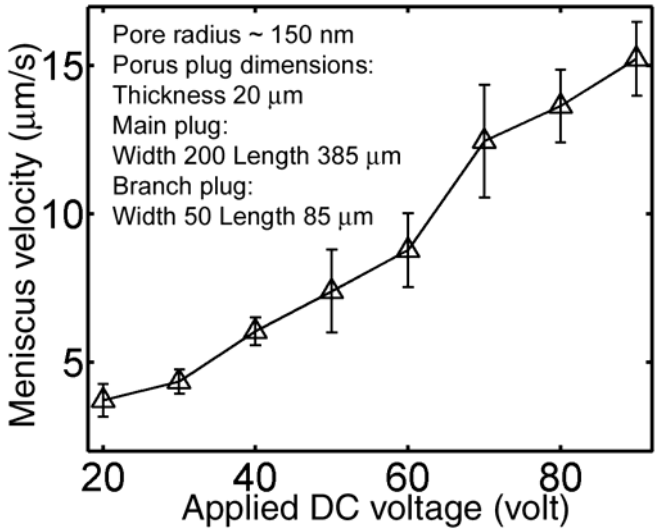

Fig. 5.5. Water-air interface velocity versus applied DC voltage.

Furthermore the flow through the porous polymer plug can be visualized by fluorescence detection of a neural marker, rhodamine b. Rhodamine b is a UV-detectable neutral marker in the solutions of pH in the range of 6 to 10.8 [Sch00] and is commonly used to visualize liquid flows. In this simple experiment, rhodamine b is dissolved in DI water and loaded into the upstream reservoir. The pump is started to pump in the downstream direction. A stereoscope (Olympus SZX12) capable of UV excitation with a 50 mW mercury lamp at 490 nm and detection above 500 nm is used to track neutral

markers. The result can be seen in Fig. 6. The markers are successfully pumped to the downstream of the main porous plug. This can be seen more clearly in Fig. 7. A high intensity of fluorescence can be seen in the main porous plug region. This shows some packing of the markers in the porous polymer. Also a considerably high fluorescence can be seen in the downstream porous plug branch. If the flow direction is reversed, the upstream porous branch also gets this high fluorescence intensity due to packing. This is because of the electro-osmotic flow through the porous plug branches.

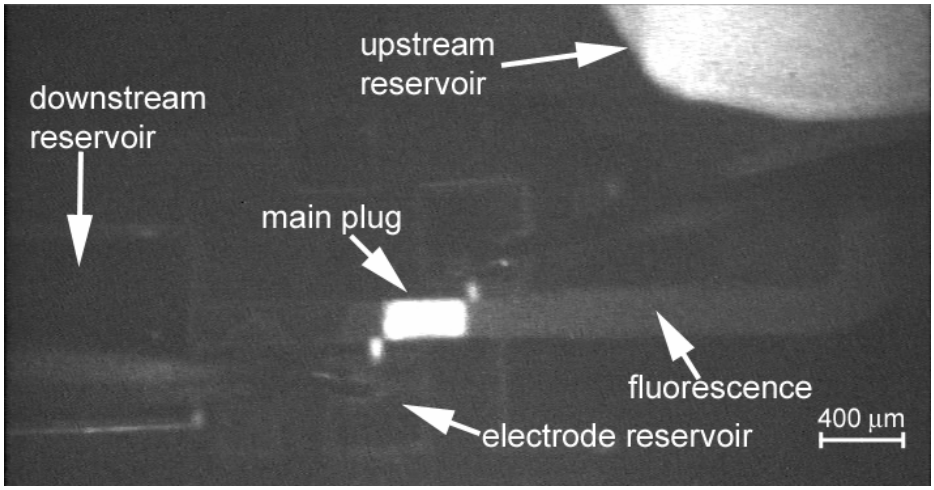

Fig. 5.6. Flow visualization with fluorescence detection of neutral markers, rhodamine b.

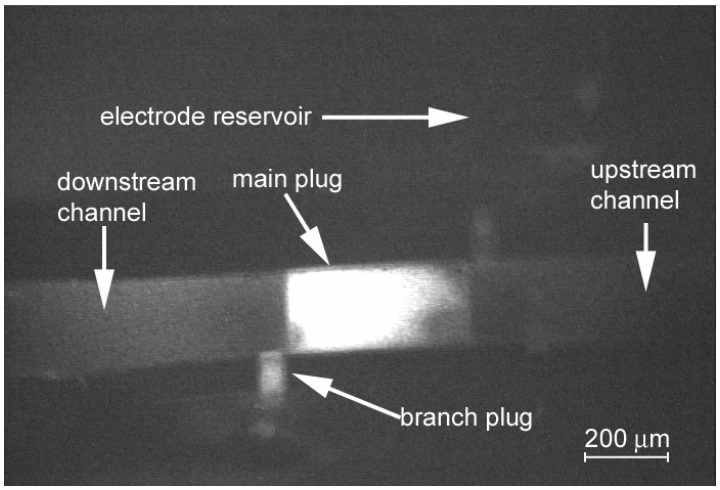

Fig. 5.7. Close up view of the porous plug region with neutral markers pumped in the downstream direction detected by their florescence.

5.3 AC Drive With Field Effect Rectification

The zeta potential of a fluid in a micro-channel can be altered by a bias applied to an insulated channel wall thereby permitting the direction of electro-osmotic flow to be reversed [Sch99]. We use this concept with a high aspect ratio, perforated metal gate electrode coated with an insulator, as a substitute for the porous plug in the electro-osmotic pump (Fig. 8). The gate electrode, is used synchronously with in-channel metal

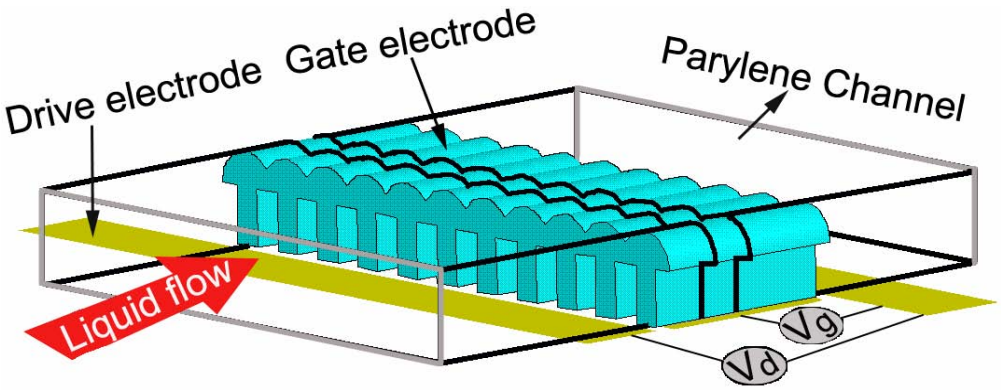

Fig. 5.8. Schematic of new flow field effect transistor (flowFET).

electrodes, up-stream and down-stream of it, to achieve unidirectional flow with bipolar AC pulses. Since the drive electrodes are inside the main channel, a high frequency zero averaged AC signal (V_d) is applied to prevent bubble generation. Without the gate electrode, this would result in net zero movement. However, if the negative of the AC signal is applied to the gate electrode (V_g) the zeta potential is synchronously modulated in the negative half-cycle, and the flow is rectified (Fig. 9). Other cases are summarized in Table 1. This resembles AC electro- osmosis where this kind of zeta potential modulation happens on a metal surface [Won03]. However, zeta potential modification through an insulated gate electrode is different from this. Details of ac electro-osmosis as defined in the literature and how it is different from this AC rectification scheme is discussed next.

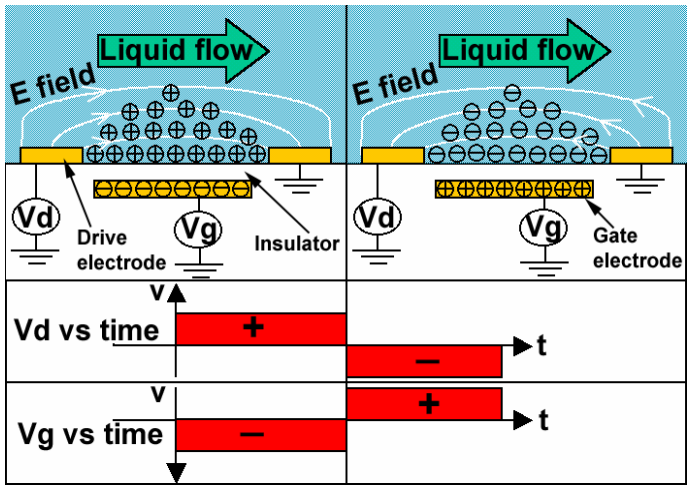

Fig. 5.9. Case showing affected charges, electric field and liquid flow direction when a periodic, net zero average waveform is applied to V_d and its negative to V_g. Net flow can be achieved as long as the *change* in the zeta potential is synchronous with V_d.

	Electric Field Direction	Affected Charges	Movement Direction	
Vd positive	+	+	+	Vg=-Vd
Vd negative	–	–	+	
Vd positive	+	–	–	Vg=Vd
Vd negative	–	+	–	
Vd positive	+	+	+	Vg floating
Vd negative	–	+	–	

Table 5.1. Different cases of a periodic net zero average waveform applied to driving voltage (V_d) and gate voltage (V_g).

5.3.1 AC Electro-Osmosis

Non-uniform AC electric fields generated by planar electrodes can produce net steady flow. As discussed in Section 4, electric field generated by the planar electrodes has both normal and tangential component. The tangential component is responsible for the electro-osmotic flow and the normal component is responsible for inducing charges in the diffuse double layers on electrode surfaces. Induced charges in the diffuse layer is opposite to the electrode charge. Even though these charges change with the AC field, tangential electric field direction changes too, leaving the liquid flow direction the same. This is depicted in Fig. 10a. The force due to tangential electric field on the induced

charges is directed from the center of the gap between electrodes onto the electrode surface producing a fluid flow pattern as shown in Fig. 10b. The fluid velocity decreases if traveled from the surface of the electrode to the top . It is maximum at the edge and it depends on the frequency and amplitude of the applied signal and on the conductivity of the electrolyte. The velocity goes to zero at high and low frequencies and becomes maximum at a specific frequency. This frequency is below 1 MHz and usually around 1 KHz [Gre02]. In that respect this is different from the AC flow rectification method introduced in this work. The gate electrode and the insulating layer does not require a non-uniform electric field like the one generated by the planar electrodes. In fact

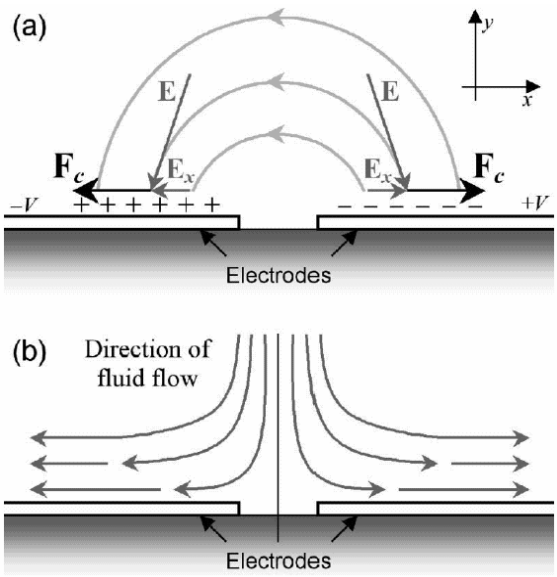

Fig. 5.10. Induced charges and the affecting force on them due to normal and tangential components of the electric field on planar electrodes respectively (a). The resulting flow pattern on planar electrodes (b) [Gre02].

a uniform electric field generated by the vertical driving electrodes would work better for the AC flowFET. Also the generated fluid flow pattern is uniform unlike the one for the AC electro-osmosis. Because of the insulating layer of the gate electrode, the flow is tangential to the surface just like the case for the DC electro-osmosis.

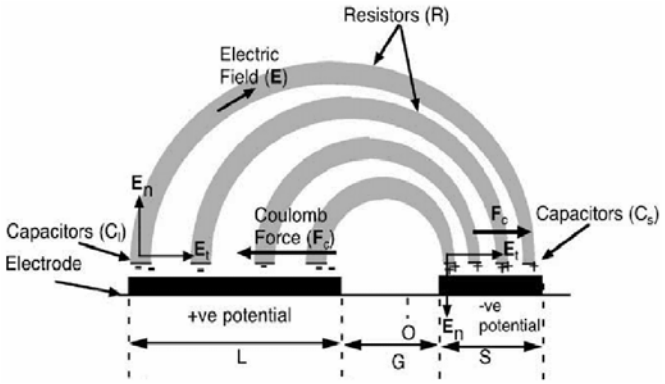

Fig. 5.11. Asymmetric electrodes to generate directional flow with AC electro-osmosis [Mph03].

In AC electro-osmosis, net liquid flow can be achieved by having asymmetric electrode geometry [Mph03,Stu02] as shown in Fig. 11. Because one electrode area is larger than the other, the induced flow on one electrode will be larger than the one on the smaller electrode hence generating a net flow in one direction. Furthermore, if interdigitated asymmetric electrodes were used on all surfaces of the channel walls, plug like flow can be achieved as was attempted in [Mph03] by having these electrodes both on top and the bottom of the channel. However AC flowFET does not require these interdigitated asymmetric electrodes.

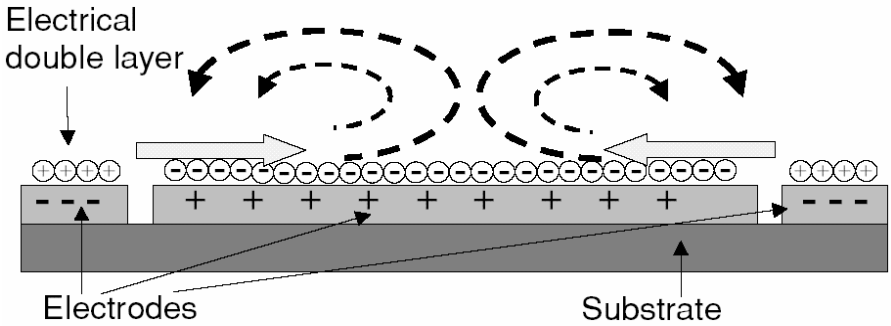

Fig. 5.12. Case showing affected charges, electric field and liquid flow on top of three electodes used for mixing liquids [Won03].

One of the main advantages of the AC electro-osmosis is its ability to create circular flow on planar electrode surfaces. This can be used for mixing as done in [Won03]. With a three-electrode configuration as shown in Fig. 12, mixing can be

achieved on top of the middle electrode. The middle electrode has opposite polarity of the other two electrodes on its right and left.

5.3.2 Time Scale of Electro-Osmotic Flow

One question that arises for this approach is if EOF can respond to alternating electric fields at high frequencies. When an electric field is applied to the liquid, its velocity at the capillary wall changes rapidly. Then the viscous forces accelerate the bulk of the liquid through the cross section of the capillary until it assumes a plug like flow at the same velocity as the slip velocity at the wall. The time necessary for the liquid to assume this slip velocity after the application of the electric field can be calculated from:

$$t_{char} = \frac{a^2 d}{5.8\eta} \tag{6}$$

where a is the radius of the channel and d is the density of the liquid [Dos93]. For a 5-μm channel radius, this value is 4.3 μs or 230 KHz.

5.3.3 Fabrication

The fabrication process starts with a silicon wafer with 2-μm thermal oxide as shown in Fig. 13. The device has a 20-μm high, 200-μm wide main channel. The gate electrode is formed by electroplating nickel through a 20-μm thick photoresist mold. The mold has 10 openings, 10-μm wide, 100-μm long, separated by 10-μm. The structure is over electroplated so that grown pillars will form mushroom structures forming closed channels [Joo95]. The final electro-plated structure looks like the drawing in Fig. 9,

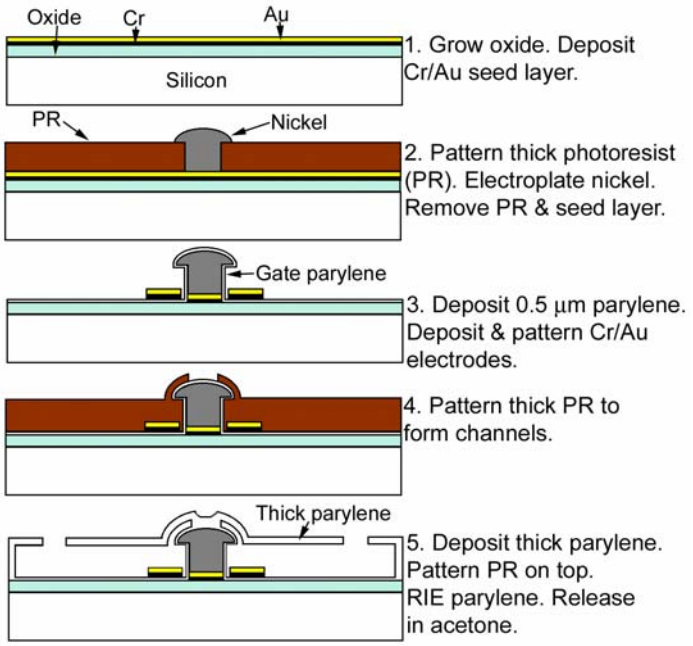

Fig. 5.13. Fabrication process for the flowFET.

forming 20-μm high, 10-μm wide 10 parallel channels. Then structure is coated with 0.5-μm thick parylene. Since parylene deposition is conformal, it can coat the inner surfaces of the closed gate structure. Figure 14 shows a fabricated device.

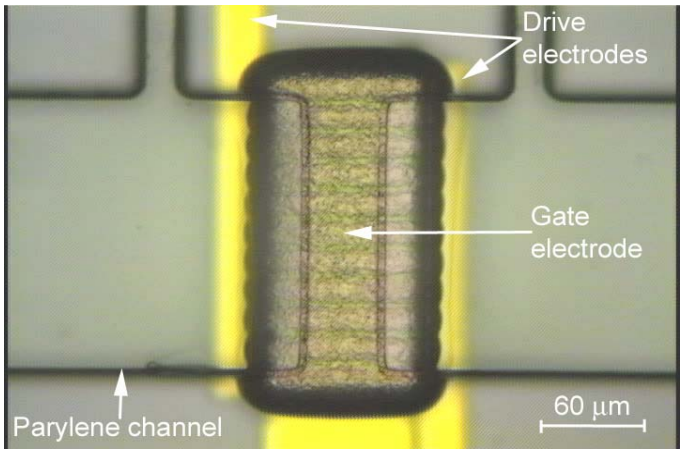

Fig. 5.14. Top view of a fabricated new flowFET.

5.3.4 Net Electro-Osmotic Velocity After Rectification

The net zeta potential after an AC signal is applied to the gate electrode can be thought of as superimposition of two components: natural zeta potential, ζ_{nat}, that would

exist at the interface if no gate voltage is applied and zeta potential change, $\Delta\zeta$, due to applied voltage.

$$\zeta_{net} = \zeta_{nat} + \Delta\zeta \tag{7}$$

For this channel dimensions the Helmholtz-Smoluchowski equation can be used to calculate EOF velocity, which is proportional to the zeta potential and the applied electric field.

$$\upsilon_{eof} = \frac{\varepsilon\varepsilon_0}{\eta}\frac{V_d}{L}(\zeta_{nat} + \Delta\zeta) \tag{8}$$

where V_d is the drive voltage, L the channel length, ε the dielectric constant of the medium and ε_0 the permittivity of free space.

Similarly net EOF velocity has two components: velocity due to natural zeta potential, ν_{nat} and velocity due to zeta potential change, $\Delta\nu$.

$$\nu_{net} = \nu_{nat} + \Delta\nu \tag{9}$$

From the above equation, it is clear that:

$$\upsilon_{nat} = \frac{\varepsilon\varepsilon_0}{\eta}\frac{V_d}{L}\zeta_{nat} \qquad \Delta\upsilon = \frac{\varepsilon\varepsilon_0}{\eta}\frac{V_d}{L}\Delta\zeta \tag{10}$$

If a sine wave is applied with a modulation frequency of ω to drive electrodes then the net EOF velocity can be found by averaging velocity components over a period:

$$\upsilon_{net} = \frac{1}{T}\int_0^T \frac{\varepsilon\varepsilon_0}{\eta}\frac{|V_d|}{L}\zeta_{nat}\sin(\omega\cdot t)dt + \frac{1}{T}\int_0^T \frac{\varepsilon\varepsilon_0}{\eta}\frac{|V_d|}{L}\Delta\zeta\sin(\omega\cdot t)dt \qquad (11)$$

In the first term in the above equation all the terms are constants except for the sine wave. Then this integration turns into integration of a sine wave over one period, which is zero. This is expected since this velocity component is due to natural zeta potential and if a symmetric AC electric field is applied, the net velocity becomes zero. However the second term is not equal to zero because we have a non-constant $\Delta\zeta$ term. This term is modeled next.

5.3.4.1 Zeta Potential Change due to Gate Potential

Gate electrode/insulator/electrolyte interface is depicted in Fig. 15. Double layer forms between the insulator and the electrolyte whose potential profile changes by the gate voltage applied to the metal gate electrode. This model assumes that the zeta potential is the potential at the intermediate node of a capacitive potential divider formed by the series combination of C_{wall}, the capacitance due to the insulating coating, C_H, the capacitance due to compact layer of the double layer and C_D, the capacitance due to diffuse layer of the double layer of the interface [Sch99] as shown in Fig. 16. Since

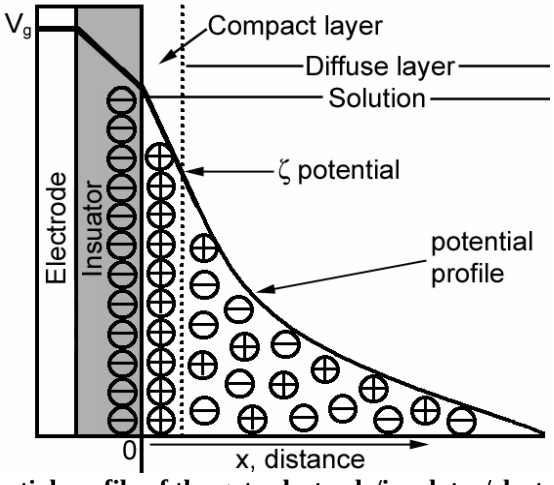

Fig. 5.15. Potential profile of the gate electrode/insulator/electrolyte interface.

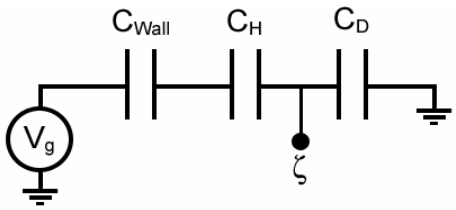

Fig. 5.16. Equivalent circuit model of the metal electrode/insulator/electrolyte interface.

compact layer's thickness is around 5 A°, C_H value is very big, so it can be neglected. Then this is just a capacitive potential divider between C_D and C_{Wall}. Furthermore C_D value is greater than C_{Wall} because the thickness of the diffuse layer of the double layer (maximum around 0.1 μm for DI water with dielectric constant of 80 and gets thinner with the increase of the ion concentration of the electrolyte) is negligible compared to the insulator thickness (0.5 μm with dielectic constant of 2.9) used here. Then a simple approximation to the effect of gate bias on zeta potential change, $\Delta\zeta$, under sinusoidal AC modulation with a frequency of ω is

$$\Delta\zeta = \frac{C_{Wall}}{C_D}\left|V_g\right|\sin(\omega.t) \tag{12}$$

This is just an approximation to the zeta potential change. Because if looked at the C_D expression of the Gouy-Chapman model as explained in Section 2, this value also depends on the zeta potential. A more complete model can be found in [Ki00]. However this simple model is important to see fundamentals of field effect rectification. Assuming that the channel contains DI water with ion concentration of 7.5 μM and natural zeta potential of 30 mV, $\left|\Delta\zeta\right|$ is 72 mV for a V_g magnitude of 10 V, which is enough to reverse the polarity of the zeta potential. However, reversing the zeta potential sign is not required to get net forward or reverse movement as will be explained next. If zeta potential sign can be reversed, the flow would be always in the same direction in both negative and positive cycles of the applied driving voltage. Therefore the flow would be

more like a continuous flow. If zeta potential sign can not be changed, this can happen in different pH and ion concentration values of electrolytes, this would still generate net flow in forward or reverse as desired but the flow would be pulsatile. The flow would be in the positive direction in the positive drive signal cycle and be in the negative direction in the negative cycle. However as long as a change can be induced in the zeta potential value, there would be a net flow as discussed next.

5.3.4.2 Electro-Osmotic Velocity Change due to Zeta Potential Change

Since expression for $\Delta\zeta$ is now derived, net EOF velocity can be calculated. Assuming the gate voltage has the same modulation frequency with the drive voltage,

$$\upsilon_{net} = \frac{1}{T}\frac{\varepsilon\varepsilon_0}{\eta}\frac{|V_d|}{L}|V_g|\frac{C_{Wall}}{C_D}\int_0^T \sin^2(\omega \cdot t)dt \tag{13}$$

Since this velocity equation has the square of a sine function, it has net value even though the electric field changes periodically. However, as mentioned before EOF velocity due to the natural zeta potential produces net zero velocity over one period. Furthermore reverse net movement can be easily achieved by applying a voltage signal to the gate that is 180° out of phase of the driving voltage. After this analysis, fabricated devices are tested to see if these derivations are correct.

5.3.5 Test Resuts

For experimental verification, a 1 KHz square wave is applied to drive electrodes and bead velocities are measured for three cases: the gate voltage floating, equal to V_d, and equal to $-V_d$, which resulted in no movement, forward and reverse movement of 1-μm latex microbeads, respectively, with bead velocities of up to 66 μm/s as expected from the above analysis.

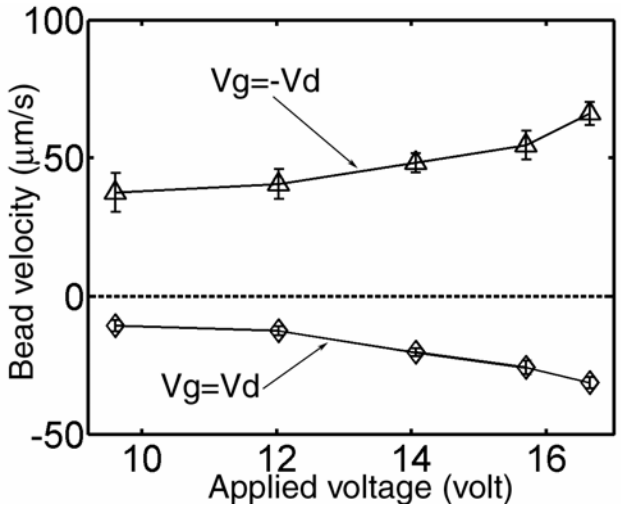

Fig. 5.17. Bead velocity vs. magnitude of V_d of a 1 KHz square wave, with V_g equals to V_d and $-V_d$.

Measurements are done in field-free regions after equalizing the pressures on both sides of the pump since with these channel dimensions pressure-driven flow can become dominant. The test results in Fig. 17 demonstrate the effectiveness of this concept. As predicted in the previous section, when the gate electrode is floating, the net velocity is due to only natural ζ potential and it is zero. When the same potential applied to the drive electrodes is applied to the gate electrode, forward flow is achieved and this is proportional to the square of the magnitude of the applied signal. This quadratic relation can be seen in Fig. 17. When negative of the drive signal is applied to the gate electrode (180° phase difference), reverse net flow is achieved again with a quadratic relationship with the applied signal magnitude. However reverse velocities are slower than the forward ones. That is because when the negative of the drive voltage is applied to the gate electrode, the potential difference across the electrolyte and the gate electrode is larger than when the gate voltage is the same as the drive voltage. This larger voltage difference creates larger zeta potential change therefore larger flow rates.

Zero-flow pressure head can be estimated from the maximum flow rate measurements (Fig. 17), which is the flow rate when the flow faces zero pressure. The

relationship is $P_{max}=Q_{max}.R_{hyd}$. R_{hyd} of 10 parallel narrow channels is $8.75x10^{12}$ Pa.s/m^3. With a signal magnitude of 16.6 volts, P_{max} =2.3 Pa. This low value is expected because of large dimensions of narrow channels. Instead of 10 μm wide parallel channels, if 1 μm wide ones is used, this will constitute 100 parallel channels in the same chip area and their hydraulic resistance will be $6.2x10^{14}$ Pa.s/m^3 corresponding to a maximum pressure of 163 Pa that can be generated. This can be further improved by making narrow channel width or height less than 1μm or by having a insulated metallic porous structure.

5.4 Conclusion

This section has demonstrated two alternatives for electrode placement and bias control for electro-osmotic pumping. The first one was to use a liquid bridge connection to the main channel through a porous polymer. This connection allowed an external current to drive flow inside the main channel, but largely blocked undesired mass flow. In this manner, DC voltage could be applied without causing any bubble generation in the main channel. At 50 V DC, flow rate was 1.76 nL/min. The second option was to rectify AC driven electro-osmotic flow by changing the zeta potential of all surfaces that produced EOF by a high aspect-ratio perforated gate electrode covered with a thin insulator. Experiments verified that with a square wave of 16.6 V magnitude at 1 KHz applied to driving electrodes, latex microbeads had forward velocity of 66 μm/s when the gate voltage was the negative of the driving voltage.

SECTION 6

THERMALLY RESPONSIVE POLYMER VALVE

6.1 Introduction

In the previous sections, the focus was on micropumps, specifically electro-osmotic pumps, for the integrated microfluidic systems since the transport of a liquid from one part of the system to the other is the most basic task. However, in addition to a micropump, integrated microfluidic systems need microvalves to separate liquids physically, direct liquid flow or seal reaction or PCR chambers where there will be heating. Most mechanical valves actuate a diaphragm to close or open a channel. This complicates the fabrication process and makes large-scale integration difficult. Due to these complexities, alternative inline valves that can provide a better seal have been fabricated using working substances such as hydrogel materials. Hydrogels undergo reversible volume change (swelling) inside the liquid, which they are immersed in response to different stimuli like pH, temperature and ion concentration thus plugging the microchannel. Presently hydrogel materials are patterned by selective deposition or in-situ polymerization on (or between) pre-fabricated surfaces. In this work, a thermally responsive hydrogel is surface micromachined in a very similar way to a photolithography of a photoresist.

This section introduces a thermally responsive polymer valve fabricated from a photoresist like thermally responsive polymer. Thin film process of this thermally responsive polymer is discussed. This is followed by test results of patterned polymer's

volume change inside water at different temperatures. The valve fabrication is then achieved by integrating the polymer plug to parylene microchannels with embedded microheaters and backside etched holes. Test results of this valve are presented.

In addition to this, microvalves have been fabricated in mesoscale by in-situ polymerization of thermally responsive polymers inside glass capillaries to characterize their valving properties more easily and to try other thermally responsive polymers with higher critical temperatures. The first mesoscale valve uses a thermally responsive polymer with almost the same chemistry as the photoresist like thermally responsive polymer. Chemistry of the polymers and test results of the valves are given. The second mesoscale valve introduces new class of thermally responsive polymers with adjustable critical solution temperatures. Test results and methods to change critical solution temperatures of these polymers are given.

6.2 Chemistry of Thermally Responsive Polymer

Thermally responsive polymer (poly (N-isopropyl acrylamide-co-allyl methacrylate)) used in this valve is formed by copolymerizing N-isopropylacrylamide (NIPAAm) with allyl methacrylate and crosslinked to a photo initiator (Azobisisobutyronitrile) inside a strong solvent, tetrahydrofuran (THF), solution as shown in Fig. 1. A copolymer is needed so that poly NIPAAm can be crosslinked to the photo-initiator and have photoresist like film property. NIPAAm is one of the best-known materials in class of temperature sensitive polymers. Its lower critical solution temperature (LCST) is 32 °C. It undergoes a rapid and reversible phase transition from extended hydrated chains (swollen state) below that temperature to collapsed hydrophobic coils (shrunk state) above it. Photo-patterning of a different polyNIPAAm copolymer and photo-initiator was reported previously [Hof99].

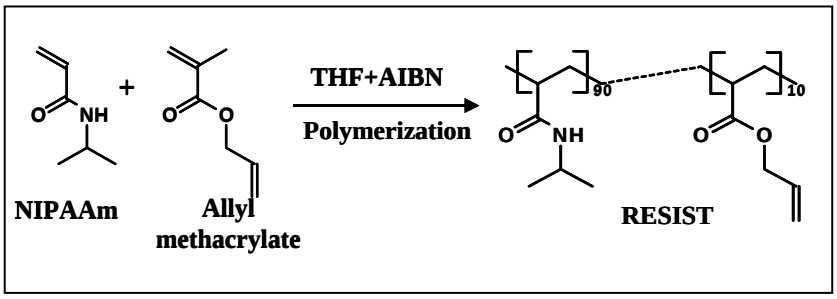

Fig. 6.1. Preparation of resist like thermally responsive polymer.

6.3 Thin film formation

It is found that the best way for thin film formation of this polymer is by spin coating the solution of thermally responsive polymer prepared using above method dissolved inside THF with a 2,2-dimethoxy-2-phenylacetophenone (DPAP, UV initiator). However since the viscosity of the polymer solution is very low, spinning at 300-500 rpm range gives film thickness of around 0.5 to 1 μm. This was for 90 mg polymer, 2 mg DPAP and 1 ml THF. In order to achieve desired thickness, viscosity of the solution has been increased by dissolving more polymer in THF. For example, 500 mg polymer, 20 mg DPAP and 2 ml THF solution spun at 500 rpm gave very good uniform film thickness of around 5 μm. However, spinning was abandoned since preparing large amount of polymer was not feasible and spinning consumed a large quantity of the polymer. Therefore, a casting method is used. The fixture used for this method is shown in Fig. 2. Process wafer is put between two aluminum plates. An O-ring on top of the wafer and tightened screws around the top plates secures the wafer and prevents any liquid leak. Polymer in THF solution is poured on top of the wafer through the opening of top aluminum plate. It is softbaked for 10 minutes at 60 °C. This forms a good uniform film. However at the edges thicker film is formed due to edge effects of the aluminum plate and also uniformity of the film depends on the level of the surface the aluminum plates stood on. Thicker film around wafer edge is removed by circling acetone-dipped scrub by

Fig. 6.2. Fixture for the casting method.

With this method thicker films can be achievable.

The Polymer film's adhesion to silicon and silicon oxide is achieved by immersing them into 7:3 acetone:A174 silane solution for a day. Patterning of the polymer is done by contact lithography. It is exposed through a mask for 15 minutes using EV-420 aligner with a UV light power density of 10 mW/cm². Exposed film is developed in acetone for 5 minutes. Resulting pattern and its response to different temperature can be seen in Fig. 3.

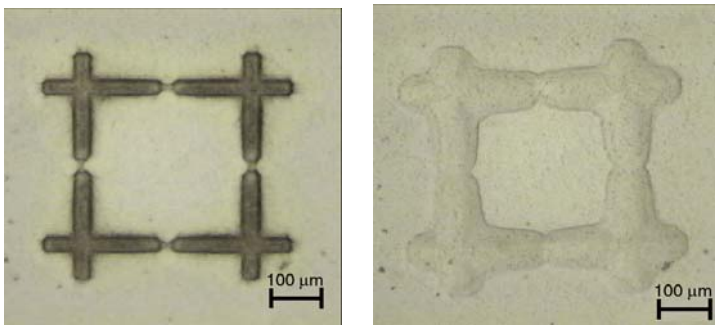

Fig. 6.3. (Left) Top view of UV patterned polymer in 40 °C water. (Right) Same pattern in 15 °C water.

6.4 Volume change characterization

Before using this polymer as a valve, patterned polymer structures are needed to be characterized for its size change at different temperatures of aqueous solution. In order

to make these measurements, cross sectional views of polymer patterns in DI water at different temperatures are taken using a CCD camera that is attached to a microscope.

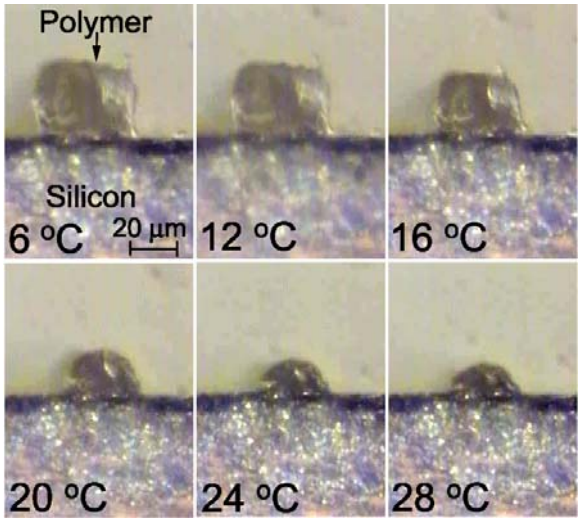

Fig. 6.4. Cross sectional view of patterned polymer inside DI water at different temperatures.

Some of the pictures from these measurements are shown in Fig. 4. Results from these measurements are shown in Fig. 5. This shows a 2.5 fold increase in film thickness with water's temperature change from 28 °C to 5°C. This points out that volume change of the patterned polymer structures happens over a temperature range. In this case, most of volume change happens between 10 and 25 °C. This deviates from an ideal behavior of poly-NIPAAm undergoing a rapid phase transition just below and above aqueous

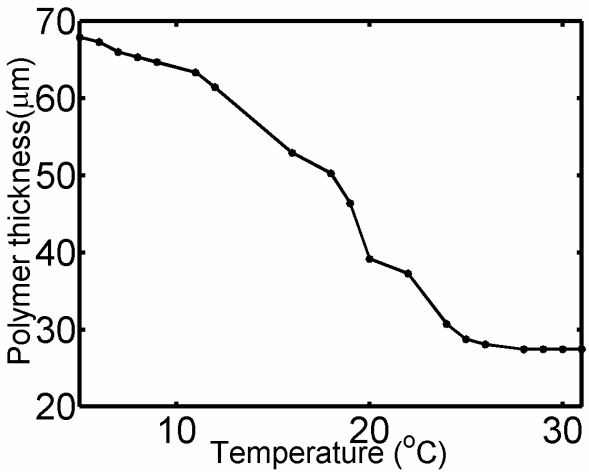

Fig. 6.5. Polymer's thickness change in DI water at different temperatures.

solution temperature of 32 °C. Other copolymer must be used in order to move the LCST of the polymer to higher temperatures or surface micromachining of pure poly-NIPAAm can be tried. Furthermore same samples show 3.4 fold increase in acetone and 4.2 fold increase in Isopropyl Alcohol (IPA) in film thickness independent of their temperatures. This later on caused release problems of devices in acetone and IPA.

6.5 Device fabrication

Thermally sensitive polymer valve is surface micromachined with backside-etched holes. Fabrication starts with growing 2-μm oxide on silicon wafer. Ti/Pt/Ti (300/1000/300 A°) is evaporated and patterned as microheaters. 0.5-μm parylene is deposited and patterned on top so that it covers only heaters for their electrical insulation. Then polymer film is patterned as explained above. Sacrificial 20-μm thick photoresist is patterned to form channels and reservoirs. 6-μm parylene is deposited to form channel

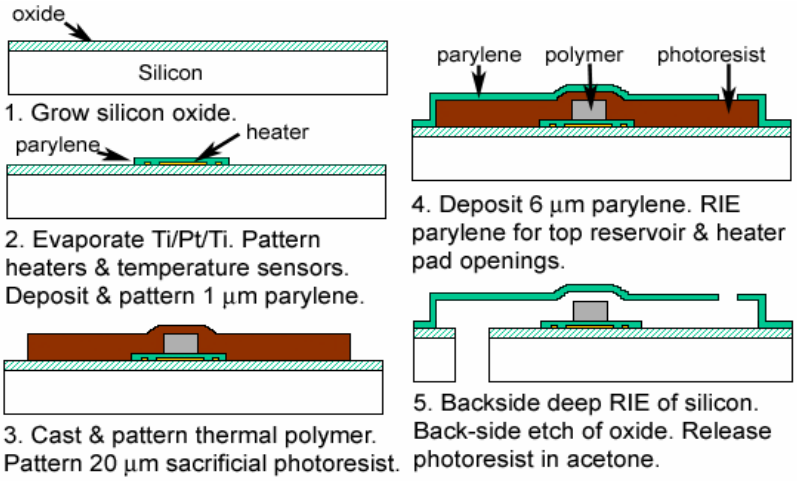

Fig. 6.6. Process flow for the photoresist like thermally responsive valve.

walls. Parylene on the backside is removed in oxygen plasma and backside alignment is done to pattern backside holes. Holes are etched with deep-RIE. Etching stopped at the oxide film. Thick photoresist is patterned on the front side for top reservoir openings and heater pads. Parylene is etched in oxygen plasma. Backside oxide film is etched in buffered HF. Finally devices are released in acetone. Process flow is shown in Fig. 6.

The acetone release of the sacrificial photoresist is very critical since poly NIPAAm copolymer swells in acetone and hinders complete removal of the photoresist. However, once acetone evaporates, the polymer shrinks almost to its patterned size. It is

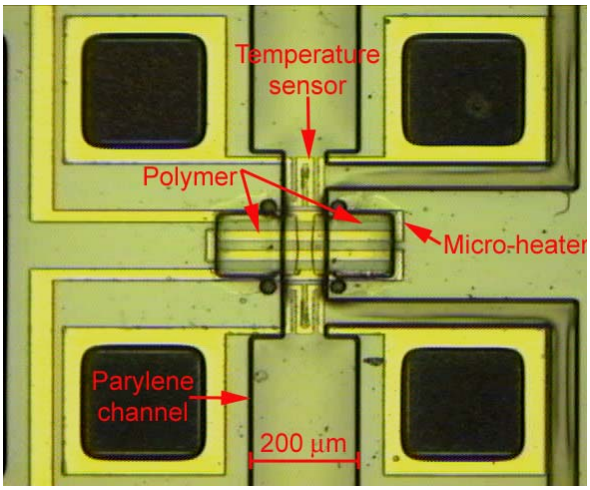

Fig. 6.7. Top view of a released valve

found that after a day-long acetone soak, two repeated 5 min acetone soaks followed by 5 min. dry periods, result in well released devices. A picture of the released device is shown in Fig. 7.

In order to enhance photoresist release around the polymers, a design with two polymer plugs with a lateral gap between them is chosen. Since response time of this polymer depends on the collective diffusion of the polymer network into the surrounding medium, a larger surface area of the polymer exposed to liquid decreases the response time [Liu02]. Further decreases can be achieved by fabricating smaller rectangular patterns in parallel instead of one large feature.

One major problem in releasing devices is, what we believe, very hydrophobic nature of the polymer in the dry state. This is apparent from polymer's showing no response to water temperature change after thorough DI water rinsing. Polymer swells only with IPA, acetone or strong bases like NaOH and KOH. So the devices are released by soaking the devices first into IPA after they have been acetone released and dried.

After IPA, soaking the devices into cold DI water (4 °C) for couple hours rinses IPA inside polymer. IPA is replaced by cold water since at temperatures below critical solution temperature, water gets incorporated into the polymer making it swell and IPA diffuses out into the water. After this release the polymer starts changing volume with water temperature. This kind of release can also be made with strong bases like KOH or NaOH since the polymer swells in these strong bases too. Therefore after acetone release, putting the devices into these strong bases for short time like 5 minutes and then soaking them into DI water also releases the polymer well. Recent devices are released this way. Dilute NaOH solution is flowed inside the channel followed by DI water. Tests are made after that. After releasing the polymer, it must not be let to dry afterwards since it will be very hydrophobic again and needs to be primed again with IPA or NaOH. Therefore a system employing these valves must be released this way and must be packaged with the liquid inside the channels. This would prevent any priming problems and make the system more reliable.

6.6 Test Results

The valve is tested using an aluminum fixture as shown in Fig. 8 to pressure liquid into microchannels through backside etched holes of the valve. The fixture have

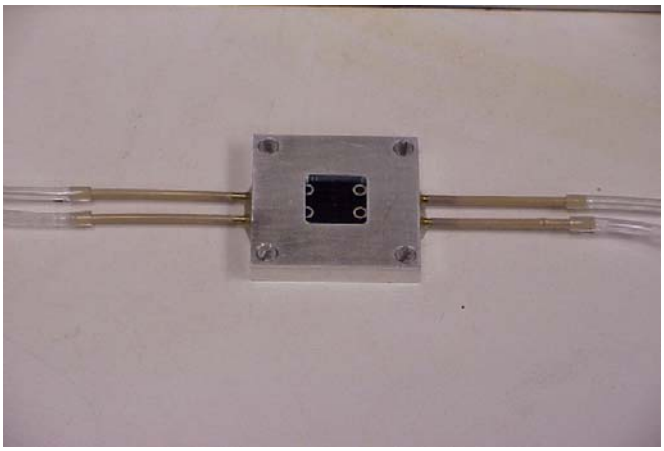

Fig. 6.8. Fixture used to test the polymer valve.

two pieces: one main piece where the device sits and a cover with a window at the center for electrical connections and visual inspection that clamps the device tightly to this piece. The main piece have drilled channels in the aluminum body that goes horizontally from the attached external tubing towards the center of the piece and then goes vertically upward reaching the surface. From top, these seem as holes on the fixture surface. However, they are connected to external tubing on the sides of the fixture. The valve's backside holes sit on O-rings where they are aligned with the holes on the fixture surface. And the second piece clamps the valve, O-ring and the first aluminum piece together tightly preventing any leakage.

The overall test setup is shown in Fig. 9. This figure also shows the cross section of the aluminum fixture. A syringe pump is used to flow liquid into the channel with a constant flow rate. The pressure inside the channel is measured with an external pressure sensor connected between the fixture tubing and the syringe pump. The fixture sits on a cold chuck that has a constant temperature of 15 °C. Heaters are connected to a power supply. First the valve operation is confirmed visually. When the heater is off, since the device temperature is at 15 °C below LCST of the polymer, it is swollen and the valve is closed. As soon as the heater is turned on, the polymer shrinks in about 1 second

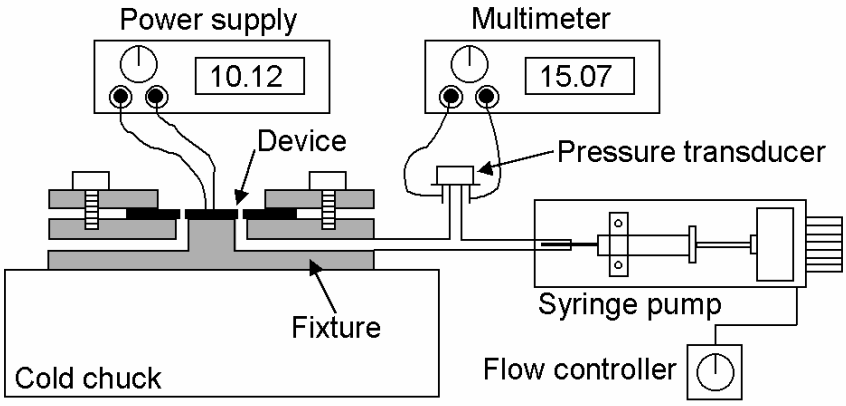

Fig. 6.9. Test setup to measure build-up pressure in front of the polymer.

opening the valve. Once the heater turned off, the temperature drops and the polymer swells in about 2 seconds closing the valve. This is shown in Fig. 10.

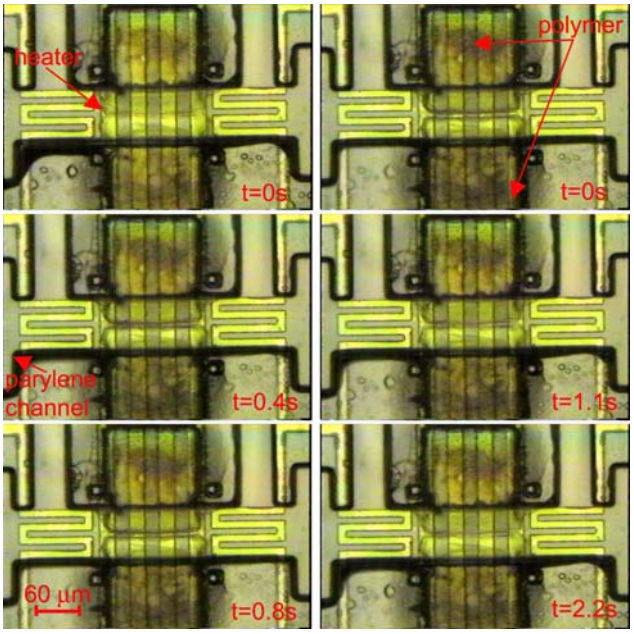

Fig. 6.10. Top view of swollen polymer inside parylene channel shrinking with time as heater turned on (left column) and shrunk polymer swelling as the heater turned off (right column).

After swelling and shrinking of the polymer is confirmed around 50 cycles, pressure readings are made with syringe pump's constant flow rate of 1 µm/min. At first the heater is on, the valve is open. The pressure reading from the external pressure sensor is around 13 psi. As soon as the heater is turned of, the pressure starts to increase with time linearly since this closes the valve. Because now the channel is closed, the pressure increases linearly with time since a constant flow rate is applied as expected. Test result is shown in Fig. 11. After 24 psi, the pressure suddenly drops because the parylene channel bursts.

So far, only this thermally sensitive polymer has been micromachined. Although this valve affords the desired rapid actions, the phase transition temperature of 32 ^{o}C may not be suitable for some applications such as PCR for which a higher temperature is required. Therefore, other polymers with higher critical temperatures can be formed using

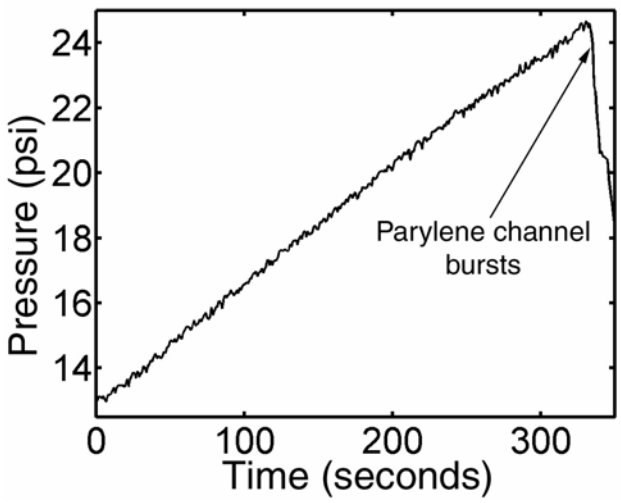

Fig 6.11. Pressure increase just after the valve is closed with a constant flow rate of 1 μm/min applied.

poly(N-ethylacrylamide) (EAm) that has a phase transition temperature of 74 ^{o}C, which is much higher than that for polyNIPAAm. This provides a technical advantage since no cooling device is required to achieve closing while a resistance heater put underneath the polymer can easily afford the heating. In addition, copolymerization of EAm with NIPAAm enables fine-tuning of the transition temperature and creation of valves operating at predetermined temperatures ranging from 32 ^{o}C to 74 ^{o}C [Luo03]. This will be demonstrated next. However before that, a thermally responsive valve very similar to this photoresist like thermally responsive polymer that has been fabricated in mesoscale by in-situ polymerization inside glass capillaries will be introduced. Their test results form the basics to test and characterize these kinds of polymers including thermally responsive polymer valves with adjustable critical temperatures that will be introduced after.

6.7 Mesoscale Thermally Responsive Monolithic Valves

The monolithic polyNIPAAm copolymer is also prepared using a UV initiated in-situ polymerization technique. In the preliminary experiment, the channel is filled with the polymerization mixture and irradiated through a mask to afford 2 mm long valve at

the specific location within the channel of a microfluidic chip. A single step in situ co-polymerization of a mixture consisting of N-isopropyl acrylamide (functional monomer), ethylene dimethacrylate (crosslinker), tetrahydrofuran and hexane (porogens), and azobisisobutyronitrile (free radical initiator) affords a macroporous monolithic material. The preliminary results achieved using a capillary as a model of a microfluidic channel indicate that this valve fits the requirements. Table 1 shows the flow resistance of the valve for water at different flow rates. Clearly, the flow resistance measured as the backpressure in the system vastly differs depending on temperature at which the measurement is carried out. As predicted, the pressure is much higher at a temperature below the LCST of the polymer, which is close to 32 °C.

Flow rate	Pressure, psi	
μL/min	20 °C	45 °C
2	0	74.5
10	5.5	111
50	22	307.5
100	37.5	∞ [a)]

[a)] The pressure in system exceeds limit tolerated by the equipment

Table 6.1. Flow resistance of a monolithic valve located in a capillary at different flow rates.

Then the thermal response of this valve is studied. The result is shown in Fig. 12. Using water at a flow rate of 10 μL/min, the backpressure of about 65 psi is monitored for the chip kept at a room temperature while a rapid decrease in the pressure is observed after increasing the temperature to 42 °C. A pressure drop to about 50% is achieved in 10 s and to 70% in 20 s.

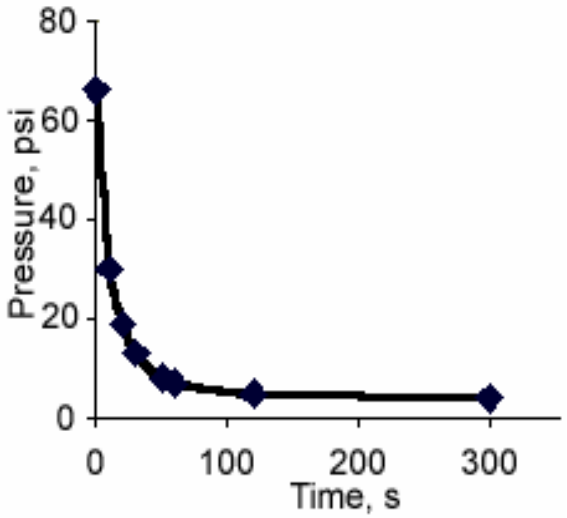

Fig. 6.12. Changes in the back pressure in the microfluidic channel containing 2 mm long macroporous NIPAAm-EDMA monolith. The microchip was submerged at time 0 in 42^0C bath.

After optimization of the procedure, the performance of the valve improved vastly. For example, a pressure of 210 psi is monitored at a flow rate of 1 μL/min and room temperature thus demonstrating better function in the "close" position. A very rapid decrease in pressure is observed after immersing the microchip in a water bath kept at a temperature of 42 °C. The pressure drops to 9 psi at 10 s, and to 4 psi in 20 s.

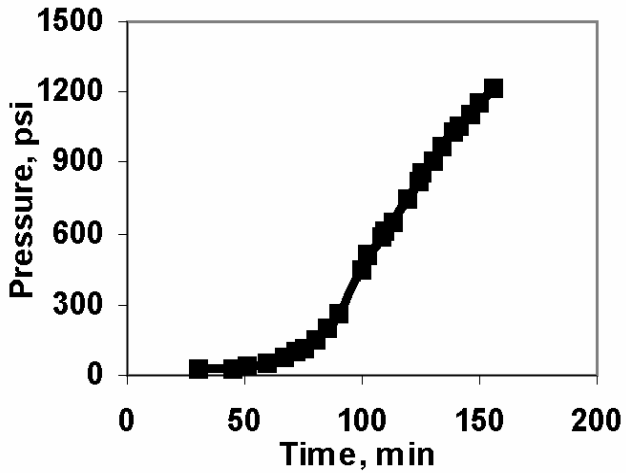

Fig. 6.13. Building of pressure in the channel containing monolithic valve.

This monolith is also characterized by an excellent mechanical stability within the channel. Figure 13 shows pressure build up in the channel after switching on the pump.

This measurement is carried out with the monolithic valve in the close position at a temperature of 20 ^{o}C using a flow rate set to 10 μL/min. The polymer is prepared in the presence of a higher percentage of tetrahydrofuran. No structural changes or displacement are observed even at a pressure of 1200 psi.

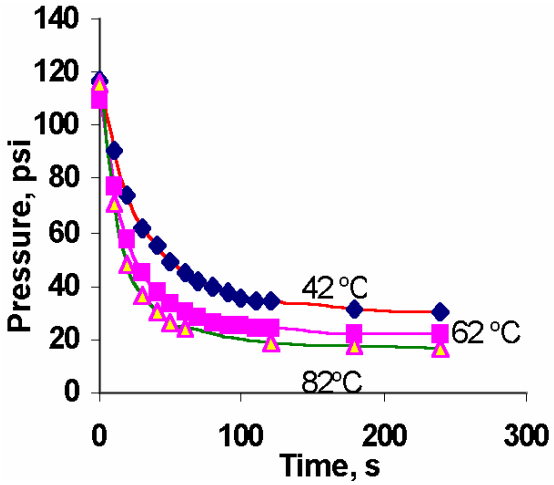

Fig. 6.14. Response profiles for the monolithic valve using different gradients of temperature. The microchip was submerged at time 0 in bath with indicated temperature.

The performance of the valve is also affected by the temperature of the water bath in which the chip is submerged. Figure 14 shows the closing kinetics for the valve at temperatures of 42, 62, and 82 °C. As expected, the higher the temperature, the large the temperature gradient between the bath and the channel, and the faster the action. However, this effect is not linear thus indicating that the heat transfer through the glass controls the rate and consequently the performance of the valve.

PolyNIPAAm is directly prepared as a monolithic polymer inside the microfluidic channel of glass microchips that were fabricated in the microfabrication laboratory of the University of California at Berkeley. A representation of it is shown in Fig. 15. The channel is 200 μm wide, 100 μm deep, and about 6 cm long. The micro channel wall is vinylized with A174 silane before use to enable covalent attachment of the monolith.

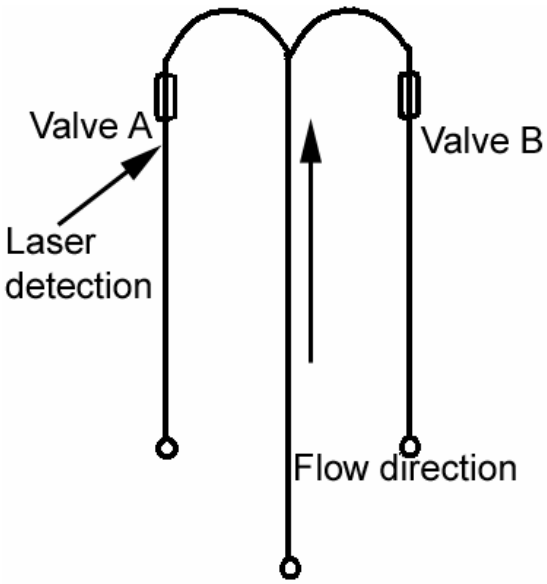

Fig 6.15. Microchip to test monolithic polyNIPAAm valve.

PolyNIPAAm solution is prepared by mixing 187.5 mg N-isopropylacrylamide with 9.375 mg N,N'-methylenebisacrylamide, 0.9375 mg 4,4'-azobis(4-cyanovaleric acid) and 4 g water. 5% of the crosslinking reagent (N, N'-methylenebisacrylamide) is added to ensure the mechanical strength of the polymer, and only 0.5% of a water soluble initiator (4,4'-azobis(4-cyanovaleric acid)) is used, since it is found that the polymerization proceeded rather fast even with a low concentration of initiator.

The solution is purged with nitrogen gas for 10 minutes to remove dissolved oxygen. It is injected into the microchip channel using a volumetric pipette. The access hole is then sealed with tape. The chip is covered with a mask and put onto a 32 ºC equilibrating plate (temperature maintained with circulating water), and UV polymerized for 45 minutes (Oriel deep UV illumination system series 8700 with a 500 W HgXe lamp). Polymerization is allowed to proceed at 32 ºC, since it is observed that polymerization at a higher temperature could result the formation of a macroporous hydrogel and increase the speed of the thermal response [Yan95]. The temperature is not increased further because at a higher temperature, the patterning procedure becomes

difficult and the edges of the polymer became unclear. The resulting polyNIPAAm monolith is 2 mm long. Its picture is shown in Fig. 16. The chip is washed with water, and connected to a micro-High Performance Liquid Chromatography (HPLC) with a 100 μm i.d. fused silica capillary.

Thermal-electrical (TE) elements (4 mm square) are used to control the local heating and cooling process. During a heating cycle, TE element raises the temperature to 57 ºC, and during a cooling cycle, it reduces the temperature to 16 ºC. Since the low critical solution temperature of PolyNIPAAm is 32 ºC, at 16 ºC, the crosslinked polymer is solvated in an aqueous solution, the polymer is in the swell-mode, and the channel is closed, whereas at 57 ºC, the polymer is dissolvated, and is in the shrink-mode, and the channel is therefore open.

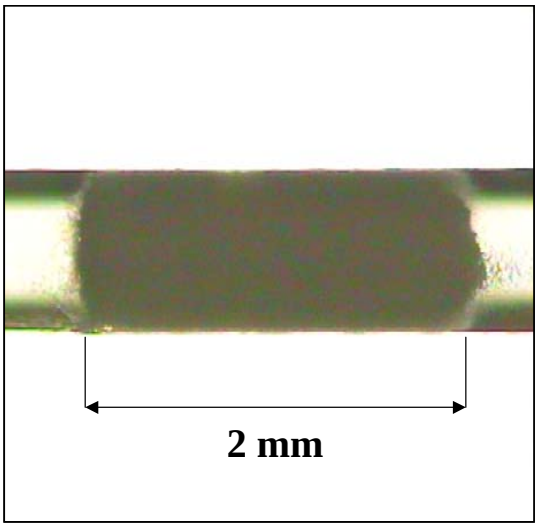

Fig. 6.16. Optical micrograph of the monolithic valve.

It is well known that glass is not a good thermal conductor. To increase the thermal conductivity, the thickness of a small section of the chip (4 mm square) on one side of the wafer where the PolyNIPAAm valve located is reduced to 45 μm by HF etching. The chip is then attached to thermal-electrical (TE) elements using a specially designed holder to ensure a good physical contact between the glass wafer and the TE elements. This is shown in Fig. 17. The other option would be placing the resistor directly

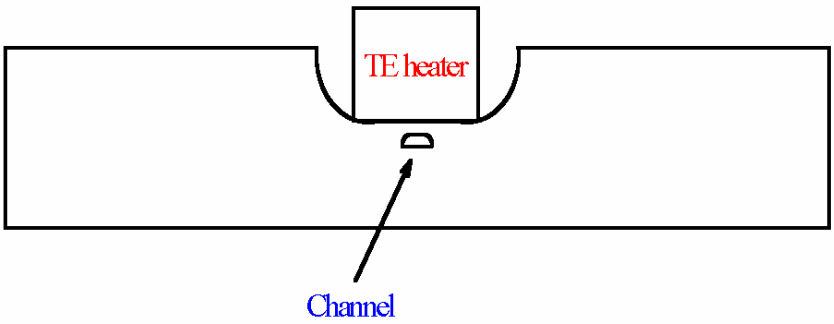

Fig. 6.17. Designed of a microchip with enhanced rate of heat transfer. TE is the thermal electrical cooler/heater (Peltier element).

within the channel. However, the need for laying wires from the outside into the sealed channel makes this approach technically difficult.

The valving effect of a single PolyNIPAAm monolith is first tested. Both TE elements A and B are set on the heating cycle so that both valves will be open. The mobile phase containing 25 nM Coumarin 519 is running through the center channel at a flow rate of 2.5 μL/min (driven by a micro-HPLC). Since valves A and B are both open, the mobile phase runs through both channels. Once the laser detection point behind valve A is set, as sample passed the detection point, it emits fluorescent light, the light is detected by the PhotoMultiplier Tube (PMT). This gives a constant fluorescence signal. When TE element A is turned to the cooling cycle, the flow of the mobile phase at channel A stops and a sudden drop of the fluorescence intensity is observed due to the photobleaching effect. If TE element A is turned to the heating cycle again, valve A opens, mobile phase again runs through channel A, and a sudden increase of the fluorescence intensity is observed. This opening/closing cycle is repeated several times, and a pattern of fluorescence intensity going up and down is observed as shown in Fig. 18. A closer examination reveals that valve A closes in about 5.7 s and opens in about 3.5 s as shown in Fig. 19. Considering that earlier experiments showed the photobleaching speed was about 0.7 s indicates that the opening speed of the valve is about 5.0 s.

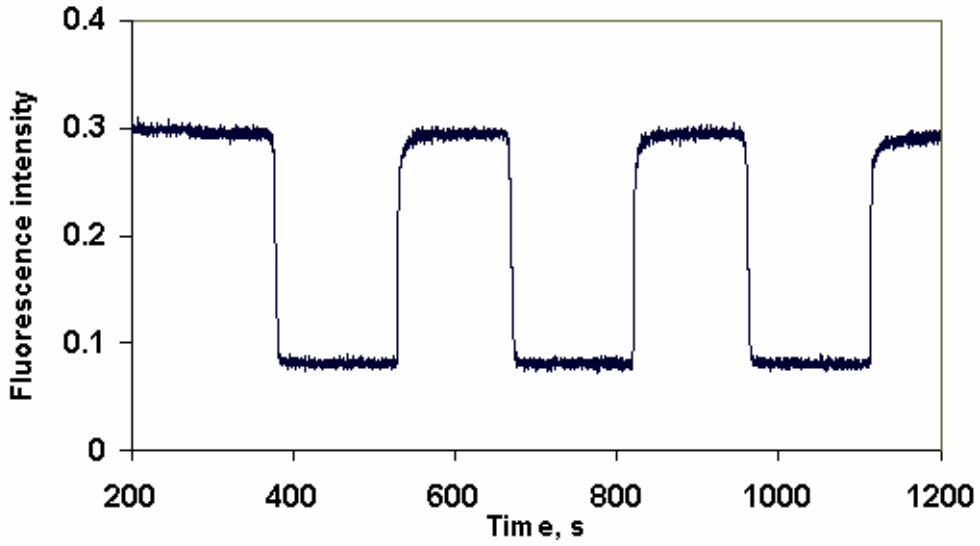

Fig 6.18. Single valve action.

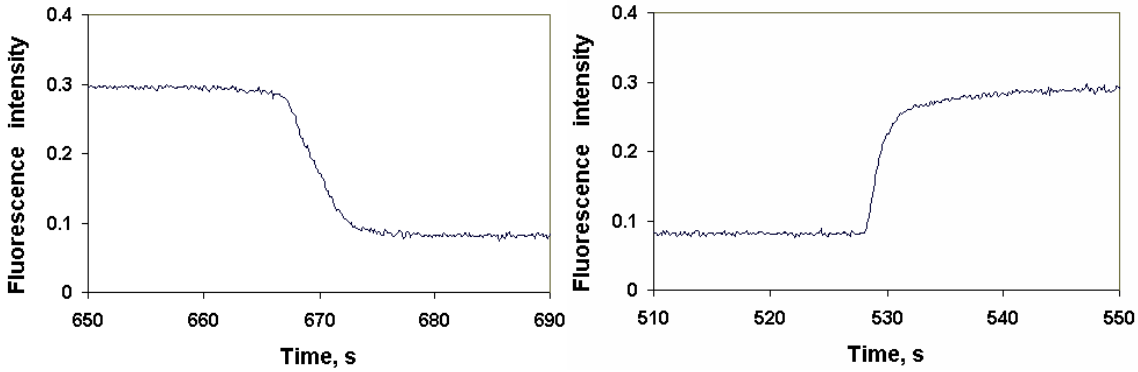

Fig 6.19. A closer view of single valve action: opening (left) and closing (right) of the valve.

The valving effect of a two-valve system is subsequently tested, again using a sample concentration of 25 nM Coumarin 519, and a flow rate of 2.5 μL/min. In this case, TE element A is set on the heating cycle and B on the cooling cycle. Once mobile phase containing Coumarin 519 is run through the center channel, since valve A is open and valve B is closed, it runs through channel A only. When the laser detection point behind valve A is set, as sample passed the detection point, it is detected by the PMT. This gives a constant fluorescence signal. Once TE element A is turned to the cooling cycle and B to the heating cycle, the flow of the mobile phase at channel A stops and a sudden drop of the fluorescence intensity is observed. The mobile phase runs through

channel B instead. When TE element A is turned to the heating cycle and TE element B to the cooling cycle again, valve A opens and B closes, mobile phase again runs through channel A, and a sudden increase of the fluorescence intensity is detected. This circle is repeated several times. A curve very similar to Fig. 18 is observed. The response time is calculated and it shows that the valve closes in about 10 s, and opens in less than 1 s.

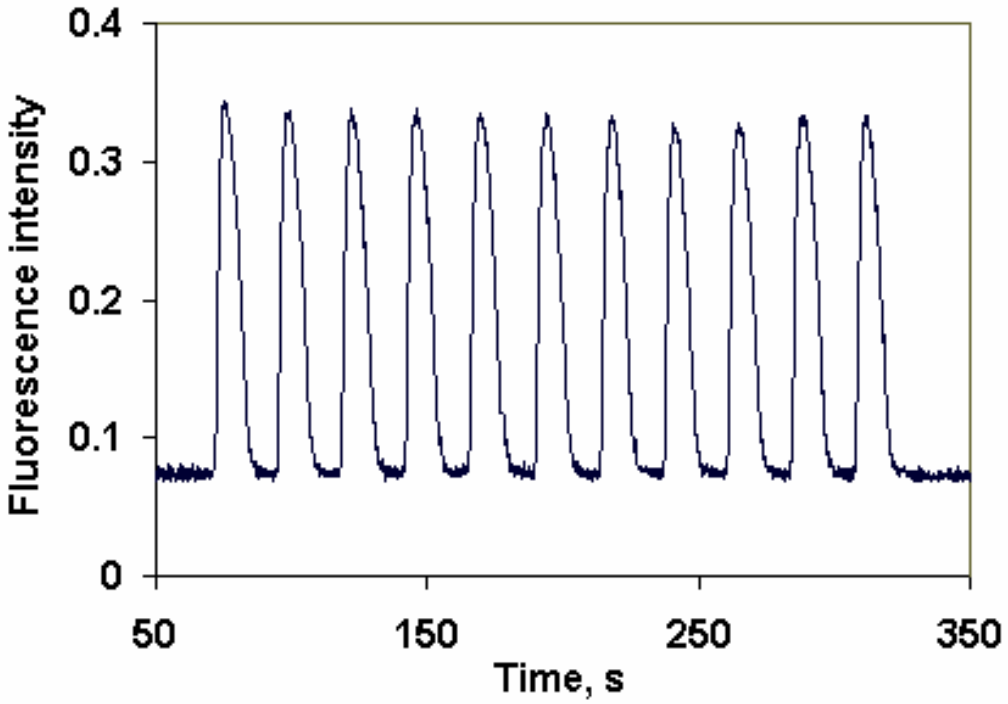

Fig 6.20. Sequential opening and closing of a single polyNIPAAm

The sequential response of a single valve is also tested. In this case, valve B is left open at all time, and valve A is kept open for 12 s and closed for 12 s sequentially. The result is the observation of a number of peaks sequentially appears on the chromatogram shown in Fig. 20, which clearly demonstrates that the valve can be repeatedly operated in a short period of time and remained to give the same performance. Earlier results also indicates that the valve could stand up to 200 psi pressure without noticeable structural damage. And at a flow rate of up to 50 mL/min, it gave almost no flow (0 psi) resistance.

6.8 Mesoscale Thermally Responsive Monolithic Valve With Adjustable LCST

Previously, monolithic plugs of NIPAAm (N-isopropylacrylamide) gel crosslinked with 5% methylenebisacrylamide have been prepared via photoinitiated polymerization within the channel of a microfluidic chip and their valving function actuated by temperature has been demonstrated. These robust valves with a transition temperature slightly above 30 ^{o}C responded very quickly to the external stimulus and kept their performance in repeated "open-close" cycles. However, their transition temperature was too low for some applications such as the control of flow through microfabricated PCR chambers that must remain closed at much higher temperatures. Therefore, a new family of thermally actuated valves have been prepared from photocopolymerized crosslinked NIPAAm and N-ethylacrylamide (NEAAm) gels whose lower critical solution temperature (LCST) can be adjusted within a broad range to meet the temperature requirements specific for some applications.

Thermoresponsive monolithic copolymers are prepared by photopatterning of a liquid phase consisting of an aqueous solution of NIPAAm, NEAAm, N,N'-methylenebisacrylamide (a crosslinker that provides for insolubility of the polymer gel plug), and 4,4'-azobis(4-cyanovaleric acid). The products are used as valves within the channels of microfluidic devices. The volume change associated with the polymer phase transition at its LCST leads to the rapid swelling and the de-swelling of the 2.5% crosslinked monolithic gel thus enabling the polymer to close or open the channel and to function as a non-mechanically actuated valve. The lower critical solution temperature at which the valve switches is easily adjusted within a range of 35-74 ^{o}C by varying the proportion of the monovinyl monomers in the polymerization mixture.

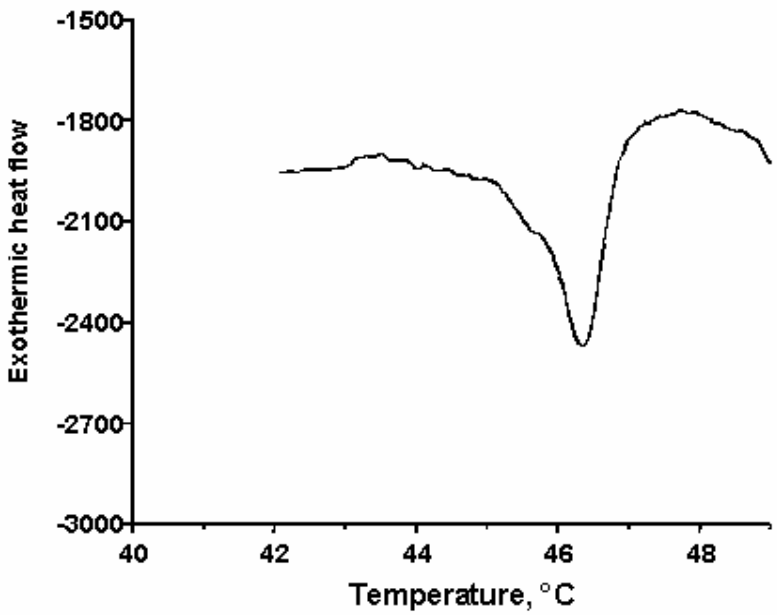

Fig. 6.21. Differential scanning calorimetric trace enabling determination of LCST.

The differential scanning calorimetry (DSC) of thermally responsive polymers swollen in water is used to determine the LCSTs. A typical DSC thermogram recorded with 2.5% crosslinked poly(NIPAAm-co-NEAAm) with equimolar ratio of both comonomers is shown in Figure 21. Using DSC, the LCSTs for both crosslinked homopolymers are found to be 34 and 74 °C, respectively. Since LCSTs for crosslinked poly(NIPAAm-*co*-NEAAm) has never been published, a series of these copolymers with a varying molar fraction of NEAAm in the monomer mixture have been prepared and their LCSTs were determined. The results are shown in Fig. 22. As expected, LCST of the copolymers increases with increasing NEAAm contents. Since NEAAm is more hydrophilic than NIPAAm, the increased hydrophilicity of the polymer results in an increase in LCST. However, this function is not linear. Equation 1 can be used for the calculation of LCST of copolymers [Liu99]:

$$T_{copol} = \frac{\mu_1 T_1 + K\mu_2 T_2}{\mu_1 + K\mu_2} \qquad (1)$$

where T_{copol} is the LCST of the copolymer, μ_1 and μ_2 are the molar fractions of each monomer ($\mu_1 + \mu_2 = 1$), T_1 and T_2 are LCSTs of the respective homopolymers, and K is a

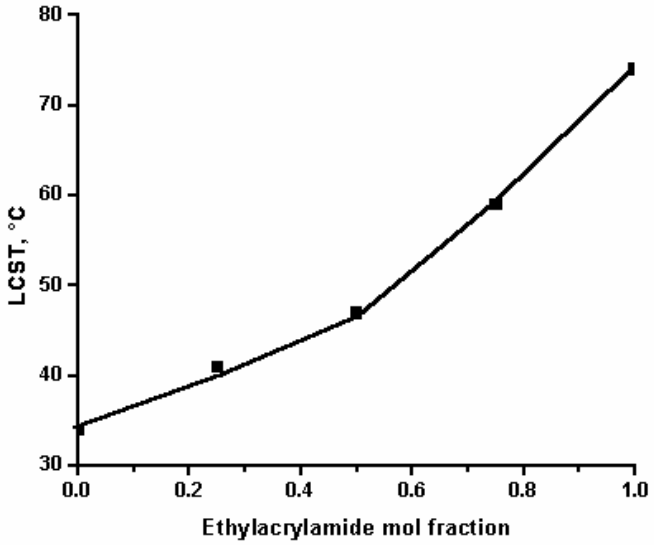

Fig. 6.22. LCST of gels as a function of the molar fraction of NEAAm in the copolymer.

weighting parameter, which is obtained from fitting of the experimental results. This experimental data afford a K value of 0.53 for poly(NIPAAm-*co*-NEAAm) gels.

Observation of the thermally responsive polymers in optical microscope reveals that the polymer gel is transparent at room temperature since it is completely solvated with water. In contrast, the polymer separates from water at 60 °C and the pores are formed. The phase separated polymer chains have a refractive index different from that of water and the valve appears opaque. The attempts to use conventional scanning electron microscopy (SEM) to image the gel valve were unsuccessful since the drying of the sample required for this technique always resulted in complete damage of the original polymer structure. In contrast, environmental SEM is capable of imaging both wet and dry specimens of conductive or non-conductive materials at magnifications typical of SEM. Dehydration of the sample can be inhibited by the correct pump down procedure, it is by the replacement of air normally located in the chamber with an imaging gas - water

vapors. This enables wet samples to be observed in their "natural state". Figure 23 shows the environmental SEMs of the poly(NIPAAm-co-NEAAm) valve in both wet and dry state. No features are seen in the image of the hydrophilic gel swollen with water. The valve is “closed” and no pores can be observed in the homogeneous mass of the gel at the magnification used in this imaging. On decreasing pressure in the chamber, water evaporates from the gel and the polymer dries. Despite both the partial shrinkage and displacement of the polymer from the capillary that cannot be prevented, the right figure in Fig. 23 clearly demonstrates that the originally homogeneous gel becomes a lace-like material with a distinct porous structure.

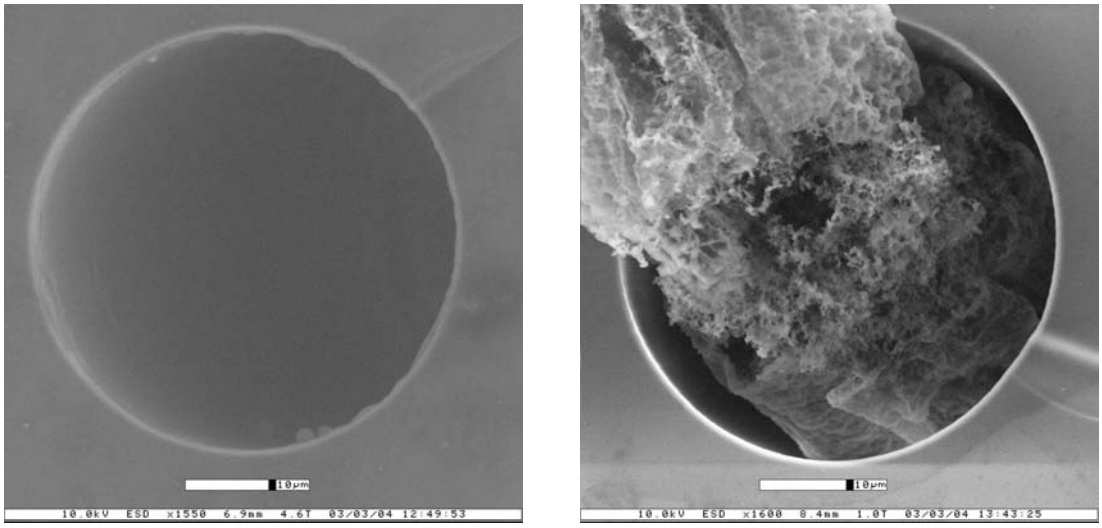

Fig. 6.23. Environmental scanning electron micrographs of the crosslinked poly(NIPAAm-co-NEAAm) valve in wet (left) and dry state (right).

The environmental SEM micrographs indicate significant differences in the pore structure of both dry and wet thermally responsive polymer. While the image of gel in the wet state at low temperature (valve is closed) is likely to represent the reality, the structure of the gel in water at a temperature above LCST is certainly different from that seen in the SEM micrograph of the dry sample. Since it is difficult to observe the valve under these conditions directly, the pore size of the valve has been investigated in open position using fluorescently labeled monodisperse beads. Obviously, no flow of liquid is

possible through the valve in the close position. Therefore, none of the particles with diameters in a range of 0.020-7.20 μm can flow through the valve. However, after increasing the temperature of the valve and its opening, particles with a size of up to 3.69 μm can permeate the valve with virtually no interference of the polymer matrix. For example, Fig. 24 shows two optical micrographs of the 2 μm beads freely moving through the opened valve. In contrast, the valve is no longer permeable for monodisperse beads with a size of 7.20 μm. As a result, all these beads are collected in front of the valve that works now as an efficient filter. To confirm these findings, the liquid that flew through the valve is also colleted and searched for the beads in it. As expected, using optical microscopy, a large number of fluorescent beads can be found in the permeate of 3.69 μm beads dispersion while no 7.20 μm beads were found in the effluent. These measurements indicate that the actual pore size of the valve in position open is somewhere in a range of 3.69-7.20 μm.

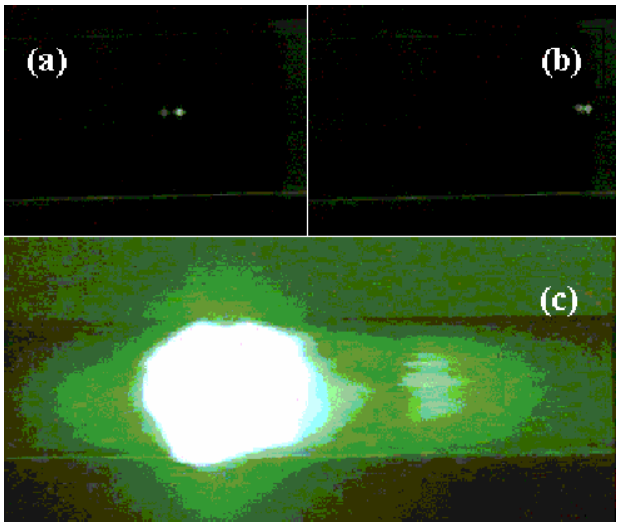

Fig. 6.24. Optical microscopic monitoring pore size of poly(NIPAAm-co-NEAAm) valve at position open using fluorescently labeled monodisperse beads. (a) and (b) are taken at the same point at different times illustrate flow of 2 μm polystyrene microspheres through the valve. (c) shows accumulation of monodisperse FITC-labeled 7.2 um poly(glycidyl methacrylate-co-ethylene dimethacrylate) beads in front of the valve.

The actual valves are prepared by copolymerizing NIPAAm and NEAAm in the presence of 2.5 % of methylenebisacrylamide. Using masks with varying length of the opening, valves with the length in a range of 500 μm to 5 mm are easily prepared. At the temperature below LCST, this gel plug is swollen with water and the valve is in position "closed". Once heated to a temperature above LCST, the polymer chains quickly desolvate, the gel shrinks and the valve opens. One of the key requirements for the practical use of such valves is their resistance to pressure that builds up in the front of the

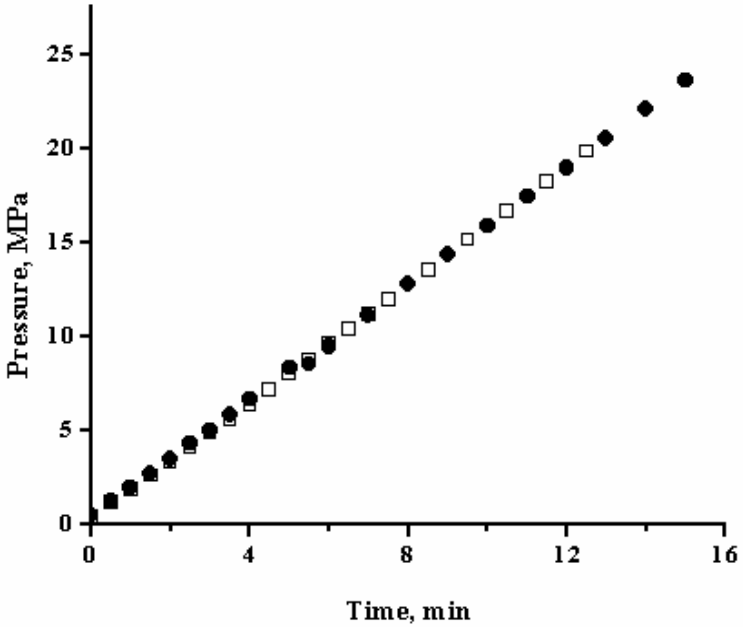

Fig. 6.25. Pressure building within an open capillary containing valve in position close (□) and empty capillary sealed at the end (●).

valve when closed. To investigate the behavior of the valve under pressure, 5 mm long valve is prepared from crosslinked poly(NIPAAm-co-NEAAm) (molar ratio 1:1) in a capillary. The capillary is connected to the pump and back pressure in the system is monitored. Almost no back pressure is observed in the system heated to 57 ^{o}C at which the valve is in position open. In contrast, Fig. 25 shows the linear increase in pressure within the capillary with the valve in closed position. No deviation from linearity is observed even at a back pressure as high as 18 MPa at which the pump is switched off,

since these extreme pressures are unlikely to be encountered in real microfluidic applications. For comparison, a similar experiment also shown in Fig. 25 is carried out with an empty capillary sealed at one end. Clearly, results of both measurements are identical. This indicates that the 5 mm long gel plug completely prevents the flow through with no leakage even at a very high pressure. Visual examination of the valve in an optical microscope following these experiments did not reveal any structural damage or dislocation of the valve. Even a much shorter valve with a length of only 0.5 mm prepared in 50 μm i.d. capillary withstands pressures of up to 0.35 MPa without damage. Although the structural strength of this thin membrane-like plug is lower than that of much longer valves, its pressure resistance is still sufficient for numerous microfluidic operations.

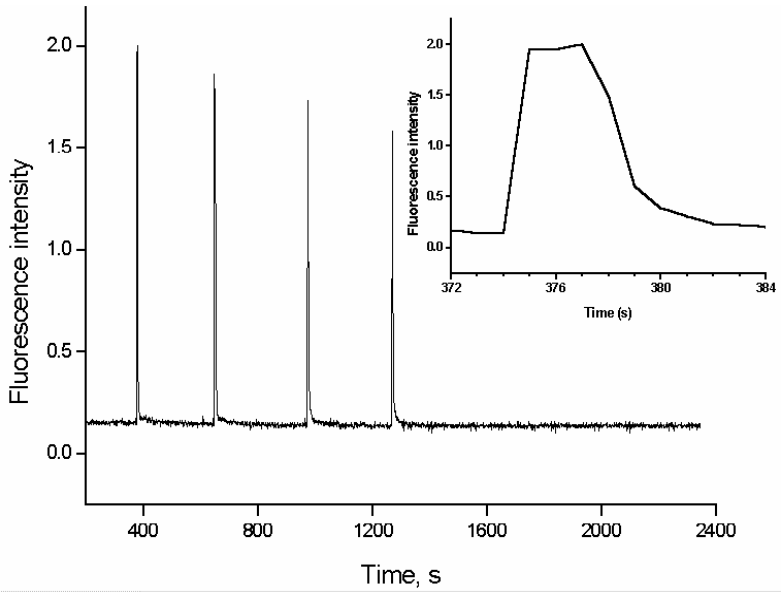

Figure 6.26. Monitoring of the valving function of 2.5% crosslinked poly(NIPAAm-co-NEAAm) monolith in straight channel using photobleaching of 100 nmol/L aqueous Coumarin 519 solution at a flow rate of 1 μL/min. Inlet: expanded part of the profile.

The performance of the 5 mm long poly(NIPAAm-*co*-NEAAm) valve located in a capillary is detected via photobleaching using a 100 nmol/L aqueous solution of Coumarin 519 at a flow rate of 1 μL/min driven by a micro-HPLC pump. The repetitive opening and closing of the valve shown in Fig. 26 is achieved by respective submersing

and lifting the capillary from a water bath heated to 60 ^{o}C. Clearly, no leakage, which would result in flow through the valve, incomplete photobleaching, and detection of appreciable fluorescence, can be observed in the system even at an extremely high pressure of 15 MPa. The inlay in Fig. 26 is an enlarged trace of one cycle. The actuation is very fast with 1 and 2 s required for opening and closing, respectively.

In addition to the experiments performed in a capillary, the valve is also prepared in a glass chip with a straight channel. The switch to position “open” is actuated by a thermo-electrical element attached to the chip beneath the valve. The rate of both opening and closing is equal to that found for the valve in capillary. However, the switching from the position close to open must be initiated by heating earlier to avoid the build up of high pressure within the channel of the chip. In contrast to capillaries, the chips are generally much less pressure resistant and any high pressure would result in their delamination and irreparable damage.

The microchip that contains a pair of valves for alternating flow through two channels is also tested using specifically designed microchip. Once again, photobleaching of the 100 nmol/L aqueous Coumarin 519 solution is used to detect the closing of the channel. Typically, the thermo-electrical element beneath the first valve (A) is set to heat to a temperature of 57 ^{o}C while the other serving valve B is set to cool to 16 ^{o}C. These two temperatures are preset in the testing unit and cannot be changed easily. In this setup, valve A is open while B is closed and all the Coumarin solution flows at a rate of 2 μL/min only through valve A. As a result, the detector focused at point located behind valve A monitors a constant fluorescence signal. When the functions of both thermo-electrical elements are reversed, valve A switches to the closed mode with no flow through and the monitored fluorescence intensity decreases rapidly. All the solution now flows through opened valve B. This cycle is repeated several times at intervals 300 s

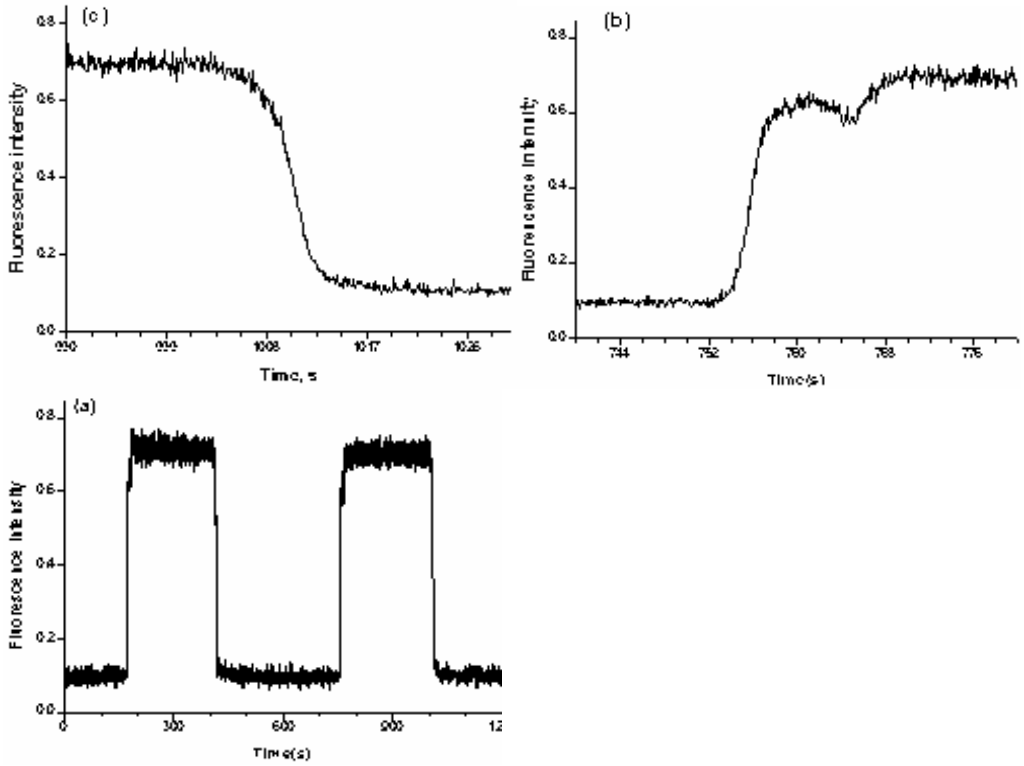

Fig. 6.27. Monitoring of the valving function of 2.5% crosslinked poly(NIPAAm-co-NEAAm) monolith in M shaped microfluidic system that includes two valves using photobleaching of 100 nmol/L aqueous Coumarin 519 solution at a flow rate of 1 μL/min. (a) original trace; expanded parts of (b) opening and (c) closing profiles.

long. Figure 27 shows the intensity of fluorescence recorded during this cycling. Enlarged records of the increasing and decreasing sections of the peak also shown in Fig. 27 facilitate the estimation of the response times for both closing and opening that are 3-4 s. These response times are slightly longer compared to the single valve operation in a capillary shown in Fig. 26. In the single valve implementation, a significant pressure of several MPa builds up in front of the valve that propels the liquid through the valve even before it opens completely. In contrast, the branched system features no significant internal pressure since one channel is always open and enables the flow. Therefore, the force driving the flow is smaller and the valve is permeable only after it opens to a much larger extent and the other valve is completely closed.

The switching function of the poly(NIPAAm-co-NEAAm) valve has also been tested at a high frequency. The temperature of the thermo-electrical elements was switched each 10 s successively between 16 and 57 °C to actuate the valves and the flow was directed through the respective branches. Figure 28 shows the changes in fluorescence with respect to the position of the valve. No change in the performance is observed even after more then 100 cycles.

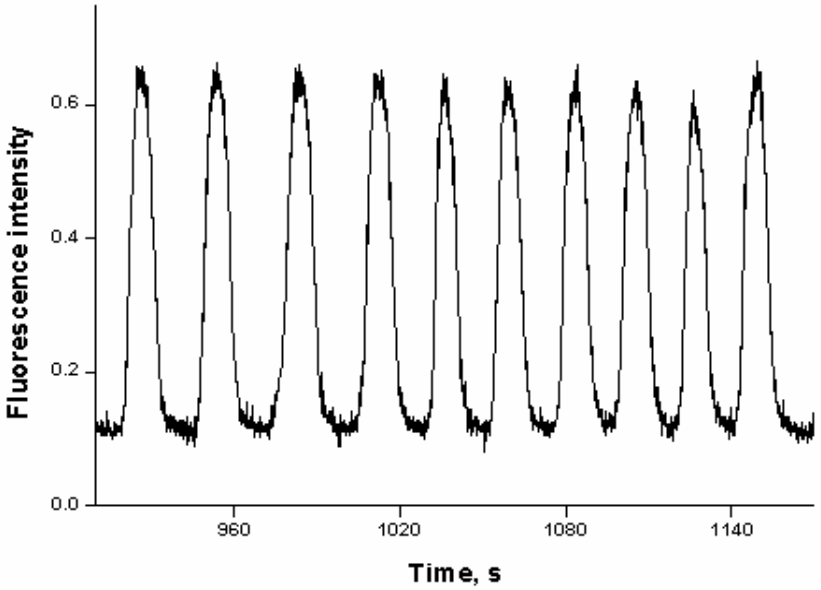

Fig. 6.28. High frequency valving operation of the 2.5 % crosslinked poly(NIPAAm-co-NEAAm) monolithic gels in the M-shaped two valve microfluidic system actuated every 10 s.

Since it is unlikely that the valve would only operate in pure water, we also tested its performance in aqueous solutions of salts. No effect on the function was observed after repetitive cycling even using a 1.0 mol/L sodium chloride solution in 20 mmol/L phosphate buffer (pH=7.4). This finding clearly demonstrates the versatility of our valve and its ability to perform well under conditions typical of numerous microfluidic processes.

6.9 Conclusion

In this section, a new photoresist like thermally responsive polymer was introduced. Thin film processing of this polymer was summarized. This was followed by characterizing its volume change with temperature change of the liquid it was immersed in. Around a 2-fold increase in polymer volume in water was observed when the water temperature changed from 25°C to 10°C. Then this polymer was integrated into parylene microchannels with embedded microheaters and backside etched holes to realize a surface micromachined inline valve. Since no actuated diaphragm was used to control liquid flow, fabrication of this valve was simple. Then the valve was tested first visually. Repeatable polymer shrinking in around 1 second and swelling in around 2 seconds were observed. Pressure measurements were made to demonstrate the functionality of the device. Furthermore a thermally responsive polymer similar to the photoresist like thermally responsive polymer has been fabricated in mesoscale by in-situ polymerization inside glass capillaries and glass chips. Test results of these valves give similar valving properties of these polymers however these valves can withstand much bigger pressure values since they are built into glass and the plug length is much bigger. Finally, thermally responsive polymers with adjustable critical solution temperature have been introduced and fabricated in mesoscale in glass capillaries and glass chips. Their test results show that any thermally responsive polymer with critical temprerature in the range of 32 and 74 ^{o}C can be prepared this way.

SECTION 7

CONCLUSION AND FUTURE WORK

7.1 Conclusion

In this report a surface micromachined porous polymer electro-osmotic pump and thermally responsive polymer valve have been developed for the implementation of integrated microfluidic systems on a chip.

A porous polymer with a pore size that can be adjusted from 100nm to 1 μm has been surface micromachined using a casting process for thin film formation and pattering with reactive ion etching. This porous polymer has been integrated into parylene channels with embedded electrodes to form a porous plug electro-osmotic pump. The flow rate of the electro-osmotic pump has been improved by having vertical electrodes. Electro-osmotic mobility and tortuosity/porosity measurements of the porous polymer have been performed. The vertical electrode device at 3 V DC generates 4.8 nL/min volumetric flow rate and a maximum pressure of 1540 Pa. This is 2.8 times higher than planar electrode devices. Micromachined porous polymer has tortuosity/porosity ratio of 3.3. Even though this polymer has been surface micromachined to be a part of an electro-osmotic pump, it can be useful for other purposes too. For example, it can be used as a separation medium, a filter or concentrator for specific particles. Therefore, introduction of this porous polymer film into the microfluidics arena is significant.

Electrochemistry of a two-electrode and an electrolyte system has been investigated to understand the low frequency asymmetrical net zero averaged current drive and high frequency symmetrical AC drive. Low frequency asymmetrical net zero averaged current drive has been found to have net non-zero voltage response due to switching to diffusion limited region, hence voltage saturation after a small current amplitude. This is found to generate net flow that increases with the lower duty cycle and frequency. However the device may have repeatability and reliability issues due to bubble generation and electrode corrosion in the long term. High frequency AC symmetrical drive has been observed to be free of bubble generation. These results eventually led this research to the development of two new electro-osmotic pumps: porous plug electro-osmotic pump with liquid bridge and AC flowFET.

A liquid bridge configuration has been developed to allow the application of DC voltages to drive the porous plug electro-osmotic pumps without any bubble generation problems. The electrodes near the main channel are connected to the main channel using narrow porous plug branches. This allows current conduction but also constitutes high hydraulic resistance to the flow. Therefore at the nodes, where narrow porous plug branches are connected to the main channel, pressure is built up driving a hydraulic flow in the field free region of the main channel. This device gives a flow rate of 1.76 nL/min and a maximum pressure head of 1673 Pa at 50 V DC. Even though this design puts larger distance between electrodes than the devices with electrodes inside the main channel, hence requires the application of higher voltages, more compact devices can be fabricated that will lower these voltage values. Furthermore, instead of directly pumping the desired liquid, the pump can have its own working liquid that will maximize its performance and this working liquid will push the real liquid under investigation separated from it with an air gap. This way, effects of liquids with different properties on the pump's performance will be eliminated. This will also eliminate any concerns about

trapping of big sized particles or molecules in the porous polymer. In that sense, this pump acts as an on-chip pressure source. It can generate very precise flow rates in the nL/min range without any bubble generation problem and maximum pressure heads in KPa range, which is adequate for flows in microfluidic channels. The pump has no moving part, low power consumption and high integration density. As a result, this pump is ready to build for an integrated microfluidic system.

Furthermore, the working principle of flow rectification with zeta potential modulation has been demonstrated by mimicking an insulated porous metallic structure with a perforated electroplated-nickel structure insulated with thin parylene. This pump uses high frequency (1 KHz) AC drive. Flow rectification with this drive is achieved by modulating the zeta potential of surfaces responsible for the electro-osmotic flow by an insulated gate electrode synchronously with the voltage signal at the drive electrodes. A simple device fabricated to prove the concept gives a flow rate of 16 nL/min with a pressure head of 2.3 Pa in response to a 1 KHz AC square signal with a magnitude of 17 volts. However, a practical device requires more and narrower parallel channels. Therefore devices with parallel nano channels have to be fabricated. The nano channel will increase the maximum pressure head that this pump can generate to KPa range. However, the height of the nano channels must be kept the same (20 μm) or multi layers of nano channels that eventually make up to this height must be fabricated in order to prevent any flow rate reduction. This would be a challenge but a good research effort. After this improvement, these pumps can also be built for an integrated microfluidic system.

A thermally responsive polymer has been surface micromachined using spinning and/or casting and patterning lithographically. It shows repeatability and around 100% volume change by changing the liquid temperature from 25 to 10 °C thus a big potential to realize valves with low leakage. This thermally responsive polymer is integrated into

parylene channels with embedded microheaters to form a valve. The valve has been tested with backside etched through holes. Furthermore a thermally responsive polymer similar to the photoresist like thermally responsive polymer has been fabricated in mesoscale by in-situ polymerization inside glass capillaries and glass chips. Test results of these valves give similar valving properties of these polymers however these valves can withstand much bigger pressure values since they are built into glass and the plug length is much bigger. Since the critical temperature of the cross linked thermally responsive polymer is below room temperature, these devices need cooling, making them impractical. However, copolymerization of N-ethylacrylamide with poly N-isopropylacrylamide has been shown to enable fine-tuning of the transition temperature and creation of valves operating at predetermined temperatures ranging from 35 ^{o}C to 74 ^{o}C. These valves have been fabricated in mesoscale in glass capillaries and glass chips. Their test results indeed show that any thermally responsive polymer with critical temprerature in the range of 35 to 74 ^{o}C can be prepared this way. In this report, further research on surface micromachining of these thermally responsive polymers has not been done. However, using this same approach, they can also be surface micromachined to make a practical microvalve. Therefore demonstration of this kind of material working as a valve is significant.

Finally, this report sets a good example for the introduction of new polymer films into the microfluidics area. This area is very diverse and has many different applications. So far sensors, micropumps, microvalves and microfluidic channels have been fabricated individually with different technologies on different substrates. Their individual performance has been very promising. However, they cannot be integrated on the same substrate to form a system because of technology incompatibilities. Overall this work is just a beginning for this final goal of integration. Parylene processing or more generally low temperature polymer processing has been chosen as an integration platform. After

this work, large-scale integratable pumps are ready for this platform and after some modification large-scale integratable thermally responsive polymer valves will be ready. By targeting main application areas like DNA, protein and cell analysis systems, new polymer films and new devices can be introduced to this platform according to the needs of these applications. This way, after every targeted specific application, new polymer films, new microfluidic devices and the knowledge of how they can be integrated together will be added to this platform. Eventually, following this approach, fabricating a specific total analysis system with a complex task will be a matter of bringing different modules together.

7.2 Future Work

An ion selective membrane like Nafion or others can be surface micromachined and used for the electrodes of the porous plug electro-osmotic pump. This way any DC voltage can be applied to the electrodes inside the main channel covered with the Nafion film without any bubble generation.

The effect of AMPS solution and different pore sizes of the porous polymer formed with different porogenic solvent percentages, on electro-osmotic mobility of the porous polymer, can be characterized.

Thermally responsive polymer valves with adjustable critical solution temperatures can be surface micromachined and integrated into parylene channels with embedded microheaters to form a microvalve therefore eliminating the need for cooling.

Surface micromachining of the poly NIPAAm itself (without co-polymerizing to another polymer) can be sought. This will improve the valve performance because co-polymerization will not change its LCST and sharp volume change response.

AC flowFETs show very promising characteristics to form an integrated system. However, these devices need improvement. Their performance can be improved by having parallel insulated metallic nano-channels.

Finally, there are many types of systems that can be built with these pumps and valves like fully integrated DNA, protein and cell analysis chips and capillary electrophoresis chromatography (CEC) and high performance liquid chromatography (HPLC) systems. A biological or chemical application in these areas must be chosen and its implementation must be sought using these pumps and valves. However, pumps, valves and microchannels are not enough to form an integrated system. Conductivity flow sensors which require interdigitated electrodes or microheaters can be easily integrated into this system for flow control. Capacitive parylene pressure sensors can also be integrated for this purpose. Biochemical sensors for the detection of reagents and reactions must also be integrated to achieve a micro total analysis system (μTAS). Electro-chemical sensors look very promising for this task because they are very easy to fabricate and can be easily integrated into this parylene technology. However, electrochemical sensor sensitivity might be an issue. They perform poorly compared to fluorescent detection or other detection techniques. Therefore, there is a need for a research effort in this area.

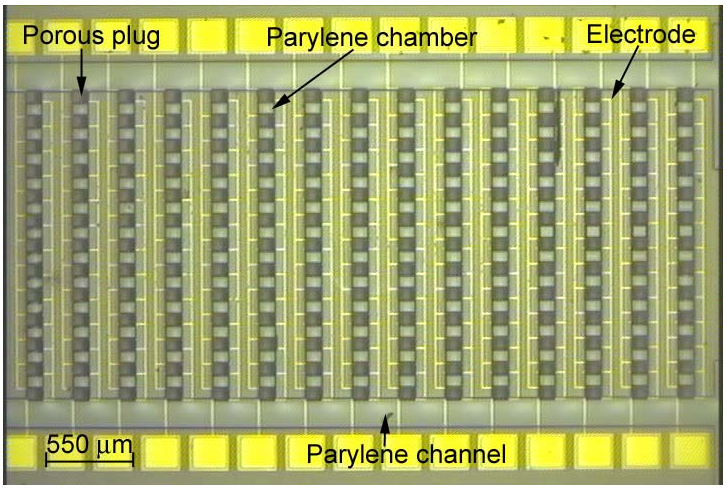

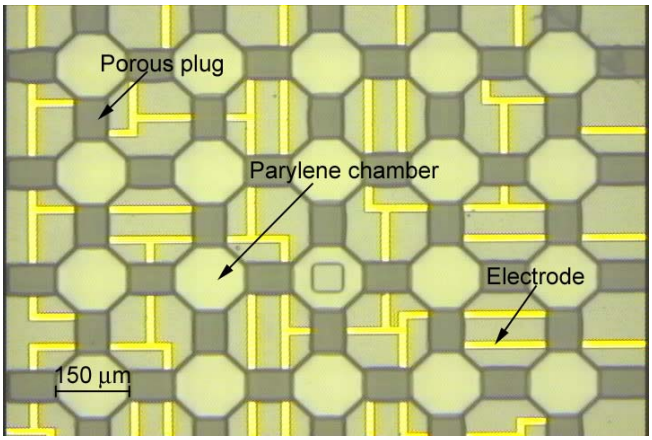

Fig. 7.1. Test structures showing large-scale integration of porous plug electro-osmotic pumps.

PARTIALLY SUPPORTED PUBLICATIONS BY THIS CONTRACT

Ph.D. Thesis

These are the Ph.D. theses supported partially by this contract.

- S. Mutlu, *Microfluidic Biochemical Analysis System With Electro-Osmotic Pump and Thermally Responsive Polymer Valve*, PhD. Thesis, University of Michigan, Ann Arbor, 2004.
- P. Selvaganapathy, *Microfabricated Components For An Integrated Microfluidic Electroanalysis System*, PhD. Thesis, University of Michigan, Ann Arbor, 2002.
- J. Zheng, *Integrated Capillary Electrophoresis System For DNA Analysis, PhD. Thesis*, University of Michigan, Ann Arbor, 2003.

Conference and Journal Publications

These are the conference and journal publications supported partially by this contract.

- S. Mutlu, F. Svec, C.H. Mastrangelo, J.M.J. Frechet, Y.B. Gianchandani, "Enhanced Electro-Osmotic Pumping With Liquid Bridge and Field Effect Flow Rectification, " Presented in *IEEE MEMS 2004 Conference*, Maastricht, The Netherlands, Jan. 25-29, pp. 850-853.
- S. Mutlu, C. Yu, F. Svec, C.H. Mastrangelo, J.M.J. Frechet, Y.B. Gianchandani, "A Thermally Responsive Polymer Microvalve Without Mechanical Parts Photo-Patterned In

A Parylene Channel, ” *Proc. Transducers 2003 Conference*, Boston, Massachusetts, USA, June 8-12, pp. 802-805.

- S. Mutlu, P. Selvaganapathy, C. Yu, F. Svec, C.H. Mastrangelo, J.M.J Frechet, “ Micromachined Porous Polymer For Bubble Free Electro-Osmotic Pumping, ” Presented in *Proc. IEEE MEMS 2002 Conference*, Las Vegas, USA, Jan. 20-24, pp. 19-24.
- P. Selvaganapathy, Y.S.L. Ki, P. Renaud, C.H. Mastrangelo, “Bubble-Free Electrokinetic Pumping,” *J. Microelectromech. Syst*., vol. 11, pp. 448-453, 2002.
- Q. Luo, S. Mutlu, Y.B. Gianchandani, F. Svec, J.M.J. Frechet, “Monolithic Valves For Microfluidic Chips Based On Thermoresponsive Polymer Gels, ” *Electrophoresis*, vol.24, 2003, pp. 3694-3702.
- C. Yu, S. Mutlu, P. Selvaganapathy, C.H. Mastrangelo, F. Svec, J.M.J. Frechet, “Flow Control Valves For Analytical Microfluidic ChipsWithout Mechanical Parts Based On Thermally Responsive Monolithic Polymers, ” *Analytical Chemistry*, vol.75 No. 8, April 15 2003, pp.1958-1961.
- S. Mutlu, C. Yu, P. Selvaganapathy, F. Svec, C. H. Mastrangelo, J.M.J. Frechet “Surface Micromachined Porous-Plug Electro Osmotic Pump,” *J. Microelectromech. Syst,* in review.

Patent Application

This is the patent application supported by this contract.

S. Mutlu, P. Selvaganapathy, C. Yu, F. Svec, J.M.J. Frechet, C.H. Mastrangelo, “Porous Polymers: Composition And Uses Thereof,” U.S. Patent Serial No.: 10/346300 UM-07727.

BIBLIOGRAPHY

[Ala01] J.P. Alarie, S.C. Jacobson, B.C. Broyles, T.E. McKnight, C.T. Culbertson, J.M. Ramsey, "Electroosmotically induced hydraulic pumping on microchips," *Tech. Dig., μTAS*, 2001, pp. 131-132.

[Bar01] A. J. Bard, L. R. Faulkner, "*Electrochemical Methods – Fundamentals and Applications*", John Wiley & Sons, New York, 2001.

[Bar90] S.F. Bart, L.S. Tavrow, M. Mehregany, J.H. Lang, "Microfabricated electrohydrodynamic pumps," *Sensors and Actuators A*, vol. A21, p.193-197, 1990.

[Bar95] P.W. Barth, "Silicon Microvalves For Gas Flow Control," Proc. *Transducers'95*, pp. 276-279, 1995.

[Ber53] T. Berzins, P. Delahay, "Theory of Electrolysis at Constant Current in Unstirred Solution. II. Consecutive Electrochemical Reactions," *Journal of American Chemistry Society*, vol.75, pp. 4205-4212, 1953.

[Bia00] F. Bianchi, R. Ferrigno, H.H. Girault, "Finite Element Simulation of an electroosmotic-driven flow division at a T-Junction of miroscale dimentions," *Anal. Chem*., vol. 72, pp. 1987-1993, 2000.

[Boc73] J.O.M. Bockris, A.K.N. Reedy, *Modern Electrochemistry*: Plenum Press, 1973.

[Boh00] S. Bohm, B. Trimmer, W. Olthuis, P. Bergveld, "A closed-loop controlled electrochemically actuated micro-dosing system," *J. Micromech. Microeng.*, vol. 10, pp. 498-504, 2000.

[Boh99a] S. Bohm, W. Olthuis, P. Bergveld, "An electrochemically actuated micropump for use in a push-pull microdialysis based in-vivo monitoring system," *Proc. Transducers'99*, Sendai, Japan, pp. 880-881.

[Boh99b] S. Bohm, W. Olthuis, P. Bergveld, "An Integrated Micromachined Electrochemical Pump and Dosing System," *Journal of Biomedical Microdevices*, Vol. 1, pp. 121-130, 1999.

[Bru77] S.B. Brummer, M.J. Turner, "Electrical Stimulation With Pt Electrodes: II-Estimation of Maximum Surface Redox (Theoretical Non-Gassing) Limits," *IEEE Transactions on Biomedical Engineering*, Vol. 24, pp. 440-443, 1977.

[Bur64] D. Burgreen, F.R. Nakache, “Electrokinetic flow in ultrafine capillary slits” *Journal of Physical Chemistry*, vol. 68 (5), pp. 1084-1091, 1964.

[Cab01] C. Cabuz, W.R. Herb, E.I. Cabuz, S.T. Lu, “The Dual Diaphragm Pump,” *Proc. IEEE Micro Electro Mechanical Systems 2001*, pp. 519-522.

[Car00] E.T. Carlen, C.H. Mastrangelo, “Paraffin actuated surface micromachined valves”, *Proc. IEEE Micro Electro Mechanical Systems 2000*, pp. 381-385.

[Car01] E.T. Carlen, *Electrothermally Actuated Polymer Microvalves*. PhD. Thesis, University of Michigan, Ann Arbor, 2001

[Che02] C.-H. Chen, J.G. Santiago, "A Planar Electroosmotic Pump," *J. Microelectromech. Syst*., vol. 11, pp. 672-683, 2002.

[Chi02] R.L. Chien, L. Bousse, “Electroosmotic pumping in microchips woth nonhomogenous distribution of electrolytes,” *Electrophoresis*, vol 23, pp. 1862-1869, 2002.

[Cho03] H. Chien-Chong, S. Murugesan, S. Kim, G. Beaucage, C. Jin-Woo, C.H. Ahn, “A functional on-chip pressure generator using solid chemical propellant for disposable lab-on-a-chip,” in *Proc. IEEE MEMS'2003 Conf.*, Kyoto, Japan, pp. 16-19, 2003.

[Dos93] E.V. Dose, G. Guiocchon, “Timescales of transient processes in capillary electrophoresis,” *Journal of Chromatography A*, vol. 652, pp. 263-275, 1993.

[Fuh94] G. Fuhr, T. Schnelle and B. Wagner, “ Travelling wave-driven microfabricated electrohydrodynamic pumps for liquids,” *J. Micromech. Microeng.*, vol. 4, pp. 217-226, 1994.

[Fuj02] T. Fujiwara, O. Kitoh, T. Tsuda, “Effect of applied parallel field on electroosmotic flow in donut channel,” *Chromatography*, vol. 23, no. 1, 2002.

[Ged87] L.A. Geddes, K.S. Foster, J. Reilly, W.D. Voorhees, J.D. Bourland, T. Ragheb, N.E. Fearnot, “The rectification properties of an electrode-electrolyte interface operated at high sinusoidal current density,” *IEEE Transactions on Biomedical Engineering*, Vol. 34, pp. 669-672, 1987.

[Gre02] N.G. Green, A. Ramos, A. Gonzalez, H. Morgan, A. Castellanos, “Fluid flow by nonuniform ac electric fields in electrolytes on microelectrdes. III. Observation of streamlines and numerical simulation,” *Physical Review E*, Vol. 66, No. 026305, pp. 1-11, 2002.

[Gro99] C. Grosjean, Y.C. Tai, “ A Thermopneumatic Peristaltic Micropump,” Transducers’99, pp. 1776-1779, 1999.

[Gu02] Y. Gu, A. Baldi, B. Ziaie, R.A. Siegel, “A micromachined hydrogel-gated smart flow controller”, *Solid-State Sensor and Actuator Workshop*, Hilton Head, South Carolina, 2002.

[Har93] D. J. Harrison, K. Fluri, K. Seiler, Z.H. Fan, C.S. Effenhauser, A. Manz, “Micromachining a miniaturized capillary electrophoresis based chemical analysis system on a chip,” *Science*, vol. 261, pp. 895-897, 1993.

[Has03] E.F. Hasselbrink, Jr., T. J. Shepodd, J.E. Rehm, “High-Pressure Microfluidic Control in Lab-on-a-Chip Devices Using Mobile Polymer Monoliths,” *Anal. Chem*, vol. 74, pp. 4913-4918, 2003.

[Hof99] J. Hoffmann, M. Plotner, D. Kuckling, W.J. Fischer, “Photopatterning of thermally sensitive hydrogels useful for microactuators”, *Sensors Actuat. A, Physical*, vol. 77, pp. 139-144, 1999.

[Hun81] R.J. Hunter, “Zeta Potential in Colloid Science”, Academic Press, 1981

[Joo95] Y. Joo, K Dieu, C.J. Kim, “Fabrication of monolithic microchannels for IC chip cooling,” *Proc.IEEE MEMS*, pp. 362-367, 1995.

[Kha02] J. Khandurina, A. Guttman, “Bioanalysis in microfluidic devices,” *Journal of Chromatography A*, vol. 943, pp. 159-183, 2002.

[Ki00] Y.-S.L. Ki, R.B.M. Schasfoort, S. Sclautmann, P. Renaud, A.V.D. Berg ”Modeling of FlowFET Characteristics”, *Proc. of the MSM Int. Conference on Modeling andSimulation of Microsystems*, San Diego, USA, pp.213-217, 2000

[Lem99] A.V. Lemoff, A.P. Lee, R.R. Miles, C.F. McConaghy, "An ac magnetohydrodynamic micropump: towards a true integrated microfluidic system," in *Proc. Transducers '99*, Sendai, Japan, pp. 1126-1130, 1999.

[Lid95] D.R. Lide, CRC, *Handbook of Chemistry and Physics*, New York, 1995.

[Lin88] H.T.G. Van Lintel, F.C.M. Van de Pol, S. Bouwstra, “ A piezoelectric micro pump based on micromachining of silicon,” *Sensors and Actuators*, vol. 15, 1988, p.153.

[Liu02] R.H. Liu, Q. Yu, D.J. Beebe, “Fabrication and characterization of hydrogel-based microvalves”, *J. Microelectromech. Syst*., vol.11, pp. 45-53, 2002

[Liu99] H.Y. Liu, X.X. Zhu, “Lower critical solution temperatures of *N*-substituted acrylamide copolymers in aqueous solutions,” *Polymer*, vol. *40*, pp. 6985-6990, 1999.

[Luo03] Q. Luo, S. Mutlu, Y.B. Gianchandani, F. Svec, and J.M.J. Frechet, “Monolithic Valves For Microfluidic Chips Based On Thermoresponsive Polymer Gels, ” *Electrophoresis*, vol.24, pp. 3694-3702, 2003.

[Man01] P.F. Man, *Monolithic Structures For Integrated Microfluidic Analysis*. PhD thesis, University of Michigan, Ann Arbor, 2001.

[Man94] A. Manz, C.S. Effenhauser, N. Burggraf, D.J. Harrison, K. Seiler, K. Fluri, "Electroosmotic pumping and electrophoretic separations for miniaturized chemical analysis systems," *J. Micromech. Microeng.*, vol. 4, pp. 257-265, 1994.

[Man98] P.F. Man, C.H. Mastrangelo, M.A. Burns, D.T. Burke, "Microfabricated Capillary-Driven Stop Valve And Sample Injector," *Proc. IEEE Micro Electro Mechanical Systems 1998*, pp. 25-29.

[Mat99] S. Matsumoto, A. Klein, R. Maeda, "Development of Bi-directional Valve-less Micropump for Liquid," *Proc. IEEE Micro Electro Mechanical Systems 1999*, pp. 141-146.

[McA92a] E.T. McAdams, J. Jossinet, "A Physical Interpretation of Schwan's Limit Current of Linearity," *Annals of Biomedical Engineering*, Vol.20, pp. 307-319, 1992.

[McA92b] E.T. McAdams, J. Jossinet, "Limit voltage of linearity- A unified model," *Proceedings of the Annual International Conference of the IEEE Engineering in Medicine and Biology Society*, Vol.14, pp. 2368-2369, 1992.

[McA95] E.T. McAdams, A. Lackermeier, J.A. Mclaughlin, D. Macken, "The linear and non-linear electrical properties of the electrode-electrolyte interface," *Biosensors & Bioelectronics*, Vol.10, pp. 67-74, 1995.

[McL03] J. McLean, F.L. Degertekin, "Interdigital Capacitive Micromachined Ultrasonic Transducers For Sensing And Pumping In Microfluidic Applications," *Proc. Transducers '03*, Boston, USA, pp. 915-918, 2003.

[Mor53] P.M. Morse, H. Feshbach, *Methods of Theorectical Physics*, McGraw-Hill Book Company, 1953,

[Mph03] M. Mpholo, C.G. Smith, A.B.D. Brown, " Low voltage plug flow pumping using anisotropic electrode arrays," *Sensors and Actuators B*, Vol. 92, pp. 262-268, 2003.

[Mut02] S. Mutlu, C. Yu, P. Selvaganapathy, F. Svec, C.H. Mastrangelo, J.M.J. Frechet, "Micromachined porous polymer for bubble free electroosmotic pump," *Proc. IEEE MEMS*, pp. 19-23, 2002.

[Mut03] S. Mutlu, C. Yu, F. Svec, C.H. Mastrangelo, J.M.J. Frechet, and Y.B. Gianchandani, "A thermally responsive polymer microvalve without mechanical parts photo-patterned in a parylene channel," *Proc. Transducers 2003*, pp. 802-805, 2003

[Mut04] S. Mutlu, F. Svec, C.H. Mastrangelo, J.M.J. Frechet, and Y.B. Gianchandani, “Enhanced Electro Osmotic Pumping With Liquid Bridge and Field Effect Flow Rectification,” in *Proc. IEEE MEMS' 2004*, pp.850-853, 2004.

[Ols99] A. Olsson, G. Stemme, E. Stemme, “A numerical design study of the valveless diffuser pump using lumped-mass model,” *J. Micromech. Microeng.*, vol. 9, pp. 34-44, 1999.

[Pau98] P.H. Paul, D.W. Arnold, D.J. Rakestraw, "Electrokinetic generation of high pressures using porous structures," in *μTAS'98 Conference*, Banff, Canada 1998.

[Pet98] E.C. Peters, M. Petro, F. Svec, J.M. J. Frechet, "Molded rigid polymer monoliths as separation media for capillary electrochromatography," *Anal. Chem.*, vol. 70, pp. 2288-2295, 1998.

[Ram98] A. Ramosm, H. Morgan, N.G. Green, A. Castellanos, “Ac electrokinetics: a review of forces in microelectrode structures,” *J. Phys. D: Appl. Phys.*, vol. 31, pp. 2338-2353, 1998.

[Rey02] D. R. Reyes, D. Lossifidis, P.A. Auroux, A. Manz, “ Micro total analysis systems.1,2,” *Anal. Chem.*, vol. 74, pp. 2623-2636, 2002.

[Ric02] A. Richardot, E.T. McAdams, “Harmonic Analysis of Low-Frequency Bioelectrode Behavior,” *IEEE Transactions on Medical Imaging*, Vol. 21, pp. 604-612, 2002.

[Ric03] C.A. Rich, K.D. Wise, “A High-Flow Thermopneumatic Microvalve With Improved Efficiency and Integrated State Sensing,” *J. Microelectromech. Syst.*, vol.12, pp. 201-208, 2003.

[Ric65] C.L. Rice, R. Whitehead, “Electrokinetic Flow in a Narrow Cylindrical Capillary,” *The Journal of Physical Chemistry*, vol. 69, pp.4017-4024, 1965.

[Rob90] L.S. Robblee, T.L. Rose, “The Electrochemistry Of Electrical Stimulation,” *Annual International Conference of the IEEE Engineering in Medicine and Biology Society*, Vol. 12, pp. 1479-1480,1990.

[Rob94] J.K. Robertson, K.D. Wise, “A Nested Electrostatically-Actuated Microvalve For An Integrated Microflow Controller,” *Proc. IEEE Micro Electro Mechanical Systems 1994*, pp. 7-12.

[Ros90] T.L. Rose, L.S. Robblee, “Electrical Stimulation with Pt Electrodes. VIII. Electrochemically Safe Charge Injection Limits With 0.2 ms Pulses,” *IEEE Transactions on Biomedical Engineering*, Vol. 37, pp. 1118-1120, 1990.

[Saf93] E.B. Saff, A.D. Snider, *Fundamentals of Complex Analysis for Mathematics, Science, and Engineering*, Prentice-Hall, Inc. 1993.

[Sch00] K.F. Schrum, J.M. Lancaster, S.E. Hohnston, S.D. Gilman, “Monitoring electroosmotic flow by periodic photobleaching of a dilute, neutral fluorophore” *Anal. Chem.*, vol. 72, pp. 4317-2636, 2000.

[Sch99] R.B.M. Schasfoort, S. Schlautmann, J. Hendrikse, A.V.D. Berg, “Field-effect flow control for microfabricated fluidic networks,” *Science*, vol. 286, pp. 942-944, 1999.

[Sel02a] P. Selvaganapathy, *Microfabricated Components For An Integrated Microfluidic Electroanalysis System*, PhD. Thesis, University of Michigan, Ann arbor, 2002.

[Sel02b] P. Selvaganapathy, Y.-S. L. Ki, P. Renaud, C.H. Mastrangelo, "Bubble-free electrokinetic pumping," *J. Microelectromech. Syst*., vol. 11, pp. 1-6, 2002.

[Sel03a] P. Selvaganapathy, E.T. Carlen, C.H. Mastrangelo, “Electrothermally actuated inline microfluidic valve,” *Sensors and Actuators A*, vol. 104, pp. 275-282, 2003.

[Sel03b] P.R. Selvaganapathy, E.T. Carlen, C.H. Mastrangelo, “Recent Progress in Microfluidic Devices for Nucleic Acid and Antibody Assays,” *Proceedings of the IEEE*, vol. 91, pp. 954-975, 2003.

[Sha69] D. Shaw, *Electrophoresis*. Academic Press, 1969.

[Sho94] S. Shoji, M. Esashi, “Microflow devices and systems,” *J. Micromech. Microeng.*, vol. 4, pp. 157-171, 1994.

[Sim80] R.W. Simpson, J.G. Berberian, H.P. Schwan, “Nonlinear AC and DC Polarization of Platinum Electrodes,” *IEEE Transactions on Biomedical Engineering*, Vol. 27, pp. 166-171, 1980.

[Stu02] V. Studer, A. Pepin, Y. Chen, A. Ajdari, “Fabrication of microfluidic devices for AC electrokinetic fluid pumping,” *Microelectronic Engineering*, Vol. 61-62, pp. 915-920, 2002.

[Tak03] Y. Takamura, H. Onoda, H. Inokuchi, S. Adachi, A. Oki, Y. Horiike, “Low-voltage electroosmosis pump for stand-alone microfluidics devices,” *Electrophoresis*, vol. 24, pp. 185-192, 2003.

[Tho02] T. Thorsen, S.J. Maerkl, S.R. Quake, “Microfluidic Large-Scale Integration,” *Science*, vol. 298, pp. 580-584, 2002.

[Til73] B.V. Tilak, B.E. Conway, H.A. Kozlowska, “The real condition of oxidized Pt electrodes. Part III: Kinetic theory of formation and reduction of surface oxides,” *Electroanalytical Chem. Interfacial Electrochem.*, vol.48, pp. 1-23, 1973.

[Tri89] W.S.N. Trimmer, "Microrobots And Micromechanical Systems," *Sensors and Actuators*, vol. 19, pp. 267-287, 1989.

[Ung00] M.A. Unger, H.-Pu. Chou, T. Thordsen, A. Scherer, S. R. Quake, "Monolithic Microfabricated Valves and Pumps by Multilayer Soft Lithography," *Science*, vol. 288, pp. 113-116, 2000.

[Vet67] K.J. Vetter, *Electrochemical Kinetics*, Academic Press, 1967.

[Web99] J. R. Webster, *Monolithic Structures For Integrated Capillary Electrophoresis Systems*. PhD. Thesis, University of Michigan, Ann Arbor, 1999.

[Won03] P.K. Wong, C.-Y. Chen, T.-H. Wang, C.-H. Ho, "An AC electroosmotic processor for biomolecules," in *Transducers' 03*, Boston, pp. 20-23, 2003.

[Xie03] J. Xie, J. Shih, Y.C. Tai, "Integrated Surface Micromachined Mass Flow Controller," *Proc. IEEE Micro Electro Mechanical System 2003*, pp. 20-23.

[Yan03] J. Yang, D. Y. Kwok, "Time-dependent Laminar Electrokinetic Slip Flow in Infinitely Extended Rectangular Microchannels." *Journal of Chemical Physics*, vol. 118, pp. 354-363, 2003.

[Yan95] Q. Yan; A.S. Hoffman, "Synthesis of macroporous hydrogels with rapid swelling and deswelling properties for delivery of macromolecules," *Polymer*, vol. 36, pp. 887-889, 1995.

[Yan98] C. Yang, D. Li, "Analysis of Electrokinetic Effects on the Liquid Flow in Rectangular Microchannels." *Colloids and Surfaces A*, vol. 143, pp. 339-353, 1998.

[Yu00] C. Yu, F. Svec, J.M.J. Frechet, "Towards stationary phases for chromatography on a microchip," *Electrophoresis*, vol 21, pp. 120-127, 2000.

[Yu03] C. Yu, S. Mutlu, P. Selvaganapathy, C.H. Mastrangelo, F. Svec, J.M.J. Fréchet, "Flow control valves for analytical microfluidic chips without mechanical parts based on thermally responsive monolithic polymers", *Anal. Chem.* Vol. 75, pp. 1958-1961, 2003.

[Yu03] H. Yu, E.S. Kim, "Micropropulsion of air and liquid jet by acoustic streaming," *Proc. IEEE MEMS'2003 Conf.*, Kyoto, Japan, pp. 76-79, 2003.

[Zde94] M. J. Zdeblick, R. Anderson, J. Jankowski, B. K. Schoder, L. Christel, R. Miles, W. Weber, "Thermopneumatically actuated microvalves and integrated electrofluidic circuits," in *Solid-State Sensor and Actuator Workshop 1994*, Hilton Head, pp. 251-255, 1994.

[Zen01] S. Zeng, C.H. Chen, J.C. Mikkelsen Jr., J.G. Santiago, “Fabrication and Characterization of Electroosmotic Micropumps,” *Sensors and Actuators B*, vol. 79, pp. 107-114, 2001.

[Zen95] R. Zengerle, S. Kluge, M. Richter, A. Richter, “A bi-directional silicon micropump,” in *Proc. IEEE MEMS'1995 Conf.*, Amsterdam, The Netherlands, pp. 19-24, 1995.

[Zha96] W. Zhang, C.H. Ahn, “A bi-directional magnetic micropump on a silicon wafer,” *Solid-State Sensor and Actuator Workshop*, Hilton Head, South Carolina, p.94-97, 1996.

[Zum93] S.S. Zumdahl, *Chemistry*, D. C. Heath and Company, 1993.